Commissioning of a Novel Electrostatic Accelerator for Nuclear Medicine

Heinrich von Jagwitz-Biegnitz

Balliol College, Oxford

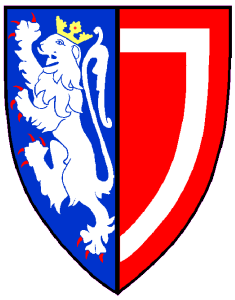

Thesis submitted in partial fulfilment of the requirements for the degree of Doctor of Philosophy at the University of Oxford

Hilary Term, 2015

ABSTRACT

Siemens Corporate Technology New Technology Fields Healthcare & Technology Concepts (CT NTF HTC) have proposed a novel electrostatic accelerator for nuclear medicine which aims at gradients of up to $10\,\mathrm{MV\,m^{-1}}$. With beam currents of $100\,\mu\mathrm{A}$ at $\approx 10\,\mathrm{MeV}$ it might replace cyclotrons whilst being simpler, more reliable and more cost effective. The accelerator concept consists of concentric hemispherical metallic shells spaced by insulators and placed in a vacuum system. The shells are interconnected by high voltage diodes so that they form a voltage multiplier with its highest voltage in its centre. Particle beams can be accelerated towards the centre through a set of holes in the shells. In tandem mode, with a stripper in the centre and a negative ion source as injector, beams of twice the centre voltage can be achieved.

This thesis presents several commissioning milestones of a test system for the novel electrostatic accelerator, thus validating the concept for commercial applications. An inter shell insulator has been designed and successfully tested to fields of $12\,\mathrm{MV\,m^{-1}}$. A diode protection concept has been devised and validated in realistic breakdown scenarios. An AC drive system including control software has been developed, delivering a sinusoidal input voltage of up to $140\,\mathrm{kV}$ peak to peak at $80\,\mathrm{kHz}$. An automatic process to carefully commission the high voltage system in vacuum has been created, implemented in a control system and successfully operated. A 4-shell prototype with these components has been successfully tested with achieved gradients of up to $5.5\,\mathrm{MV\,m^{-1}}$. A negative hydrogen ion source has been constructed, commissioned and characterised with a purposely developed wire grid. Beam currents beyond $200\,\mu\mathrm{A}$ have been achieved. Beam transport from the ion source through the 7-shell system has been demonstrated in simulations which are based on experimental data from the ion source characterisation. A stripper system has been designed and constructed.

ACKNOWLEDGEMENTS

I thank everyone who has helped and supported me during the eleven terms of my DPhil work. I thank Andrei Seryi for being an excellent academic supervisor, always approachable and providing invaluable advice. I also want to thank the amazing particle physics support team, Sue Geddes, Kim Proudfoot and Francesca Oliver for helping with all the inconceivable paperwork. I thank the team at Siemens CT NTF HTC for having me join on such an exciting project. In particular Oliver Heid for inspiring chats and ingenious ideas for hands-on problems in the lab. Thomas Kluge for his outstanding software framework, great training and saving help in coding crises. Paul Beasley for fun discussions, business insight and delicious pizza. Thanks to the experimental team at RAL. Dan Faircloth for being an inspiring scientist and a fun person to be around. Christoph Gabor, whose too early death has left us speechless, for his insulator ideas. Rob Selway for the most amazing engineering support ever, for being incredibly focussed, efficient and helpful, for remarkable generosity and dedication with the wire grid and for nice lunch conversations on outdoor fun. Andrew Holmes for sharing his vast knowledge about ion sources, both practically and theoretically. Many thanks also to my office mates in the physics department. Andy for always being happy to help and for knowing the answer to almost any question. Muhammad for magnificent support with automating my simulations. Thanks to the tutors and students of Somerville College for an unforgettable teaching experience. A huge thank you also to all the other friendly and helpful colleagues, especially Neven Blaskovic Kraljevic, for an admirable abundance of enthusiasm, for always being in contagiously good spirits and for taking so much time to help me advance my spanish and Phil Burrows for always being up for a friendly and often humorous chat.

The author gratefully acknowledges financial support for his work from Siemens AG and EPSRC under the auspices of an industrial case studentship.

This thesis was written using the LATEX typesetting package. All graphs were produced using GnuPlot, Python, Microsoft Powerpoint, Inkscape, LTSpice and Vectorfields Opera unless otherwise stated. This thesis and the research it describes are original work carried out solely by the named author, unless explicitly stated.

CONTENTS

LIST OF FIGURES

LIST OF TABLES

1. INTRODUCTION

As well as to almost every other area of life, the modern era has brought fundamental changes to medicine. The age of dubious quack doctors seems to be over once and for all after the discoveries of the 19th and 20th centuries. This applies both for diagnostics and treatment of disease and technology plays a key role in both of them, maybe even more so in diagnosis than in treatment. Alongside the complex analysis of blood samples and tissue which are possible nowadays, imaging techniques play a major role in diagnosis in many areas of medicine such as oncology, cardiology and orthopaedy. They enable medics to take a scientific approach to their diagnosis and at the same time they link them to scientists who provide imaging procedures. For physicists this opens a field of work which is interesting and demanding from the physics point of view and at the same time very meaningful as it impacts the lives of patients worldwide.

Wilhelm Conrad Röntgen's discovery of X-rays in 1895 can be seen as the birth of medical imaging. Technology has evolved since and medicine nowadays knows a large number of different imaging techniques employing different physics phenomena in numerous settings and combinations such as nuclear spin resonances, X-rays, γ-rays, particle-antiparticle annihilation, ultrasound, electric impedance and others. This involves physicists and engineers from a number of areas ranging from mechanics and electronics to nuclear physics and particle accelerators. This section deals with nuclear medicine which is the area of imaging employing radioactive materials which are injected into the body of the patient. The decay of these radioactive isotopes creates a

signal which is used for imaging. The main techniques in this field are called Single Photon Emission Computed Tomography (SPECT) and Positron Emission Tomography (PET). The supply of the radioactive materials used for SPECT and PET is crucial to these imaging methods and a major factor for their availability. SPECT isotopes are largely produced in nuclear reactors. This is an efficient way of producing large quantities, however the few reactors accounting for most of the production worldwide (Chalk River in Canada and Petten in the Netherlands provide 85 % of worldwide production [5]) are aging and likely to be shut down within the next decade with no substitutes in place to cover for them. Also the current technique for the production of the main SPECT isotope ^{99}Mo in reactors involves the use of enriched Uranium (i.e. higher than natural concentration of ^{235}U) which is a safety issue as ^{235}U can be used for nuclear weapons. Most PET isotopes are currently produced in particle accelerators, usually cyclotrons, which are distributed around the globe. As these isotopes have short half lives (from 2 minutes for ^{15}O to 110 minutes for ^{18}F) they require rather elaborate logistics or an expensive and space consuming accelerator in the hospital. This may well be seen as one of the limiting factors for the availability of PET imaging. Therefore the establishment of cheaper and simpler supply methods for PET isotopes might dramatically increase the availability of PET, especially in 2nd and 3rd world countries and therefore contribute towards the improvement of health care quality worldwide. It might also partly relax the problems connected with the supply problems for SPECT isotopes.

The invention of the novel electrostatic accelerator [6] by Siemens CT NTF HTC is a promising way towards this end. The accelerator is meant to be cheaper, simpler and more compact than currently used cyclotrons. The novel accelerator concept employs a voltage multiplier circuit similar to the Cockcroft-Walton cascade in order to transform

an AC voltage into a higher DC voltage. However, in this concept the capacitances of the Cockcroft-Walton cascade are represented by two sets of concentric hemispherical metallic shells. This geometry is very beneficial, as the shells act as capacitors, as shielding for the electrostatic fields and as a beamline. It will therefore be able to provide much higher gradients than conventional Cockcroft-Walton accelerators whilst keeping all the advantages. The accelerator will have its highest electrostatic potential in the centre of the accelerator itself (so called terminal), which will be shielded by all subsequent sets of shells. It will be operated in tandem mode. A negative ion source is placed on one side of the accelerator and the beam is extracted on the other side of the accelerator. The charge of the beam has to be changed in the centre of the accelerator via charge stripping with a carbon foil. With its robust and reliable technology the accelerator is a promising candidate for a compact and easy to handle machine which can be placed in any standard size hospital room and operated by medical staff without the need for dedicated accelerator physicists. A prototype for the novel accelerator is currently under commissioning at the Rutherford Appleton Laboratory (RAL) in Didcot, United Kingdom. This text explains some key concepts of the design of the accelerator and its components as well as the results of component testing and the first commissioning steps of a 7-shell prototype. It also gives some background on nuclear medicine.

1.1 Nuclear Medicine

1.1.1 History

Less than a year after Röntgen discovered X-rays in 1895, Antoine Henri Becquerel discovered natural radioactivity during experiments with uranium salts and his students Marie and Pierre Curie discovered several radioactive radioisotopes in the subsequent

years which resulted in a Nobel prize for all three of them in 1908. Whilst X-rays soon began gaining importance for medical imaging, the development of nuclear medicine took some more time. The detection of X-rays was much easier and the intensity of the sources much higher so that radioactivity was not widely used as a source of radiation to shine through the human body.

However in 1913 the Hungarian chemist George Charles de Hevesy came up with the idea of the radioactive tracer [7]. Attaching radioactive isotopes to biological materials enables the physicist to track these materials on their way through biological systems via monitoring the particles emitted from the decay of the radioisotopes. A story which is related in this context tells how de Hevesy attached a radioactive substance to his meat leftovers at the dinner table in an English boarding house in order to investigate some peculiarities of the English kitchen. He then detected the radioactivity in a different dish on a different day and was thus able to prove that the kitchen actually recycled the leftovers, accounting for the quality and taste of the food served in this English boarding house. De Hevesy soon identified the huge medical potential of his method and published his first paper on this topic in 1923 [8]. The paper reports on experiments with bean plants (Vicia faba) carried out at the university of Copenhagen. De Hevesy immersed the isotope ^{212}Pb in water and then placed the roots of the bean plants in this water for several hours. He would then wash the bean plant and burn stem, roots, leaves and fruits separately in order to determine the radioactivity of the ashes. He had found an easy way of investigating the accumulation of lead in different parts of the plant resulting in the discovery that up to a certain saturation level most of the lead is bound in the roots of the plant.

The following years saw many new experiments culminating in the publication of a paper by Herrmann Blumgart and Soma Weiss titled “Studies on the Velocity of

Blood" [9]. The two scientists describe a radium production and injection procedure which they developed at Boston City Hospital and the Harvard Medical School. The radioactive radium produced could be intravenously injected into the left arm of a patient and later on be detected in the right arm of the patient after having made its way through the heart and the lung and back into the arteries. Their work can be seen as the first application of nuclear medicine for human health care.

In 1934 Frédéric and Irène Joliot-Curie discovered the existence of artificially created radioisotopes after bombarding aluminium with alpha radiation. Together with Ernest Orlando Lawrence's invention of the cyclotron at the University of California in 1930 this was another milestone for the further development of nuclear medicine. Early nuclear medicine experiments had solely relied on natural isotopes. With later generations of Lawrence's cyclotrons however, new, not naturally occurring isotopes could be produced and tested for medical purposes. E. O. Lawrence's brother John, who was a medic at Yale University, was instrumental in these developments through collaborations with his brother.

After the end of the second world war scientists started to investigate the use of nuclear reactors for the production of artificial radioisotopes. Some of the equipment developed for the Manhattan Project was made available for this purpose and the 1950s saw the establishment of nuclear medicine as a separate field in medicine. New inventions on the detector side, such as the first rectilinear scanner and Anger's scintillation camera [10], made a strong contribution towards this development. In the 1960s the ^{99m}Tc technetium generator was invented, based on the decay of ^{99}Mo [11]. It provides a simple and practical solution for the supply of a tracer radioisotope for hospitals far away from nuclear or accelerator sites, as these generators typically operate for a whole week. The development of tomographic methods together with appropriate tracers led

to the establishment of new 3D procedures such as SPECT and PET in the 1970s and 1980s. The following decades saw improvements in resolution and accuracy facilitated by the increase in computing power as well as enhancements in detector technology. The most recent developments are the combination of nuclear medicine techniques with conventional imaging such as SPECT/CT, PET/CT or PET/MRI.

Today more than 35 million nuclear imaging procedures per year are carried out worldwide, 80 % of which are SPECT procedures using ^{99m}Tc and carried out on about 20,000 SPECT scanners. More than 95 % of the 4 million annual PET procedures use the glucose-like tracer FluoroDeoxyGlucose (FDG) making use of several hundred dedicated medical cyclotrons for the production of ^{18}F [2].

1.1.2 Imaging techniques

All nuclear imaging procedures follow the same pattern: A substance containing radioactive nuclei, the so called radiopharmaceutical, is administered to the patient intravenously, orally or via inhalation. The distribution of this radiopharmaceutical within the patient's body is then recorded, sometimes immediately, but usually a certain time after the radiopharmaceutical has been administered. Often a number of images of the distribution are taken after certain time intervals to investigate how the distribution of the radiopharmaceutical develops over time. The medical utility of this procedure chiefly depends on the biological function of the administered radiopharmaceutical. If the radiopharmaceutical has a particular biological function within the human body, the imaging procedure can give an insight into this biological function, e.g. one can obtain a map of metabolic activity within the body via administering the glucose like compound Fluorodeoxyglucose (FDG, with the Fluor being ^{18}F) and then taking images of the distribution of the administered FDG. In fact this is an important technique

for the diagnosis and staging of cancer patients, as tumour cells usually show a higher metabolic activity [2], [12], [13].

The procedure described so far might seem similar to the use of contrast agents in other imaging techniques like MRI and CT. However there are two important differences: The contrast agents in MRI and CT generally increase the contrast of the images, however they do not link as directly to biological functions as the radiopharmaceuticals in nuclear imaging. This is due to the second difference, which is the source of the radiation used to construct the image: In MRI the image is constructed from radiation coming from the relaxation of magnetic states of protons in a strong external magnetic field. The protons are parts of water molecules within the human body and their magnetic states are excited first by external radio frequency radiation with an appropriate resonance wavelength and then the external RF is switched off and the radiation coming from the relaxing magnetic states of the protons is measured. The technique therefore gives a picture of the water distribution within the body. In radiography and CT an external X-ray source is placed on one side of the human body or a particular part of it and a detector is placed on the other side. The detector measures the intensity of the radiation which traverses the body and therefore gives a measure of the attenuation of X-rays in the tissue between the source and the detector. In nuclear imaging however the administered radiopharmaceuticals themselves are the source of the radiation which is used to construct the images, as they always contain some radioactive nuclei. The radiation coming from the decay of these nuclei, i.e. from within the body, is recorded by detectors outside the body and an image is reconstructed from the recorded data. The contrast, resolution and quality of the image therefore strongly depends on the wavelength of the radiation coming from within the body and therefore on the particular radioactive nucleus used for the procedure. Usually nuclear images

contain rather little anatomic detail, as they are solely based on the distribution of the radiopharmaceutical. This fact has led to the combination of nuclear images with imaging techniques capable of providing extensive anatomic detail like CT or MRI, even resulting in combined machines like SPECT/CT, PET/CT or PET/MRI.

Scintigraphy

The invention of Anger's scintillation camera was the starting point for the technique called scintigraphy. The radiopharmaceuticals used for scintigraphy are γ-emitters, some of them are actually β-emitters which emit a gamma photon as well. A scintillator is used to detect the gamma rays coming from inside the human body. Behind the scintillator is a photo film or a photomultiplier which records the scintillation events from the scintillator. As the radiation source is spread out over the whole body some sort of optics is required. The use of traditional lens optics is impossible for gamma wavelengths, Anger therefore used the principle of the pinhole camera. A very small aperture is placed between the patient and the scintillator and the rays coming through the pinhole create an inverted picture of their origins on the scintillator. However, as the pinhole needs to be rather small in order to get a satisfactory resolution, only a very small fraction of the created radiation makes its way to the scintillator and therefore the administered radioactive dose needs to be rather high or the exposure time very long in order to get a satisfactory image. Except from some special applications where multi-pinhole setups are still used nowadays [2] the pinholes have been replaced by a collimator setup. The collimator consists of a thick plate with many parallel holes forming parallel tubes. The holes ensure that only rays which come from a direction perpendicular to the scintillator can make their way to the scintillator. The image on the scintillator is therefore a 2D projection of the 3D distribution of the

radiopharmaceutical. In the very first approaches the photons from the scintillator were recorded on a photo film. However as the doses required to create an image on a photo film are rather high compared to common event rates radiated by radiopharmaceuticals, it is rather impracticable to get an image without exceedingly long exposure times or very high dose rates to the patient. Scintillation cameras nowadays therefore work with photomultipliers (PMT), which are capable of detecting single photon events from the scintillator. The signal of the PMT is proportional to the intensity of the light from the scintillator and therefore to the energy of the gamma photon incident on the scintillator. This enables the system to exclude at least part of those photons which are scattered within the body and therefore contain incorrect directional information. The PMTs usually have diameters of several cm and therefore their resolution as a pixel detector would be quite limited. Events in the scintillator produce a light cone which is usually broader than a single PMT. The light pulse created by a gamma event therefore usually hits several PMTs and the position of its origin can be calculated from the ratios of the intensities of the signals from the different PMTs, yielding in a much higher accuracy. The amplitude of the added signal of all involved PMTs gives a measure of the gamma photon energy. The acquisition system records all events over a certain amount of time and creates a 2D histogram which represents the actual projection of the 3D distribution of the radiotracer.

The resolution of the image is severely limited by a large number of factors, most of them not inherent to the irradiation process itself. The gamma energy of the used nuclei is usually somewhere between 80 keV and 500 keV (140.5 keV for the most common isotope ^{99m}Tc). ^{99m}Tc is a pure γ-emitter, and its decay product ^{99}Tc is to be considered as stable (half life 211,000 years), however other scintigraphy isotopes are β-emitters. This means they also radiate an electron which contributes to the radi-

ation dose administered to the patient without contributing to the imaging process. Low energy gamma radiation has the problem of attenuation within the body and cannot travel through infinite thickness of tissue. Also, depending on the location of the nucleus along the projected axis, gamma rays travel different distances through tissue and are therefore attenuated more or less strongly. Another limitation is given by the collimator's hole diameter and wall thickness. Higher energy rays require thicker collimator walls in order to absorb photons coming in at angles other than perpendicular. The scattering of rays within the body puts another limit to the resolution, as the energy resolution of the detector is usually limited due to the non-uniformity of the scintillator crystal as well as attenuation within the crystal itself and other factors. Some specialised systems use elaborate collimator shapes like concave or convex geometries or multi-pinholes as well as different detector concepts like photo diodes instead of PMTs or direct gamma detection with Cadmium-Zinc-Telluride detectors without the need for a scintillator [2].

Many of the effects which hamper the resolution can be corrected for. E.g. it is possible to work with a calibration table for the non-linearity of the crystal and to do a numeric correction for the attenuation in tissue, possibly using attenuation maps created by the use of external X-ray or gamma sources. Nevertheless for common whole-body hospital style applications the resolution of scintigraphy images is limited to about a cm which is at least ten times worse than conventional techniques like MRI and CT which reach down to sub millimeter resolutions.

SPECT

Single Photon Emission Computed Tomography (SPECT) is a technique which uses the same radiopharmaceuticals and similar detection techniques (in fact often the very

same detectors) as scintigraphy, however it is capable of creating 3D images. Usually the detector is mounted on a gantry and can be moved around the patient. It then takes 2D projection images of the 3D distribution from a number of different angles. The application of suitable tomographic reconstruction techniques then provides 3D information again. Depending on the number of pixels/voxels in the image, this usually requires a substantial amount of computing capacity. With modern computers this is no extraordinary challenge. It was a problem however in the 70's and 80's when tomographic reconstruction techniques were first adopted and the performance of computers was several orders of magnitude lower than it is today. The obtained 3D images make it much easier for the physician to diagnose their patient. Although it takes much longer to record the images, as often tenth or hundreds of positions have to be covered instead of just one, the radiation dose does not necessarily have to be higher. The accuracy of SPECT images compared to scintigraphy images is much higher, especially when it comes to quantitative measurements like kinetic tracer studies. However the anatomic detail of SPECT images is still rather little due to both the limited resolution of SPECT as well as the fact that the image only comes from the distribution of the radiopharmaceutical. Physicians therefore usually take CT images of the patient as well and it is therefore useful to combine the techniques in one machine to improve the registration of the two images. The combined machines are called SPECT/CT and are a commercial standard nowadays.

PET

Positron Emission Tomography (PET) is a tomographic imaging technique which relies on β^+-emitters, making use of the positron and not being dependent on any gamma radiation produced by the decay itself. The emitted positrons have a rather small range

in the tissue (several mm or even less, depending on the energy). When their kinetic energy declines, the cross section for an annihilation process

$$e^+ + e^- \quad \rightarrow \quad \gamma + \gamma \tag{1.1}$$

increases very much and the positron annihilates with an electron. Due to energy-momentum conservation there must always be at least two photons. However the cross section for the production of three or more photons should be lower by a factor of the order of the quantum electrodynamics coupling constant $\alpha \approx \frac{1}{137}$ as these processes have at least three vertices compared to two vertices for the two photon process. In fact, as experiments show [14] the probability for three or more photons is about 10^3 times smaller and one can neglect it for the following considerations. As the positron and the electron both are almost at rest when the annihilation happens, it follows from energy-momentum conservation that the two photons are emitted into opposite directions and both have the same energy of 511 keV which is the mass of the electron and the positron. Usually a ring of detectors is placed around the patient so that both photons can be detected. With the aid of a coincidence analysis (annihilation coincidence detection ACD) done by the detector electronics, one can then find pairs of photon events which originate from one single annihilation event each. The coincidence detection makes use of the fact that the photon events must occur at the same time. Of course this requires the general event rate to be low enough not to have random coincidences which do not originate from the same annihilation event. In practice one will look at events within a certain time window, as the detector time resolution is finite and the scintillators and PMTs in the detector induce some uncertainty as well. Also there is a path length difference between the two photon paths from the

positron to the detector. Of course there might be random coincidences as well and the time window must be chosen appropriately to capture most of the real events whilst still keeping the random coincidence rate as low as possible. Usually the window width is set to a few ns. As we get events in two detectors from every positron and given the fact that the photons go off in opposite directions it is now possible to retain directional information by just drawing a line connecting the two detectors. This principle is called electronic collimation and makes mechanical collimators as used for scintigraphy futile. The sensitivity of PET imaging is therefore much higher compared to SPECT, as in SPECT most photons get absorbed in the collimator walls, whereas in PET imaging literally all photons which leave the patient contribute to the measurement. Furthermore, with a ring of detectors placed around the patient, 2D projections from all angles are recorded at the same time. In general this makes PET imaging faster in comparison to SPECT, which is an advantage especially for dynamic studies. The set of 2D projections from different angles is then used for the tomographic reconstruction of a 3D image of the radiopharmaceutical's distribution in the patient's body in a similar way as it is done with other tomographic techniques. Depending on the detector's time resolution time of flight (TOF) measurements are possible as well. If the speed of the detector electronics, the cable delay and the delay of the PMTs were the same for all detectors, then the time difference of the registration of two coincidence events would directly correspond to the path length difference of the two photons. From this one could directly reconstruct the location of the annihilation of the positron and any further tomographic analysis would become superfluous. However, even in the best PET machines with ultrafast scintillators like lutetium orthosilicate (LSO) the TOF resolution is limited to the order of 10 cm and cannot be relied on for the reconstruction. Nevertheless the obtained information can be used within the

Isotope	max. Energy	avg. Range in Water
^{3}H	18.6 keV	< 0.01 mm
^{11}C	961 keV	1.0 mm
^{14}C	156 keV	0.1 mm
^{13}N	1.19 MeV	1.3 mm
^{15}O	1.72 MeV	2.0 mm
^{18}F	635 keV	0.6 mm
^{32}P	1.74 MeV	2.0 mm
^{82}Rb	3.35 MeV	4.3 mm

Tab. 1.1: PET isotopes and the range of their β^+ radiation in water. The range should be as small as possible to keep PET resolution high. Data taken from [2]

tomographic reconstruction process and contributes to considerable noise reduction in high edge PET scanners [2].

The detectors used for PET work in a similar way as those for scintigraphy, however without the collimators. Also different scintillators (different material and much thicker) are used as the detector needs to be optimised for 511 keV whereas scintigraphy and SPECT scanners are usually optimised for the 140 keV gamma energy of the ^{99m}Tc decay. A property peculiar to PET is an inherent limit to the resolution, which is caused by the path length of the positron before its annihilation with an electron and by the kinetic energy of the positron and electron at the time of their annihilation. When the positron is emitted in a β^+ decay it has a certain kinetic energy. As the annihilation happens almost at rest, the positron first travels a certain distance in tissue where it scatters elastically and loses energy until it comes to rest and annihilates. The location of the annihilation therefore differs from the location of the decay (and therefore of the radiopharmaceutical) by an average distance depending on the energy of the emitted positron, e.g. less than a mm for the 635 keV positrons emitted by ^{18}F up to half a cm for the 3.35 MeV positrons emitted by ^{82}Rb (see also Table 1.1). The second

inherent limitation is caused by the fact that the positron-electron pair is not always completely at rest at the time of its annihilation. According to momentum conservation the photons will therefore not be emitted at angles of exactly 180°, but slightly more or less than that. It is not possible to detect this inaccuracy without gathering additional directional information, e.g. using a collimator, which would mean losing many of the advantages of PET.

As with scintigraphy and SPECT the anatomic detail provided by PET images is rather low, therefore the combination with CT or MRI images is a usual procedure. In fact nowadays almost every standard PET scanner available from healthcare companies has a combined CT scanner on board. The two can easily be integrated and work alongside each other. The combination of MRI and PET seems promising from the medical point of view, however the technical side is far more complicated. The PMTs usually used in PET scanners work with secondary electron multiplication and are therefore extremely sensitive to magnetic fields. In fact many PET scanners even do a numerical correction of their data to account for the change of the earth magnetic field when the gantry turns round. Nevertheless combined PET/MRI scanners exist, usually ensuring that the PET detector is far away from the MRI magnet to prevent interference. Of course this makes simultaneous acquisition impossible. However new approaches are under investigation, e.g. using field cycled MRI (FCMRI), where the PET detector is only read out in the phase when the magnetic field is zero [15] or guiding the signals from the scintillators out of the magnetic field with optical fibers or the replacement of PMTs by avalanche photodiodes [16]. The combination of PET and MRI therefore remains and active field of research.

PET vs. SPECT vs. scintigraphy

In general PET and SPECT both can be used for simimlar medical procedures, i.e. the 3D imaging of biological processes within the human body. PET has the advantage of electronic collimation, i.e. no mechanical collimator is required, and taking projections from all angles at the same time. This enables PET either to work with lower quantities of the radiopharmaceutical or to perform the imaging process much faster, which is especially useful for dynamic studies. Despite the inherent limits of PET resolution (about a mm for ^{18}FDG) the resolution of PET scanners (app. 6-7 mm) is usually much better than that of SPECT and scintigraphy scanners (about a cm). For both types the resolution strongly depends on the distance between the object and the detector and therefore all parameters need to be known in order to make a direct comparison between two systems. Dedicated scanners for brain or heart can achieve higher resolution and specialised scanners for small animal imaging actually get much closer to the inherent limit of PET. A challenge for SPECT scanners is the attenuation of the 140 keV gammas from ^{99m}Tc and the degradation of the resolution towards the centre of the 3D image (i.e. the patient). The attenuation for 511 keV is much weaker and PET does not show degradation towards the center of the image as no mechanical collimators are used. The low resolution of PET and SPECT leads to the so called "partial volume effect": If an increased concentration of the radiopharmaceutical is located in a structure smaller than the resolution of the imaging technique, then the image will show a larger area with a lower density of the radiopharmaceutical, i.e. the concentration peak will be blurred. The integral over the concentration will still be correct, but the actual biological fact will look less severe than it actually is. It is obvious that PET with its generally better resolution is less prone to this complication than SPECT [12].

Technique	Image Content	Insight	Resolution	Radiation Risk
MRI	Water	Soft Tissue	High	No
CT	Absorption	Bones	Very High	Yes
SPECT	Tracer	Biological	Poor	Yes
PET	Tracer	Biological	Medium	Yes

Tab. 1.2: Characteristics of various imaging techniques.

On the more practical side one has to consider the radiopharmaceuticals available for both techniques: They enable the investigation of biological processes and therefore the different medical procedures. At the moment PET imaging mostly uses ^{18}FDG which gives insights into glucose metabolism, whereas SPECT and scintigraphy work with a wide range of tracers, almost all of them using ^{99m}Tc. Whilst ^{18}F is produced in cyclotrons to be followed by elaborate chemistry to yield ^{18}FDG, the production of Tc in generators and the easy preparation of tracers with so called "cold kits" makes SPECT and scintigraphy much cheaper than PET. Also the generators can be transported literally anywhere as they last for about a week, whereas FDG needs more elaborate logistics with a half life of two hours. Furthermore SPECT and even more so scintigraphy scanners themselves are several times cheaper than PET scanners, increasing their practical advantage in every day clinical practice. Although planar scintigraphy does not provide 3D information, its much lower cost and higher availability makes it an important tool for medics all around the world. However the development of new PET radiopharmaceuticals in the future as well as sophisticated systems like PET/MRI will probably further increase the utility of PET. New, cheaper, simpler and more practicable approaches towards the producton of isotopes are an important effort towards the propagation of PET. The novel electrostatic accelerator is meant to contribute towards this goal.

1.1.3 Tracers and medical procedures

There is a wide range of medical procedures in nuclear medicine, which serve to test different processes in the human body or to diagnose disease. The most important ones regarding their practical relevance are found in oncology and cardiology and rely on the SPECT isotope ^{99m}Tc and the PET isotope ^{18}F.

PET tracers The whole PET landscape is dominated by one single tracer, ^{18}Fluorodeoxyglucose (FDG). FDG is a glucose like molecule and is treated by human cells in the same way as glucose is. FGD can therefore be used for the assessment of glucose metabolism in the brain, lungs and the heart in order to diagnose a range of diseases. It is especially important for oncology, as tumours usually have a higher metabolic activity than healthy tissue. They can therefore be detected with FDG.

Apart from FDG, there are four more PET tracers currently approved by the US Food and Drug Administration (FDA), which only have small practical relevance as they compete with more practical SPECT or scintigraphy procedures. These include rubidium chloride (^{82}RbCl) and ammonia ($^{13}NH_3$) which are both used for myocardial perfusion tests [13] as well as sodium fluoride (Na^{18}F) which is used for bone scans. A new development which only recently got approval from the FDA [17] is florbetapir (^{18}F-AV-45), which is used for the investigation of cognitive impairment, e.g. Alzheimer's disease. A number of other tracers are used in research and a lot of research work currently focuses on the development of new tracers for medical applications.

SPECT and scintigraphy tracers The tracers used for scintigraphy and SPECT are generally the same, as SPECT is just an extension of scintigraphy. There is a long list of different tracers for SPECT, most of which contain ^{99m}Tc, which is by far the most important isotope in nuclear medicine. The tracers are usually large biologically

active molecules and the imaging isotope is linked to some biologically inactive part of the molecule. Examples for Tc containing tracers are ^{99m}Tc-MDP for bone scans, ^{99m}Tc-sestamibi for myocardial perfusion tests, ^{99m}Tc-HMPAO for cerebral perfusion tests and DTPA for renal function testing [2]. There are also isotopes which are used as tracers in their own right, i.e. without attaching them to a biologically active molecule. An important example is 123-iodide ($^{123}I^-$), which is used for the diagnostic of thyroid diseases.

Oncology In oncology nuclear medicine plays a key role for the localisation of tumours as well as for the monitoring of the progress of ongoing therapies. The usual technique is the injection of a tracer which accumulates in tumours. A suitable SPECT tracer is $^{67}Ga^{3+}$ which is administered in the form of a salt and accumulates in tumours as well as in areas of inflammation and infection. Other SPECT tracers used in oncology are ^{99m}Tc-sestamibi or ^{99m}Tc-MDP which is specifically used for bone scans.

The imaging of cell metabolism with PET scanners using FDG is a very important and successful technique in oncology. The metabolic activity of malignant tumours is far higher than that of healthy tissue and they can therefore be detected using this technique. Metabolic imaging with FDG is the most important application of PET today.

Cardiology Nuclear imaging has a great significance for the diagnosis of cardiac diseases. An important technique is the measurement of myocardial perfusion, i.e. the blood flow in the heart muscle. This measurement is usually done with 3D scanners and is often gated by combined electrocardiography in order to capture the heart in different states of motion. The technique uncovers areas of low blood flow within the heart muscle (myocardium) and, among other applications, serves for the diagnosis of

coronary artery disease, which is the major cause for heart attacks. Radiopharmaceuticals used for myocardial perfusion imaging are ^{99m}Tc-sestamibi, ^{99m}Tc-tetrofosmin and ^{201}Tl for SPECT and ^{82}RbCl for PET.

A different technique is the imaging of the glucose metabolism of the myocardium with FDG in PET scanners. This procedure is useful for the diagnosis of coronary artery disease and to detect non-functioning tissue. In practice it is sometimes combined with myocardial perfusion imaging in PET scanners using ^{82}RbCl or $^{13}NH_3$.

Other areas There are many other interesting techniques, some of which will be mentioned here. With nuclear tracers one can very effectively perform leakage tests. E.g. a tracer is administered to the patient orally and the image can then record its way through the patient's gastro-intestinal tract. Even smallest leakages from the tract can be made visible this way. Another example is the testing of the blood-brain barrier which in a healthy human prevents the diffusion of most substances between the blood and the brain. ^{99m}Tc-DTPA is administered to the patient. With a healthy blood-brain barrier this should however not be able to enter the patient's brain. Furthermore metabolism measurement with FDG as well as perfusion tests with ^{99m}Tc-HMPAO and ^{99m}Tc-ECD are used for the diagnosis and research of many neurological diseases like dementia, seizure disorders, psychiatric diseases or cerebro vascular disease. Another technique is the injection of human cells labelled with ^{111}In. E.g. this could be white blood cells to detect inflammations or dead red blood cells to test the function of the spleen. ^{123}I is used to measure the uptake of iodine by the thyroid gland.

Promising research areas Very promising areas of research are the development of labelled antibodies and of labelled receptor binding molecules. An example is the labelling of monoclonal antibodies with ^{111}In for the detection of colorectal carcinoma.

Another example is the labelling of octreotide with ^{111}In (SPECT) or ^{11}C or ^{68}Ga (both PET) for the detection of neuroendocrine tumours. Octreotide binds to somatostatin receptors which are particularly found in these tumours. The labelling of antibodies as well as receptor binding substances are said to be very promising areas of research as they might open up a vast variety of diagnostic possibilities for a large spectrum of diseases. Furthermore the same techniques might be used for effective treatment methods using radioisotopes [12].

1.1.4 Treatment with Radioisotopes

Generally there are two types of treatments with radioactive substances in the human body: Sealed source radiotherapy (brachytherapy) and unsealed source radiotherapy.

For brachytheraphy the radioisotope is confined in a physical container which is placed inside or near the actual tumour. In many cases this requires surgery to place the radioactive implant in the patient's body and again to remove it after the treatment is completed. Brachytherapy is used for the treatment of cervical, prostrate, breast and skin cancer. The used isotopes are usually γ-emitters, e.g. ^{137}Cs, ^{192}Ir or ^{125}I.

Unsealed radiotherapy relies on the chemical or biological distribution of the isotope in the body and therefore similar mechanisms as for nuclear imaging can be used. It is desirable to use β-emitters for this therapy method as the radioisotope will be directly linked to the cancer cells. An important example for this therapy is the treatment of thyroid cancer with ^{131}I which is an electron emitter (606 keV) but also radiates a high energy γ-photon (364 keV). Of course one has to be aware that the long range of the gamma radiation might affect other persons who come close to the patient. Pure β-emitters like strontium (^{89}Sr) would therefore be preferable. The latter is administered as strontium chloride and is used for bone cancer patients, especially for the palliation

of aches resutling from painful bone metastases. Although strontium is a pure β-emitter one still has to be careful not to expose other people than the patient, e.g. the urine might contain radioactive strontium.

As with imaging, an important future area is the labelling of antibodies which bind to antigens present in the tumours. This technique is called radioimmunotherapy and it is e.g. used for the treatment of blood cell lymphomas with ^{131}I labeled monoclonal antibodies [18]. A lot of research is carried out in order to become able to produce and effectively label other antibodies to widen the scope of this very promising technique.

1.1.5 Radioisotopes and their production

Throughout the history of nuclear medicine a large variety of isotopes have been in use. At the very early beginnings these were naturally occuring isotopes as the only ones available. Later on more and more artificial isotopes were discovered and became available. Today a small number of artificial isotopes dominate medical practice based on two factors: Suitability for the medical and imaging process and practicality of supply. The supply of radioisotopes is the main limiting factor for the implementation of nuclear medicine procedures as the methods of production are rather elaborate and expensive. Generally there are three main nuclear reactions which are used for the production of isotopes for nuclear medicine. These are fission, neutron capture and proton capture/transfer reactions.

Requirements for medical isotopes There is a number of requirements for isotopes, some of which contradict each other so that at times a trade-off has to be made. The main requirements are:

1. Detectability. Gamma rays should have an energy of at least 50 keV in order to be able to traverse the human body and still give a good signal in the detector

of the imaging scanner.

2. Labelling. They should be able to be attached to molecules which are used in biological processes in the human body. This gives an advantage to smaller, "biological" elements like Oxygen compared to larger elements like Technetium.

3. Activity. They should have a high specific activity in order to give a good ratio between injected quantities and detected event rate. This limits the exposure of the patient as well as making sure that the injected substance doesn't impact the patient biologically. Naturally a short half life increases the activity.

4. Transportability. The isotopes need to be produced, attached to a carrier molecule and then afterwards be transported to the patient. This takes time which reduces the activity. If transportation over longer distances or lengthy chemical procedures are inevitable, then a longer half life will be beneficial.

Of course availability and cost play a key role too and need to be considered in every case.

Fission Medical isotopes can be produced from the fission of large nuclei. The most common process is the fission of ^{235}U induced by slow neutrons in nuclear reactors:

$$^{235}_{92}U + n_{slow} \quad \rightarrow \quad ^{A}_{Z}X + ^{235-A}_{92-Z}Y + \gamma + x \cdot n_{fast} \tag{1.2}$$

The resulting isotope is carrier free, i.e. it is possible to obtain high specific activities of the isotope. However, the fission process yields a large number of possible products whereas usually only one of those is desired for medical use, so that a large number of side products are present which need to be chemically separated from the desired

isotope for medical use. Examples for medical isotopes produced by fission are ^{99}Mo (which decays into the ^{99m}Tc for SPECT) and ^{131}I.

Neutron capture Neutron capture is a nuclear process which happens in nuclear reactors and can be used for the production of medical isotopes in reactor facilities. However other safer or easier accessible neutron sources could potentially be used for this process as well, of course it is crucial that alternative neutron sources reach a reasonable neutron flux. Neutron capture involves the following processes

$$ {}^{A}_{Z}X + n \rightarrow {}^{A+1}_{Z}X + \gamma \tag{1.3} $$

or more rarely

$$ {}^{A}_{Z}X + n \rightarrow {}^{A}_{Z-1}Y + p \tag{1.4} $$

The more common process in Equation 1.3 does not change the element of the irradiated target, i.e. the produced medical isotope is not carrier free. This limits the specific activity as the isotope cannot be chemically separated from its sister isotopes. Therefore very high neutron flux is desirable to transform a high portion of the isotope into the desired medical isotope.

Direct reactions Direct reactions like proton capture or transfer reactions are usually employed in accelerator based isotope production facilities. A particle accelerator irradiates a fixed isotope target with protons, deuterons or alpha particles inducing nuclear reactions in the target. These reactions change the element and the obtained isotope is thus carrier free resulting in high specific activity. Common reactions are:

$$ {}^{A}_{Z}X + p \rightarrow {}^{A}_{Z+1}Y + n \tag{1.5} $$

and

$$ {}^{A}_{Z}X + d \rightarrow {}^{A+1}_{Z+1}Y + n \tag{1.6} $$

and

$$ {}^{A}_{Z}X + p \rightarrow {}^{A-3}_{Z-1}Y + {}^{4}_{2}\alpha \tag{1.7} $$

Of course the cross sections for these reactions do depend on the energy of the incident particle and actually most of these reactions have a threshold energy below which the cross section equals zero. This means that accelerators for this purpose have to reach at least the threshold energy. In practice however the energy used in facilities is often much higher than the threshold energy as up to a certain level the cross section increases with the energy of the incident particles. Nevertheless it can be attractive to work below the threshold energy of certain side products to get a "cleaner" result, of course making a trade off with the achieved yield. However, with accelerators capable of higher currents and respectively robust targetry to deal with the beam power, these drawbacks could potentially be overcome.

Reactors

The production of radioisotopes in nuclear reactors is currently the standard technique for SPECT isotopes. Usually targets are placed near the reactor core to enable neutron capture or induced fission of the target. After a certain amount of time the target gets taken out of the reactor and processed in a radiochemistry lab. As this requires frequent access to the reactor core, power plants or facilities for nuclear weaponry are usually not used for the production of medical isotopes. However there are over 200 research reactors worldwide and some 70 of them are used for the production of medical isotopes ([19]). Another method of obtaining medical isotopes from reactors

is the use of fission products from within the reactor core. Of course this involves elaborate processing as the range of fission side products is quite large but the amount of available material is usually larger than with separate targets outside the reactor core. ^{99}Mo, the mother isotope of ^{99m}Tc, which is the most important medical isotope, can be produced in reactors by both techniques described above. The ^{99}Mo with a half life of 2.7 days is used in so called Technetium generators. The ^{99}Mo in the generator is bound by a solid substrate with a liquid which is able to chemically dissolve Tc (or respectively the products of chemical reactions containing Tc) but not Mo (or respectively the chemical compounds containing the Mo). Whenever a ^{99}Mo nucleus decays into Technetium, it can be dissolved into the solution and be extracted from the generator. This technique widely increases the viability of Tc as a tracer. Tc itself has a half life of only 6 hours. Using the generator technique however, one can provide a device which is able to deliver reasonable amounts of ^{99m}Tc for about a week. This is ideal for long range transportation and the invention of the generator concept in the 1960's has laid the foundation stone for the worldwide success of Tc as a medical tracer isotope. In fact ^{99m}Tc is by far the most important medical isotope today and virtually all of it is procured from ^{99}Mo generators which in turn get their Mo from nuclear reactors. However, the reactor technology has a number of drawbacks. Most of today's production is covered by a small number of old reactors which are unreliable and most of them are planned to be shut down within the next ten years, some of them without any replacement planned at all. The design and construction of nuclear reactors is very challenging and expensive and the political climate in many countries has turned against nuclear reactors in general. Furthermore most procedures for ^{99}Mo production use ^{235}U enriched Uranium targets which raises proliferation issues.

Isotope	Half-Life	β^+ fraction	max. β^+ energy
^{11}C	20.4 min	0.99	960 keV
^{13}N	9.96 min	1.00	1.19 MeV
^{15}O	123 s	1.00	1.72 MeV
^{18}F	110 min	0.97	635 keV
^{62}Cu	9.74 min	0.98	2.94 MeV
^{64}Cu	12.7 hr	0.19	580 keV
^{68}Ga	68.3 min	0.88	1.9 MeV
^{76}Br	16.1 hr	0.54	3.7 MeV
^{82}Rb	78 s	0.95	3.35 MeV
^{124}I	4.18 d	0.22	1.5 MeV

Tab. 1.3: An overview over PET isotopes. Short lifetimes are good for low patient doses, but they introduce logistic difficulties. Data taken from [2]

Accelerators

Accelerators have been used for the production of isotopes even before the construction of the first nuclear reactor in 1946. In particular isotopes for PET procedures are generally produced in accelerator facilities as there are no viable techniques to produce them in reactors. The majority of accelerators in medical isotope production nowadays are cyclotrons working in the energy range of 12-20 MeV. They accelerate protons or deuterons onto a target which later on gets processed immediately. However, electrostatic accelerators like van-de-Graaff or Cockcroft-Walton have played a role historically and the novel electrostatic accelerator treated in this thesis is another example of electrostatic technology for nuclear medicine applications. As the half lives of typical PET isotopes are rather short (see Table 1.3), they need to be produced near the location of their use or elaborate logistic procedures have to be employed.

This has led to the use of hundreds of cyclotrons in numerous locations worldwide, many of which have been procured from commercial suppliers. The accelerator pro-

duction of PET isotopes is decentralised and independent of nuclear technology and Uranium. It thus avoids some of the problem areas connected with reactors.

Given the recent problems with reactors, scientists have come up with a number of new ideas for the production of medical isotopes. One of these ideas is the replacement of cyclotrons by simpler and less expensive electrostatic technology in order to make PET less expensive and more accessible and possibly replace some of the SPECT procedures.

Another approach which is investigated by canadian researchers at TRIUMF (Canada's national nuclear physics lab) is the photon induced fission of ^{238}U [5] using photons from Bremsstrahlung created by an electron beam.

A different reaction for the production of ^{99}Mo using photons is from ^{100}Mo

$$^{100}Mo + \gamma \quad \rightarrow \quad ^{99}Mo + n \tag{1.8}$$

Experiments with Bremsstrahlung from a 20 MeV electron beam performed by V. L. Uvarov in 1997 have successfully shown that this is viable and a study by Bennett et al. [20] illustrates that the construction of 20 electron accelerators would be sufficient to cover the supply of the entire US at a cost lower than the current production from reactors.

Both processes discussed above avoid ^{235}U altogether as well as the need for a reactor. Other concepts use neutrons created by accelerators, e.g. from spallation targets or from reactions between accelerated protons and targets containing Deuterium or Tritium.

1.2 Electrostatic Accelerators

1.2.1 History of Electrostatic Accelerators

Early Developments The history of electrostatic generators can be traced back to the origins of research on electricity in general. First electrostatic generators were made as early as the 17th century, e.g. Otto von Guericke's charge separation machine using the friction of rotating sulphur spheres in 1663 ([21]). A machine with a silk belt was made by Walckiers de St. Amand in 1784 ([22]) and in 1883 James Wimshurst ([23]) presented a machine similar to the influence generators used in school demonstrations nowadays. In 1872 Augusto Righi completed a charge seperation machine which he made for his doctoral thesis ([24]). It contained charged cylinders on an insulated rope and had stunning similarities with the Pelletrons built by Ray Herb in the second half of the twentieth century ([25]). Although these early developments foreshadowed many of the technologies which were later picked up or reinvented for large high energy accelerators, the objectives of those early experiments were quite different to modern ones. The main focus was on investigating electricity and high voltage in general rather than using it for particle acceleration in order to perform physics experiments with particle beams.

The Dawn of Nuclear Physics Experiments This changed however with Rutherford's discovery of the nucleus in 1911 ([26]) and nuclear reactions in 1917 ([27]). Nuclear physicists started needing energetic particle beams for their experiments in order to investigate the structure and mechanisms of nuclei. Since those times particle accelerators have always been an important means serving experiments in nuclear and particle physics as well as other areas in physics and later in medical and industrial applications. In 1930 the first Cockcroft-Walton accelerator produced a proton beam of 200 keV and

in 1932 an upgraded machine provided a 600 keV beam ([28]) which was used for the first nuclear reaction induced by an accelerated particle beam, the transmutation of Lithium to Helium (see Figure 1.1). In parallel to the voltage multiplying rectifier con-

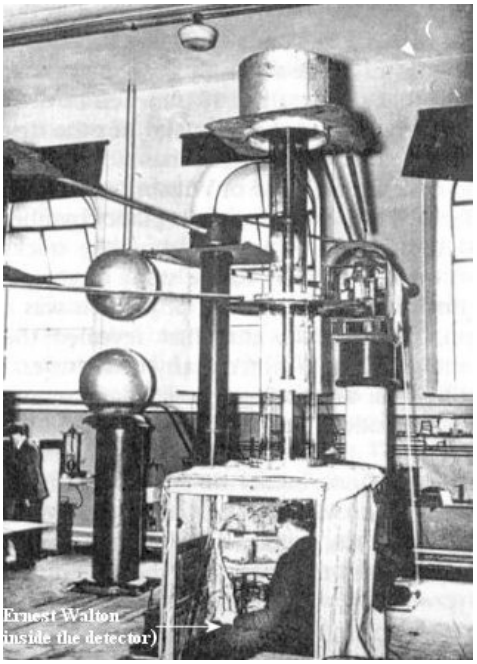

Fig. 1.1: The original accelerator which Cockcroft and Walton used for their experiment discovering the beam induced ^{7}Li(p,α)^{4}He reaction in 1932. The ion source is located at the top and the target and detector at the bottom. Photo from the museum at the Cavendish Laboratory in Cambridge (www.cambridgephysics.org/museum)

cept of Cockcroft and Walton in England, American physicist Robert Van de Graaff experimented with belt driven machines at Princeton University. He created a voltage of 1.5 MeV in 1931. In 1932, then in Washington DC, he produced a proton beam with an energy of 600 keV. From that time on belt driven machines were outperforming the multiplier based ones in terms of energies. All subsequent steps to push the energy frontier were done with those belt driven machines and later on with Pelletrons. During the 1930's the concept of enclosing the accelerators in pressurised gas was developed by Ray Herb as well as the use of a potential grading structure for the accelerating column. In 1939 a machine which set standards for at least the next decade was commissioned in Wisconsin. Thanks to the new technologies this accelerator was able to

stably operate with beam at 4.3 MeV.

Commercial Involvement in Accelerator Development The Second World War and the Manhattan Project changed the circumstances for accelerator development. The science budgets after the war were hugely increased and the establishment of the High Voltage Engineering Corporation (HVEC) in 1947 marked the entrance of a commercial player into the field of accelerator development. HVEC was involved with a substantial part of high energy electrostatic accelerator installations for the next two or three decades and contributed to many of the technical developments. These include the construction of tandems (first tandem in 1958), the Pelletron drive system and more elaborate grading structures as well as the development of better ion sources and the use of SF_6 as insulation gas. By the 1970's accelerators with beam energies up to 20 MeV were commercially available and in use in many research institutions worldwide.

Attempts at Higher Energies In the mid 1970's and early 1980's a number of projects were started to design electrostatic accelerators which would go beyond 20 MeV. These were machines with large dimensions, requiring dedicated buildings to host them. One example is the electrostatic accelerator at the Daresbury lab in the UK (see Figure 1.2), which started commissioning in 1980. The voltage generator achieved a maximum voltage of 29.5 MeV. For actual operation with particle beams 20 MeV were viable. This accelerator incorporated great new technological concepts, e.g. the laddertron charging system or infrared links for the communication of the control system. It contributed to many successful research projects in nuclear physics, especially nuclear structure. The difference between the voltages achieved with and without points towards a disadvantage of electrostatic accelerators. A similar case is the 25URC accelerator which commenced testing in 1979 at the Oak Ridge National Laboratory. Without the accel-

Fig. 1.2: The building of the large laddertron charged electrostatic accelerator at Daresbury. The terminal with the ion source was at the top and the accelerating column went down the whole tower towards the bottom. The accelerator was shut down in the 1990's. Picture taken from Wikipedia (user: Jotelcommons) under the creative commons licence CC BY-SA 2.0

erating column it reached a voltage of $32 \pm 1.5\,\mathrm{MeV}$, but with beam it could initially only run at 20 MeV. Only years of conditioning and improvements brought it up to 24 MeV. Plans for even higher energy machines, which had existed in the 1970's, were thus abandoned. Those machines with their larger structures and higher voltages would have had enormous stored energies and this was already a problem with the existing machines as sparks often lead to serious damage.

Dominance of Applications for New Developments This period of rather unsuccessful attempts to push the energy barrier with electrostatic accelerators ended the dominance of belt or chain charged accelerators. Subsequently the focus within the field of electrostatic accelerators has moved towards safely and economically operating the existing machines on the one hand and designing smart concepts for lower energy in-

dustrial or medical concepts on the other hand. In parallel to the research applications a wide range of areas emerged where particle accelerators are used. As energy is not the main factor for these purposes, the technology differs from the large belt machines and this actually led to a renaissance of the cascade type voltage multipliers. Cost, reliability and ease of operation are the main parameters for applications like Atomic Mass Spectrometry (AMS), medical devices or implanters for the semiconductor industry. These parameters are the key drivers for innovations in electrostatic accelerator technology. The Novel Electrostatic Accelerator described in this thesis has to be seen in the context of this development.

1.2.2 Key Challenges for Electrostatic Accelerators

In contrast to e.g. linear RF accelerators the scalability of electrostatic accelerators is very limited. Although their technology is basically rather simple compared to RF systems, increasing the design energy leads to a number of key challenges. These have resulted in the fact that the maximum beam energy achieved is around 25 MeV, whereas the majority of research machines runs well below 20 MeV. For industrial and medical machines reliability and practicality play an even more important role and in this field the use of electrostatic accelerators is confined to energies below 5 MeV. This section deals only with those parts of the accelerator which are particularly sensitive to upscaling the energy and does therefore not mention ion sources or stripper systems. A more comprehensive treatment of electrostatic accelerator technology can be found in [29].

Insulating High Voltages Usually the voltage generation as such is not the most challenging part of an electrostatic accelerator. The technology for charging belts, chains or cascade rectifiers is well developed and seems reasonably scalable. However the insula-

tion of the high voltage part of the machine gets more challenging, when increasing the terminal voltage. Traditionally systems are confined in a compressed gas environment, usually SF_6. The higher the voltage, the larger the required tank size to keep the fields below the breakdown strength of the gas. Thus the required tank volume grows more than linear with the voltage. The design needs to have shielding and grading structures in order to prevent field enhancements and to minimise the required volume.

Breakdowns, Stored Energy and Machine Protection Even with an optimal field design occasional breakdowns cannot be completely eliminated, especially during the commissioning phase. Therefore the impact a breakdown would have on the system needs to be taken into consideration for the design. As an electrostatic accelerator is always a capacitive system, the stored energy CV^2 is quadratically proportional to the voltage. As the size of the system grows with its energy the capacitance usually increases too. This leads to enormous amounts of stored energy with the potential of severe damage to any mechanical component as well as to circuit components like resistors or diodes, especially in the case of rectifiers which have an even higher stored energy due to their stacks of capacitors. A number of means to mitigate this have been developed. These include circuit protection in the form of protective resistors and spark gaps as well as corona points and dedicated spark gaps to initiate controlled breakdowns before uncontrolled breakdowns occur with their unpredictable potential for damage. Nevertheless the immense stored energy of electrostatic accelerators has proven a limiting factor for the scaling towards higher energies.

Beam Tube The accelerated particle beam needs to propagate in vacuum. This constitutes the need for a beam tube, i.e. a vacuum channel in the centre of the accelerator. This beam tube is a very vulnerable part of the system in terms of breakdown as it does

not profit from the advantages of pressurised gas insulation. The surface breakdown strength of beam tube insulators can be increased by convoluted geometries and can reach similar values as the SF_6 insulation, however it is very sensitive to radiation. Secondary electrons and stray ions play a major role in the induction of breakdowns along these surfaces. Unfortunately these effects do not only depend on the field strength but also on the terminal voltage of the machine. Secondaries can be accelerated along substantial parts of the column and therefore gain high energies. Different methods to capture secondaries and stray ions before they gain too much energy have been developed. Most of them use relatively weak transverse fields which must be strong enough to deflect secondaries on collectors but not so strong as to impact the actual beam too much. Despite these concepts breakdowns along the inner surface of the beam tube have always been a major problem and are in fact one of the main stumbling blocks towards larger scale electrostatic accelerators.

The novel electrostatic accelerator discussed in this thesis overcomes some of the main problematic areas mentioned in this section by a different design approach. The concentric shell system with the terminal in its centre provides all the grading which is needed for a uniform field distribution. As the whole voltage generation system operates in vacuum, there is no need for a beam tube and the various problems related to beam tubes are therefore avoided. The graded fields with a large number of concentric electrodes keep the stored energy reasonably low, nevertheless appropriate circuit protection is required to preserve the diodes and resistors in the voltage multiplier.

1.2.3 Cockcroft Walton Rectifiers / Voltage Multipliers

While most electrostatic accelerators at the high energy end are driven by belt or chain charging systems, voltage multipliers have always played an important role for accelerators in the lower energy range, especially in industrial environments. They do not have any mechanical parts and thus are reliable and easy to operate. Furthermore they are capable of delivering high currents of hundreds of mA and hence hundreds of kW whereas belt driven accelerators are confined to about 1 mA per belt and chain driven ones to 150 µA per chain (see [29]). This section gives a brief introduction to multiplying circuits and some of their properties.

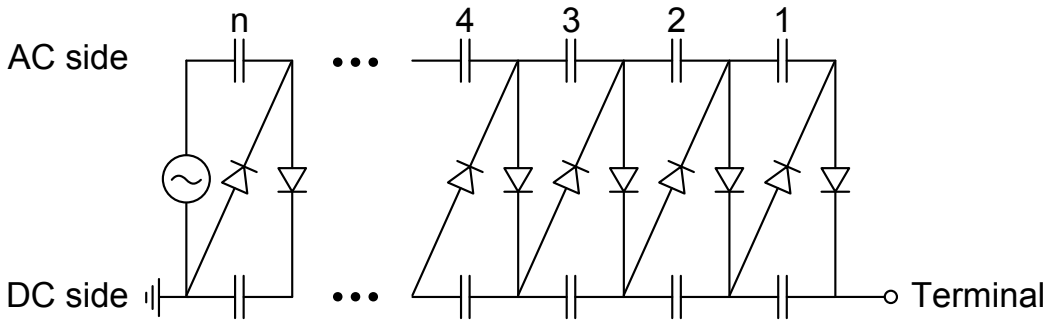

Fig. 1.3: Schematic of a Cockcroft Walton Rectifier with n stages.

The circuit used by Cockcroft and Walton in their first accelerators is the asymmetrical cascade which was invented by Swiss physicist Heinrich Greinacher ([30]) more than 10 years before Cockcroft and Walton's famous experiment in 1932. It consists of two stacks of capacitors, each stack being a series of capacitors, which are interconnected by rectifying diodes (see Figure 1.3). One stack is connected to ground, the other to an AC voltage $V(t) = V_0 \cdot \sin(\omega t)$. With the interconnecting diodes allowing the charge only to flow in one direction, i.e. up the stack, all the capacitors get charged with the same polarity. Charge is transferred from one capacitor to another during one part of the AC cycle and the first capacitor is recharged during the second part of the

cycle. The whole system of capacitors gets charged up to its maximum voltage over a number of AC cycles after switching on the power supply or changing its output voltage. In the case of no load and ideal diodes without recovery times or resistances and no stray capacitances in the system the capacitor closest to ground on the AC stack (named n in Figure 1.3) gets charged up to a voltage of $V_{C1} = V_0$ and all the other capacitors in both stacks get charged to the voltage $V_C = 2 \cdot V_0$. For a system with n stages, i.e. n capacitors in series in each stack, this leads to a terminal voltage on the DC side of the system given by:

$$V_{Terminal} = 2n \cdot V_0 \tag{1.9}$$

In principle one could add as many stages as one would like to, however insulation, realistic diode behaviour and stray capacitances put a limit to this in a real machine.

Voltage Drop and Ripple with Load As soon as a load is connected to the terminal a current starts flowing from the highest capacitor of the stack (C_1). This capacitor then needs to be recharged from the next lower stage and the charge flowing through the load needs to travel through the whole cascade, therefore lowering the voltage across each capacitor. The average voltage drop with a load current I_{load} in a cascade with n stages is given by

$$\Delta V = \frac{I_{load}}{2f} \sum_{k=0}^{n-1} (k+1) \left(\frac{2k+1}{C_{2k}} + \frac{2k+2}{C_{2k+1}} \right) \tag{1.10}$$

Note that the numbering of capacitors starts at the terminal, i.e. increasing the capacitances of the higher stages near the terminal reduces the voltage drop less than increasing the capacitances of the first stages near the AC drive. The peak to peak

ripple is given by

$$\delta V = \frac{I_{load}}{f} \sum_{k=0}^{n-1} \frac{k+1}{C_{2k}} \tag{1.11}$$

Note that the ripple due to a load only depends on the capacitances of the DC column of capacitors. In a system where all capacitors have the value C one can solve the sums in Equations 1.10 and 1.11 and obtains

$$\Delta V = \frac{I_{load} n}{12fC}(8n^2 + 9n + 1) \tag{1.12}$$

and

$$\delta V = \frac{I_{load} n}{2fC}(n + 1) \tag{1.13}$$

Note that many authors subtract half of Equation 1.13 from Equation 1.12 in order to obtain the minimum voltage drop during a cycle (e.g. [29] and [31])

Stray Capacitances Stray capacitances between the AC side capacitors and any of the DC capacitors or ground lead to voltage drop and ripple due to reactive currents. Note that this ripple and voltage drop is present even without a load. Using a transmission line approach Everhart and Lorrain (see [32]) calculated the efficiency $F = V_{output}/2nV_0$ of a multiplier with several stages with the same capacitance C and shunt capacitance C_{shunt} parallel to the rectifier for each stage

$$F = \frac{1}{2n}\sqrt{\frac{C}{C_{shunt}}} \tanh\left(2n\sqrt{\frac{C_{shunt}}{C}}\right) \tag{1.14}$$

and the ripple is given by

$$\delta V = V_0 \left[1 - \operatorname{sech}\left(2n \sqrt{\frac{C_{shunt}}{C}} \right) \right] \tag{1.15}$$

Note that this approach does not include stray capacitances to ground or between different stages of the multiplier. The effect can be mitigated by use of inductors either in series with the capacitors or between the highest voltage points of the AC and DC column, [32] gives a detailed theory of this. Another way of mitigating reactive currents and also substantially decreasing the voltage drop from load currents is the use of a symmetrical circuit, i.e. two AC columns with a phase shift of 180° between the to AC drive voltages, see [33].

Diode Forward Voltage and Diode Recovery Charge The forward voltage drop of the diodes causes a drop in the output voltage ΔV_{diodes} which according to [33], grows linearly with the number of stages n. For modern diodes the forward voltage drop is three orders of magnitude smaller than the maximum reverse voltage capability and therefore this effect does not play an important role. The diode recovery charge could be treated in a similar way as the reactive currents from the shunt capacitance. An extra value $C_{recovery}(V_0) = Q_{recovery}/V_0$ would have to be added to C_{shunt} in Equations 1.14 and 1.15.

2. THE NOVEL ELECTROSTATIC ACCELERATOR PROGRAMME AT RAL

2.1 Introduction to the Concept

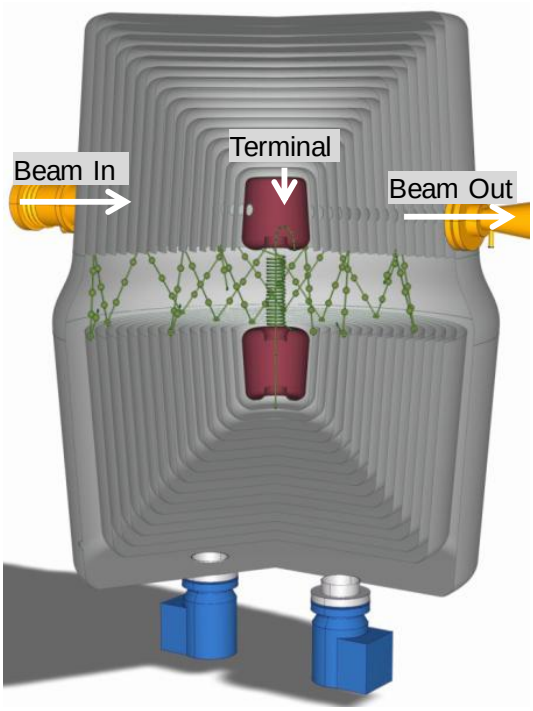

Fig. 2.1: Schematic setup of the novel accelerator. Figure taken from Siemens internal documents and modified with their permission.

The novel accelerator concept employs a voltage multiplier circuit similar to the Cockcroft-Walton cascade in order to transform an AC voltage into a higher DC voltage. However, in this concept the capacitances of the Cockcroft-Walton cascade are represented by two sets of concentric hemispherical metallic shells. This geometry is very beneficial, as the shells act as capacitors, as shielding for the electrostatic fields and as a beamline. It will therefore be able to provide much higher gradients than

conventional Cockcroft-Walton accelerators whilst keeping all the advantages. The accelerator will have its highest electrostatic potential in the centre of the accelerator itself (so called terminal), which will be shielded by all subsequent sets of shells. It will be operated in tandem mode. A negative ion source is placed on one side of the accelerator and the beam is extracted on the other side of the accelerator. The charge of the beam has to be changed in the centre of the accelerator via charge stripping with a carbon foil (see Figure 2.1 and Figure 2.2 for more details on the setup).

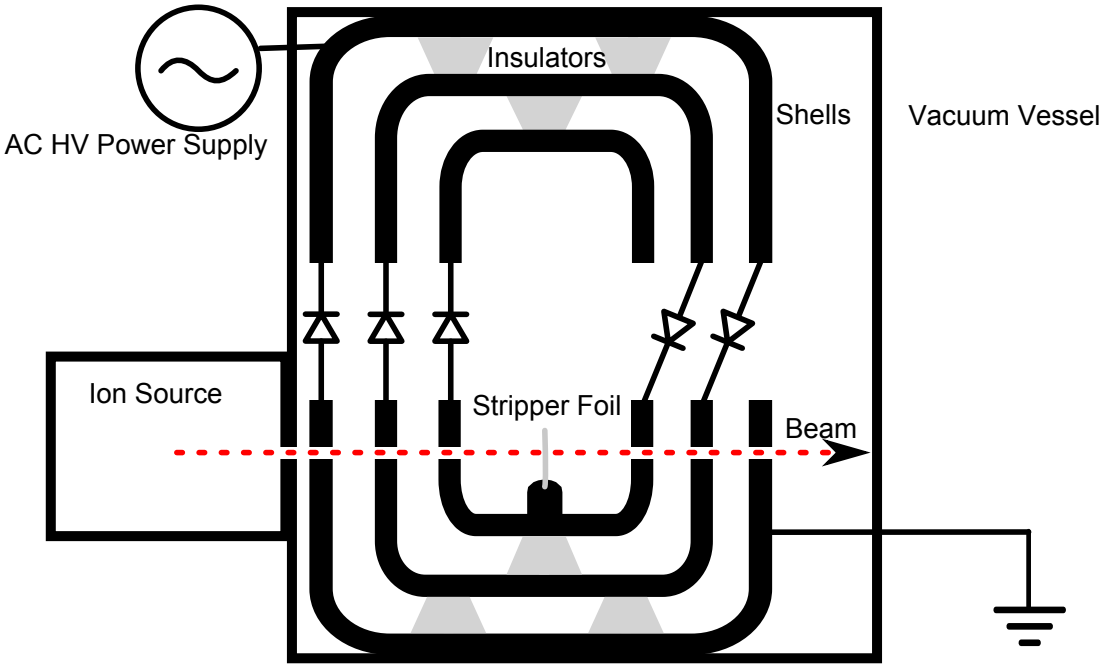

Fig. 2.2: Schematic setup of the novel accelerator. Two sets of shells (3 each to simplify the diagram, in a full scale machine this could be up to 40) are interconnected by diodes. The lower shell set has a series of holes, through which the beam is accelerated. The stripper foil in the centre changes the polarity of the beam from negative (as coming from the ion source) to positive.

The circuit of this setup is still exactly the same as in a conventional Cockcroft Walton accelerator. This is achieved by interconnecting the metallic shells of the bottom and top shell set with diodes in the right fashion. The shells themselves need to be spaced from their neighbouring shells by suitable high voltage insulators. The novel accelerator aims at gradients as high as $10\,\mathrm{MV\,m^{-1}}$ which is ambitious for a DC

accelerator. It is therefore crucial that the design of all components support these high fields. The shape of the shells grades and defines the fields and the field strength at any point of the system and is hence important. The inter shell insulators are generally the weakest point of the system in terms of voltage breakdown. The diodes are a very vulnerable component as they have to operate in vacuum and in high electric fields and at the same time are exposed to extreme transient currents during electric breakdown. Hence the three aforementioned components are the most crucial components for successfully creating field gradients of the desired magnitude in a system of the described sort. A lot of work, both theoretically and experimentally has been put into their design, testing and development.

Electrostatic accelerator concepts with nested electrodes have been around for some time. The Budker Institute in Novosibirsk have built and operate successfully a 2 MV proton tandem accelerator for currents of tens of mA (see [34]). In this accelerator nested electrodes in vacuum are used for the voltage grading and shielding as well as functioning as a beam tube. However the voltage itself is supplied by an external voltage source and connected to the shells via a feedthrough. Furthermore the voltage gradient in the machine at BINP is several times lower than in the proposed novel electrostatic accelerator, leading to a much larger footprint. In a number of patents (e.g. [35]) R. J. Adler has proposed the use of a nested structure for the creation of high voltage as well as its insulation. Suggested means of creating the voltage within each stage are batteries, induction from an external magnetic field, an insulated mechanical shaft, heat or cascade generators (see also [36]). Using this concept, electron and ion accelerators have been built by Applied Energetics, Inc. and are sold commercially. These machines are currently limited to 1.5 MV (see [37]). They use solid insulation for

part of the system and the accelerating structure operates at lower gradients than the novel electrostatic accelerator. However, it has never before been proposed to use the capacitances of nested vacuum electrodes as capacitor columns within the Cockcroft Walton circuit. The voltages would always be created by external power supplies, requiring appropriate feeds and connections and thus limiting the gradients and voltage of such systems as well as increasing their size. The novel electrostatic accelerator proposed by Siemens uses the electrodes themselves to create the high voltage and therefore does not need any external high voltage apart from a suitable high voltage AC power supply. It thus promises to be the starting point for electrostatic accelerators with an unprecedented combination of high gradients and very small footprint. This opens opportunities for a number of applications, especially radioisotope production for nuclear medicine.

The concept of the novel accelerator was invented by Prof. Oliver Heid of Siemens AG, CT NTF HTC, Erlangen. A substantial amount of theoretical work on the concept has been done by him and his group in Erlangen in order to move towards a real machine for medical radioisotope production. In order to replace compact cyclotrons currently in use, the minimum requirements for such a machine are a beam energy of about 8 MeV and beam currents of at least 100 µA. This could be realised with a tandem system of e.g. 40 stages of 100 keV each and a terminal voltage of 4 MV.

Siemens AG has decided to build a first prototype to test the various components and prove the feasibility of the proposed system. For this purpose Siemens teamed up with STFC at the RAL lab as well as with the John Adams Institute at the University of Oxford. The first stage of the prototype programme is a 7-shell prototype (i.e. six multiplier stages) with 1 cm gap spacing. The goal is successful extraction of a proton beam from this system, aiming at the full scale system specifications of 100 µA current

and gradients of up to 100 kV per stage. This would result in 600 keV terminal voltage and proton beam energy of 1.2 MeV. Generally all the components used in this system should be suitable for the full scale system. It is one of the objectives of the 7-shell prototype to test and validate every system component to prove its adequacy for a full scale commercial system. Of course a full scale system has different capacitances due to the larger dimensions of the outermost shells. This had to be taken into account for the AC drive system in terms of an additional parallel capacitor which simulates the capacitance of the additional shells. Also the stored energy of the largest shells in a full scale system would be higher. This mainly affects the diode protection system which therefore needs to be robust enough to be able to handle stored energies slightly higher than those present in the 7-shell system.

The work which I have done for this thesis focuses on the development and testing of the 7-shell protoype and its components, in particular the ion source, stripping system, AC power supply, insulators, diodes, beam diagnostics and the control system.

2.2 Concentric Shells

The shells for the 7-shell prototype have been spun from stainless steel with a maximum thickness of 2 mm at the bottom and receding thickness towards their edges. This process is rather expensive and the resulting shells have a considerable weight. Both the choice of material and the fabrication method are an interesting and important research topic pursued by Siemens' CT NTF HTC research team which however is not addressed in this thesis. Current suggestions include metals as well as organic materials which could be covered with a thin metal layer. The geometry of the shells needs to take into account the resulting field distribution, the achieved capacitances,

the placing of inter shell insulators and of course the beam line. For the prototype a flat bowl shape with vertical walls and a spacing of 1 cm between any two shells has been chosen (similar to the shells in the schematic of Figure 2.2). On the innermost and outermost shell flares can be beneficial, as they relieve the fields in the equatorial gap between the upper and lower shell set. Flares have not been present for all of the experiments and were only added on later iterations. They do not play any role for the results presented in this thesis. The choice of the distance between each shell has many implications. It determines the number of overall shells as well as the capacitances between the shells and has therefore an important impact on the efficiency of the CW circuit . Also for gaps larger than a few mm the breakdown fields of both the metal electrodes and inter shell insulators decrease with gap distance (see e.g. [38] and [39]). On the other hand very small gaps are not practical in terms of space consumed by the metal, the matching of higher tolerances and the placing of insulators and diode chains. The gap spacing of course also determines the voltage per gap and thus the input voltage of the AC power supply. The optimum gap spacing is subject to research by Siemens' CT NTF HTC team and will not be addressed in this thesis. The size of the innermost shell determines the size of the overall machine and the inter shell capacitances. The innermost shell of the beam side of the machine also needs to contain the stripper system. In our prototype system the innermost shell has a diameter of 30 cm. A series of beam holes has been cut through the shells, on the injection side, these have 1 cm diameter, only the first hole is larger, i.e. 5 cm. On the extraction side there is a series of holes with 2 cm diameter. The shells also have suitable holes on the bottom for the fixing of inter shell insulators. The alignment of the shells is important to achieve uniform field strength and also to achieve alignment of the beam holes.

2.3 The CW Circuit

The multiplier circuit consists of the inter shell capacitances and the diodes connecting them. The 7-shell prototype has a column of six capacitors on each side and therefore an ideal multiplication of six times the Peak to Peak input voltage. The capacitances between the shells have been measured and are in the range of approximately 200 pF to 300 pF as expected theoretically from a simple calculation assuming parallel plate capacitances. As explained in Section 1.2.3 beam loading introduces ripple and voltage drop to the system. This effect is inversely proportional to capacitance and operating frequency. The rather low capacitances of the system therefore require a rather high operating frequency and for the prototype programme a frequency of about 100 kHz has been chosen. Stray capacitances lead to additional voltage drop at each stage and introduce ripple even without beam loading, furthermore the diode forward voltage drop and diode recovery can introduce further output voltage decrease and ripple. These effects have been analysed in some depth by O. Heid ([40]), however the purpose of this thesis is neither their theoretical nor their experimental analysis, the focus is rather on proving the general feasibility of the proposed system. An optimisation of the circuit to minimise adverse effects could be part of a later stage of the research programme.

2.4 AC Drive for the CW Circuit

With the chosen gap distance of 1 cm the power supply needs to be capable of delivering an input waveform with a Peak to Peak voltage of at least 100 kV at a frequency of about 100 kHz. Furthermore it should be compact and should have low stored energy to limit the damage in cases of voltage breakdowns. For this purpose an air core resonant

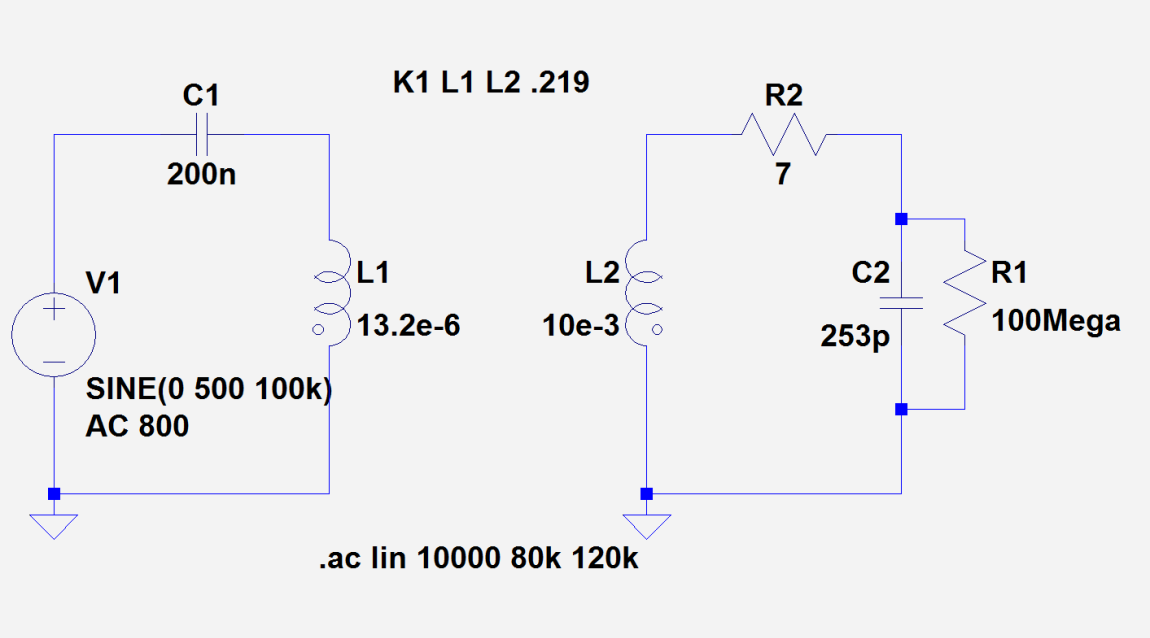

Fig. 2.3: The circuit of the resonant transformer used for modelling in LTspice IV. Primary and secondary are only loosely coupled (≈22 % field overlap).

stepup transformer has been designed and manufactured by Siemens' CT NTF HTC research team in Erlangen and subsequently commissioned at RAL (see Section 3.1). The primary coil of the transformer is in series with a capacitance, thus forming a series LC circuit with the resonance frequency being the desired output frequency. Together with the capacitive impedance of the 7-shell circuit the secondary coil of the transformer forms an LC circuit which should have the same resonance frequency as the primary side, i.e. 100 kHz. The transformer was designed for a 40-shell full scale system which has larger capacitance than the 7-shell system. Thus an extra parallel capacitance has been added inside the transformer secondary side in order to match the frequency. See Figure 2.3 for the circuit of our transformer with the approximate design properties. I have modelled the circuit using the widely known circuit modelling engine SPICE ([41]), in particular the LTspice IV tool ([42]). Each individual side would have a series resonance (i.e. the resonance is caused by a capacitor and an inductor in series. The impedance of such a circuit is near zero and thus draws large currents from the AC source, increasing the stored energy further and further until one of the components

gets damaged) at ≈100 kHz, the coupled circuit has two series resonances at about 90 and 112 kHz and a parallel resonance (i.e. the resonance is caused by a capacitor and an inductor in parallel. The impedance goes toward infinity and the current thus towards zero. The stored energy is limited by the input voltage) at 100 kHz. The series resonances cause extreme voltages and currents on both the primary and secondary side and are therefore to be carefully avoided. The parallel resonance at 100.06 kHz has low voltages and currents on the primary side. The voltages across inductor and capacitor are of the order of the drive voltage and the currents of the order of a few A. The current on the primary side strongly depends on the load on the secondary side (e.g. breakdown currents or beam loading), in our circuit represented by the 100 MΩ resistor. With an input voltage of 800 V Peak to Peak the secondary voltage at the resonance point of 100.06 kHz is about 100 kV the transformer ratio being ≈ 125 : 1. With no resistive load at all the primary side current is of the order of 2.2 A and the reactive current on the secondary side 16 A. As to be expected a 1 mA resistive load on the secondary side increases the primary current by 125 mA. See Figure 2.4 for the frequency response of the voltages obtained from the SPICE simulation.

As the whole system aims at commercial viability, an off-the-shelf power supply which is normally used for induction heating has been chosen to provide the input voltage for the transformer primary (see Figure 2.5). This power supply provides voltages up to 2000 V Peak to Peak and usually uses feedback from its load in order to always tune to the resonance frequency. An appropriate feedback system for our transformer had to be developed in order to operate it (see Section 3.1), as the standard feedback system did not work. The transformer used in our experiments has a toroidal coil design, the toroid sitting in a large aluminium box for shielding. The output comes through a hole in the box to be connected to the vacuum feedthrough. This design

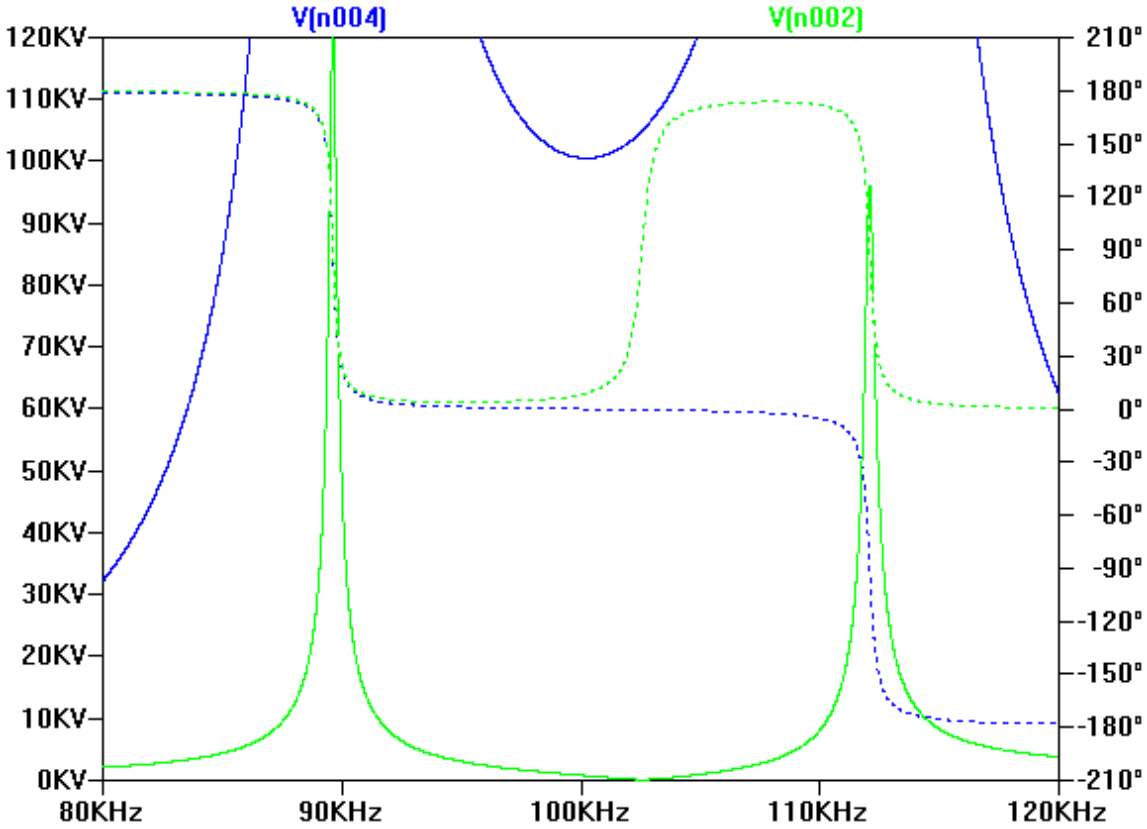

Fig. 2.4: Frequency response of the coupled transformer circuit (LTspice IV simulation). The plots depict the amplitudes (full lines, left y-axis) and phases relative to input voltage (dotted lines, right y-axis) of the voltages across the transformer inductances as a function of the input voltage frequency (x-axis) at a constant sinusoidal input voltage of 500 V. All voltages are RMS values. The green plots (V(n002)) are for the primary winding inductance and the blue plots (V(n004)) are for the secondary winding inductance. Note the dangerous resonances at 90 and 110 kHz as well as the useful resonance at 100 kHz, where the output voltage is 100 kV

Fig. 2.5: The AC power supply by TRUMPF Hüttinger GmbH + Co. KG. It covers the frequency range of 20 kHz to 100 kHz and has an output power of up to 20 kW. The maximum Peak to Peak output voltage is 2 kV. It uses feedback from its load to determine the resonance frequency.

has been successfully operated (see Chapter 3), however more compact transformer designs are being developed to move closer towards the goal of a very compact single room machine.

2.5 Diodes

The diodes for the accelerator need to be fast enough in terms of their reverse recovery time (t_{rr}). As the drive frequency is around 100 kHz t_{rr} should not be more than a few hundred ns, otherwise every multiplier stage will lose voltage on its diode through reverse conduction. Furthermore the reverse currents will lead to an extra thermal load. Also the diodes need to be robust enough to withstand the currents. Currents during operation are very low, of the order of a few hundred µA, however surge currents during breakdowns can be of the order of tens of A. High power diodes which can take these currents do actually exist, however current capability usually corresponds to junction capacitance. The high capacitances of those diodes would act as stray capacitances between the two columns of the multiplier and thus severely undermine the performance. The diodes therefore definitely need a protection system against surge currents. The most straightforward way to do this is a current limiting resistor in series with the diodes, for a detailed discussion see Section 3.4. As most off-the-shelf high voltage diodes are limited to reverse voltages of 10 kV to 30 kV a number of diodes need to be used in a series in order to match the input voltage Peak to Peak of 100 kV. It is therefore important that the diodes have consistent capacitance and reverse leak conduction so that the voltage distributes equally across the chain. Most modern diodes fulfil this criterion. Another important aspect is of course the physical size of the diodes as the diode chains need to fit into the hemispherical gap between the top and bottom shell set. We have explored three ways of joining the

diodes together into a chain: Soldering, crimping and connecting beads. The soldering is bad for use in vacuum. Crimping always involves sharp edges which are bad in high voltage environments. We therefore developed copper beads with a round surface and a hole for the diode leads. They also have screws to fix the leads in the bead. Figure 2.6 shows a diode chain made up with copper beads as used in our prototype. See Table 2.1 for an overview of potentially suitable diodes, we have assessed a couple of them in our experiments, i.e. HVRT300 and UX-F2CL15, see Chapter 3.

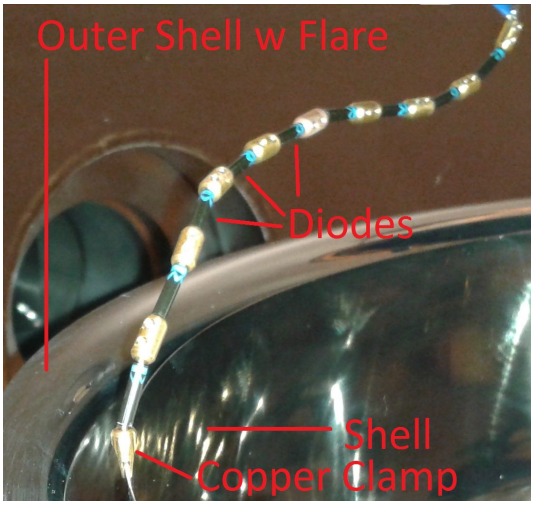

Fig. 2.6: A typical diode chain. The picture shows two shells, a flared one and an unflared one sitting inside it. A diode chain is connected to the inner shell via a copper clamp which is clamped onto the edge of the shell. The individual diodes are interconnected with copper beads.

2.6 Insulators between Shells

The insulators between the shells are stressed to the technological limits. They need to be capable of permanently withstanding DC fields of at least $10\,\mathrm{MV\,m^{-1}}$. At the same time they have to serve the purpose of holding together the top shell set. Alternative designs where the top shell set sits on a tripod insulator which in turn sits in the centre bottom shell have been evaluated, however these were very vulnerable to secondary radiation and thus frequent breakdown and have therefore been abandoned

Diode	V	L	t_{rr}	I_{surge}	I_{rect}	I_{rev}	V_{forw}	C_{junc}
K100 UF	10 kV	6.5 mm	100 ns	100 A	1500 mA	2 µA	14 V	35 pF
ZR100 FF3	10 kV	11 mm	30 ns	9 A	150 mA	1 µA	32 V	8 pF
MR140 FF5	14 kV	9 mm	50 ns	0.5 A	10 mA	0.1 µA	50 V	0.5 pF
NTE517	15 kV	22 mm	100 ns	50 A	550 mA	5 µA	14 V	n/a
BT757	20 kV	10 mm	100 ns	25 A	25 mA	2 µA	45 V	n/a
X200 UFG	20 kV	10 mm	100 ns	2 A	25 mA	1 µA	30 V	2 pF
BT933	20 kV	18 mm	100 ns	100 A	200 mA	10 µA	32 V	n/a
G30FP	30 kV	12 mm	100 ns	3 A	10 mA	0.2 µA	55 V	n/a
2CL2FP	30 kV	15 mm	100 ns	10 A	220 mA	2 µA	52 V	15 pF
HVRL400	40 kV	15 mm	100 ns	3 A	30 mA	2 µA	50 V	0.6 pF
HVRT300	30 kV	12 mm	100 ns	3 A	30 mA	2 µA	45 V	1 pF
JB289	35 kV	15 mm	100 ns	10 A	100 mA	2 µA	55 V	15 pF
HVEF12P	12 kV	10 mm	20 ns	3 A	20 mA	0.2 µA	27 V	0.25 pF
UX-F2CL15	15 kV	15 mm	50 ns	20 A	150 mA	0.5 µA	16 V	3.5 pF

Tab. 2.1: Potentially suitable diodes for the accelerator

(see Chpater 3). The basic material used for the tested insulator designs at the Siemens prototype is PEEK, which has a bulk breakdown strength of more than $20\,\mathrm{MV\,m^{-1}}$. However, the main breakdown mode for insulators is surface discharge and these start at lower voltages than the bulk breakdown limit. In fact the breakdown limit of two metal electrodes is always lower with an insulator than without [39]. The insulators will therefore always be the weakest point in the system, unless the shell spacing is increased at the location of the insulators.

A lot of research has been done on the physics of surface discharge on insulators in vacuum. The common theory is that breakdowns evolve in three steps: Initiation, development and discharge. Most researchers agree that the initiation of the discharge has to do with electrons mainly emitted from the cathode side triple junction between metal, vacuum and insulator. Opinions differ about the second stage, in fact C. Miller

[39] suggests that whilst the different mechanisms proposed might all be involved at the same time, the prevalence of one of them depends on details of the design and material of the used insulator. The third stage of the surface breakdown, the discharge, takes place either on, near or inside the surface of the insulator. A common theory is that the discharge flows inside a small layer of gas desorbed from the surface of the insulator.

Efforts to increase the voltage standoff of insulators have been made by many researchers and address different aspects of the development of a discharge. Cone shaped insulators have turned out to have a much higher breakdown voltage than cylindrical ones, with the ideal cone angle being 45°. The effect is much less for dc than for short pulses, however the experimentally determined improvement of 30 % [43] to 40 % [44] is still large enough to play a role. A contrary result is reported by Jaitly and Sudarshan [45]. They found that a negative cone angle of 50° to 60° was best. However they used 9.2 mm thick plexiglass insulators compared to the 2 mm thick ceramic insulators used in [43]. They also tried 55° chamfers on the edges of the wider side of the cone, which considerably increased the voltage standoff of both negative and positive cone angles. Also with the chamfers the positive cone angles turned out to have a higher performance than the negative ones, with the conditioned breakdown voltage for the 9.2 mm gap exceeding 100 kV for any cone angle between 40° and 60°. Our insulator design therefore roughly follows the one tested by Jaitly.

Length and diameter of the insulator play a role as well. The diameter should be as small as reasonable, as the diameter increase leads to decrease in breakdown voltage (e.g. [46]). It is not easy to quantify the effect. The experiment done by Pillai in [46] compares breakdown voltage for 2 mm thick insulators of different diameters, where the diameter reduction from 12.7 mm to 2 mm led to an increase in breakdown voltage of 17.5 %. Increased length of the insulator does of course increase the breakdown

strength, however it does not scale 1:1, but rather $V_{\text{breakdown}} \propto L^{0.5}$ as measured for insulators thicknesses of 2 mm to 8 mm in [46] and for 5 mm to 15 mm thick insulators in [47].

Many efforts concentrate on the triple point, especially on the cathode side, as this is the source of electrons which start the discharge. Very small gaps between the insulator and the metal surface lead to field enhancement in that gap, due to the higher permittivity of the insulator compared to vacuum. This effect can be counteracted by introducing a gradient of permittivity in the insulator. A different approach is the reduction of the fields in the triple junction by recessing the ends of the insulator in the electrode, by the use of field shaping metal inserts in the insulator or by the use of shields. Of course improving the interface between insulator and metal, i.e. making it as smooth and tight as possible, helps as well.

Surface charge is part of some of the theories for the development of discharges. Some researchers have tried covering their insulators with thin layers of highly resisitive materials to prevent surface charging. This yielded an improvement, e.g. in [48] the Cu_2O (200 nm) coated version of a 12.7 mm high alumina insulator immediately reached a DC standoff of 65 kV where as the uncoated version of the insulator would need 8 conditioning flashovers to reach the same voltage standoff. However after the conditioning both insulators would be equal.

Other factors for breakdown strength are choice of material, material homogeneity, permittivity and surface roughness. Generally the material should be as homogenous as possible without any enclosures. For a more detailed discussion see [39] and the references mentioned therein. Also bakeout of the insulators has proven beneficial. During operation however the insulator temperature should be kept as low as possible, as temperature increase leads to reduced strength.

Conditioning of the insulators is an important process as it increases the voltage standoff. However it always bears the potential of damage to the insulator surface and should therefore be carried out gently and slowly. For this purpose I developed a dedicated conditioning process for the prototype and implemented it in the control system in order to be run automatically. For a detailed description of this system see Section 3.3. In his review [39] Miller mentions that the conditioned state of a system can deteriorate if the system is left without voltage for an extended amount of time. Another conditioning procedure might become necessary then. This practical aspect needs to be considered for the operation of potential medical accelerators.

2.7 Ion Source

Introduction

To provide a suitable negative ion beam for the prototype, a very compact so called filament cathode cusp volume ion source has been designed. It is roughly based on the design of the Culham ion sources [49]. A major design goal was the beam matching to the beamline consisting of the holes in the shells. This avoids the necessity of a Low Energy Beam Transport (LEBT) section, therefore hugely contributing to the compactness of the whole system.

The ion source produces H^- ions in a hydrogen plasma, which is contained in a magnetic field (see Figure 2.7 for a schematic of the different regions and the location of permanent magnets in filament cathode cusp volume ion sources). The plasma is divided into two regions by a transverse magnetic filter field, a hot and a cold region . The plasma in the hot region is ignited and maintained by a discharge current between a heated tungsten filament cathode and the walls of the source volume itself. The cold region serves the formation and extraction of H^- ions, which are protected from hot

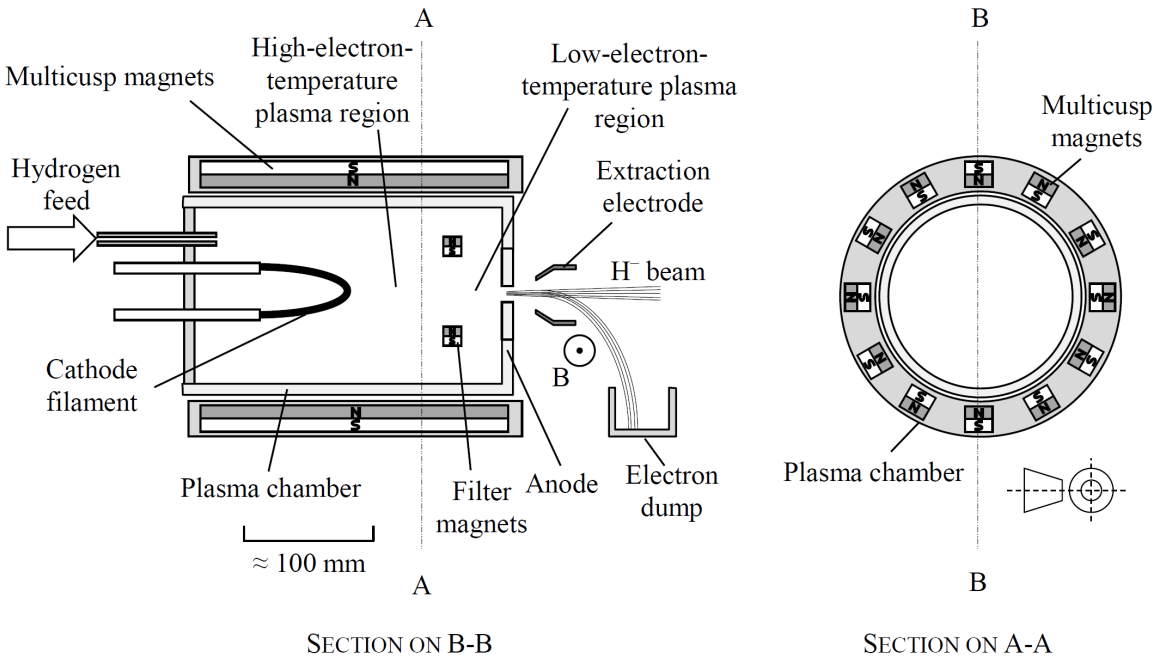

Fig. 2.7: Schematic of a filament cathode multicusp volume source, taken from [1] with the author's permission. The Siemens ion source does not have filter magnets inside the plasma chamber as shown in this schematic. The filter field is created by an asymmetry of the multicusp magnets, see Figure 2.8 for an actual cross section of the Siemens ion source.

electrons and protons by the filter field. The plasma is fuelled by a constant inflow of hydrogen from a pipe and pumped by a vacuum system on the other side.

In the Siemens ion source the extraction of H^- ions from the cold plasma region is done with a set of three subsequent extraction electrodes (as can be seen in the cross section of the Siemens ion source in Figure 2.8). Another transverse magnetic field deflects extracted electrons onto the first and second extraction electrode.

The voltages of the extraction electrodes (See Figure 2.9 for detailed explanations) do not only influence the amount of extracted current, they also work as a focusing element and therefore shape the extracted beam. Other important ion source parameters are the hydrogen flow from the gas inlet and the voltage and current of the plasma discharge between the cathode and the walls.

The following sections expand on the physics processes of the ion source as well as on the specific design of the Siemens ion source.

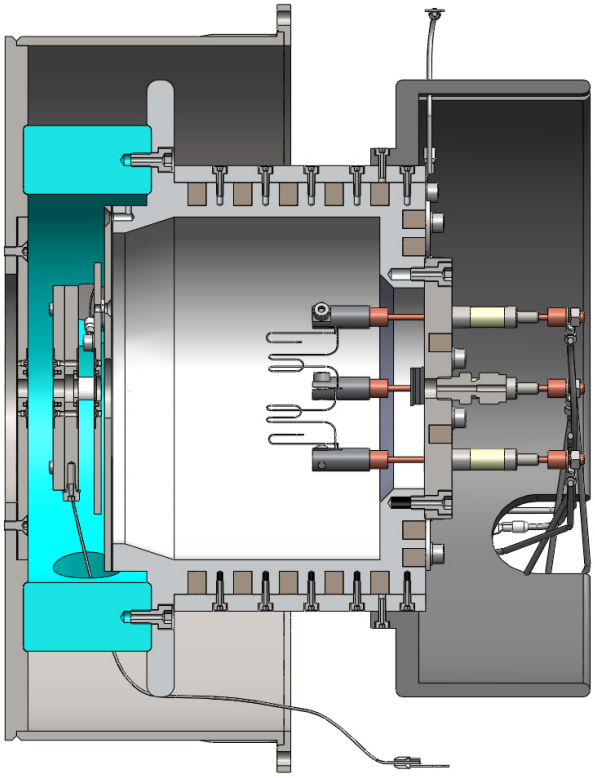

Fig. 2.8: Cross Section of the Siemens ion source. The source can have up to five different filaments to increase maintenance intervals. The filter field is created by an asymmetrical arrangement of the permanent magnets in the walls of the plasma chamber.

H^--Production

There are two processes that are usually exploited for the production of H^- in ion sources. One is called surface production and the other one is called volume production. Surface production relies on interactions between plasma particles and the electrodes. As a result of these interactions an H^- ion is formed. Those interactions are rather complex and far from completely understood [1]. However the work function of the electrode surface plays a key role in this process. The lower the work function, the higher the yield of produced H^-. The so called Caesium Effect discovered in the early 1970's by G. Dimov, Y. Belchenko and V Dudnikov at the Budker Institute in Novosibirsk [50] makes use of this fact. The three researchers added Caesium vapour to their

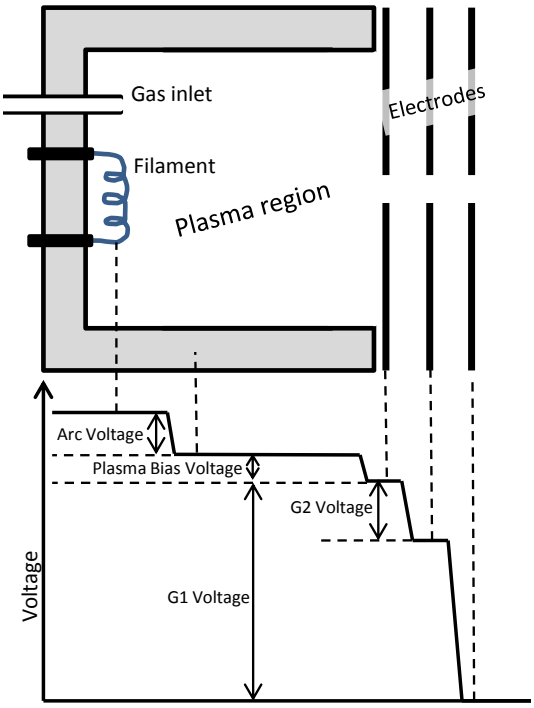

Fig. 2.9: The upper image shows a schematical 2D-cut through the ion source. A discharge current between the filament and the walls of the plasma region ionises the hydrogen which is constantly flowing in through a pipe. The H^- ions are extracted using a series of extraction electrodes. A magnetic dipole field (not displayed) near the extraction aperture filters electrons. They are absorbed by either the first or the second extraction electrode. The lower part of the figure shows the electric potentials (only schematical) of the different parts and how they are referred to in the text. Typical values for the potentials are: G1 10 kV, G2 1.5 kV, arc voltage 100 V, plasma bias voltage 2 V.

gas feed. The Caesium formed a very thin layer on the electrode surface substantially reducing the work function and dramatically increasing the H^- yield. Caesiated H^- sources are now the state of the art in many high power hadron accelerator facilities, however they have a number of disadvantages to do with the requirement of a constant supply of Caesium.

The second production process is the so called volume production. In this process H^- is formed in the plasma volume itself. The use of a transverse magnetic filter field that separates the extraction region (see Figure 2.7) from the hot plasma has substantially increased the extraction of H^- from plasmas. The explanation for this is that H^- is always formed in the plasma volume by dissociative attachment but immediately

Vibrational Level ν	Optimum Impact Electron Energy	Cross Section σ
0	3.75 eV	$2.8 \times 10^{-21}\,\mathrm{cm}^2$
1	3.23 eV	$8.3 \times 10^{-20}\,\mathrm{cm}^2$
2	2.75 eV	$1.0 \times 10^{-18}\,\mathrm{cm}^2$
3	2.29 eV	$7.5 \times 10^{-18}\,\mathrm{cm}^2$
4	1.86 eV	$3.8 \times 10^{-17}\,\mathrm{cm}^2$
5	1.46 eV	$1.2 \times 10^{-18}\,\mathrm{cm}^2$
6	1.08 eV	$2.9 \times 10^{-18}\,\mathrm{cm}^2$
7	0.74 eV	$4.3 \times 10^{-18}\,\mathrm{cm}^2$
8	0.42 eV	$3.2 \times 10^{-18}\,\mathrm{cm}^2$
9	0.14 eV	$4.3 \times 10^{-18}\,\mathrm{cm}^2$

Tab. 2.2: Dissociative attachment cross sections near thresholds for vibrational levels of H_2 molecules. Data taken from [3]

destroyed by hot electrons. The separation of the plasma in a hot and a cold region was seen as a solution to this. However this explanation has been debated a lot as certain effects to do with the plasma and extraction electrodes could not be explained by it [51]. Also extracted H^- currents have often surpassed the expectations of theoretical models (e.g. in [52]). However in 2005 T. Mosbach did two experiments confirming the hypothesis of the formation of H^- by dissociative attachment of rovibrationally excited H_2 molecules [53, 54]. Using laser-induced fluorescence spectroscopy and optical emission spectroscopy he measured the densities of rovibrationally excited H_2 molecules. He also measured the electron energy distribution with a Langmuir probe. Using this data he modeled the expected H^- density in the plasma and compared it with the H^- density obtained from photodetachment measurements with a laser. This confirmed dissociative attachment as the main process for H^- formation.

In a dissociative attachment reaction an electron is attached to an H_2 molecule which then in turn dissociates to yield a hydrogen atom and an H^- ion. With H^-

formation in the extraction region of negative ion sources the H_2 molecules are usually highly rovibrationally excited ($\nu \geq 5$) and the electron energy is low ($E \leq 1\,eV$)[55]:

$$H_2^* + e(E \leq 1\,eV) \quad \rightarrow \quad H^- + H^0 \tag{2.1}$$

The cross section for this process with non excited hydrogen molecules is extremely low (of the order of $1 \times 10^{-21}\,cm^2$ for electron energies below 10 eV [1]. For higher energies it slightly increases [3], but the cross section for the destruction of H^- increases at the same time, thus those electrons are not allowed in the cold region), however rotational and vibrational excitation raises it by up to four orders of magnitude (see Table 2.2).

The rovibrationally excited molecules can be produced in the hot plasma region via collision of electrons with hydrogen molecules. As they are not charged those excited molecules can freely drift through the magnetic filter and interact with cold electrons in the cold plasma region on the extraction side of the source. Proper separation of the two regions thus plays a key role in the ion source design.

The cross sections for vibrational excitations of H_2 molecules in electronic and vibrational ground state via a collision with a low energy electron (i.e. $E < 10\,eV$)

$$H_2(\nu = 0) + e(E \approx 1\,eV \text{ to } 10\,eV) \quad \rightarrow \quad H_2^*(\nu > 0) + e \tag{2.2}$$

peak at a few eV, depending on the excited vibrational level ν as well as on rotational states excited in the same process. The higher ν processes have very low cross sections for their production in this process (see Table 2.3). However, as mentioned above, the rovibrational level for dissociative attachment in the extraction region needs to be $\nu \geq 5$ as the electron temperature there is rather low, i.e. below 1 eV [55]. Of course this depends on the filter field of the particular source as well as the discharge power

Vibrational Level ν	Optimum Impact Electron Energy	Cross Section σ
1	3.23 eV	$5 \times 10^{-17}\,\mathrm{cm}^2$
2	2.75 eV	$4 \times 10^{-18}\,\mathrm{cm}^2$
3	2.29 eV	$4 \times 10^{-19}\,\mathrm{cm}^2$
4	1.86 eV	$9 \times 10^{-20}\,\mathrm{cm}^2$
5	1.46 eV	$4 \times 10^{-20}\,\mathrm{cm}^2$
6	1.08 eV	$1 \times 10^{-20}\,\mathrm{cm}^2$

Tab. 2.3: Cross section for vibrational excitation of H_2 molecules in electronic and vibrational ground state through direct low energy (i.e. $E < 10\,eV$) electron impact. Data taken from [3]

and others parameters. Another possible process to play a role in the production of $H_2^*\nu \geq 5$ molecules is a change of the vibrational state through low energy electron collision via a H_2^- resonance [55].

$$H_2(\nu) + e(\mathrm{E} \approx 2\,\mathrm{eV}) \quad \rightarrow \quad H_2^*(\nu + \Delta\nu) + e \tag{2.3}$$

For the above process however, according to M. Bacal, the most probable change in excitation level is $\Delta\nu = \pm 1$. This would require a very high number of interactions in order to reach states of $\nu \geq 5$ and therefore higher particle densities than usually present in an ion source plasma. W. Kunkel [4] suggested that radiative decay of H_2 electronic singlet states excited by energetic electron collisions might lead to highly vibrationally excited H_2^* molecules in the electronic ground state.

$$\begin{aligned} H_2\left[X^1\Sigma_g^+(\nu=0)\right] + e(\mathrm{E} \geq 20\,\mathrm{eV}) \quad &\rightarrow \quad H_2\left[B^1\Sigma_u^+ \text{ or } C^1\Pi_u^\pm\right] + e \\ H_2\left[B^1\Sigma_u^+ \text{ or } C^1\Pi_u^\pm\right] \quad &\rightarrow \quad H_2\left[X^1\Sigma_g^+(\nu>0)\right] + \nu_{\mathrm{photon}} \end{aligned} \tag{2.4}$$

J. Hiskes has calculated the cross sections for the above processes (see Table 2.4) and estimated the cross sections for similar processes involving higher electronic states

Vibrational Level ν	Cross Section σ
0	$\approx 1.0 \times 10^{-17}\,\mathrm{cm}^2$
1	$\approx 6.0 \times 10^{-18}\,\mathrm{cm}^2$
2	$\approx 5.5 \times 10^{-18}\,\mathrm{cm}^2$
5	$\approx 5.2 \times 10^{-18}\,\mathrm{cm}^2$
6	$\approx 5.0 \times 10^{-18}\,\mathrm{cm}^2$
7	$\approx 4.5 \times 10^{-18}\,\mathrm{cm}^2$
8	$\approx 3.5 \times 10^{-18}\,\mathrm{cm}^2$
9	$\approx 3.2 \times 10^{-18}\,\mathrm{cm}^2$
10	$\approx 3.0 \times 10^{-18}\,\mathrm{cm}^2$
11	$\approx 2.8 \times 10^{-18}\,\mathrm{cm}^2$
12	$\approx 1.7 \times 10^{-18}\,\mathrm{cm}^2$
13	$\approx 2.3 \times 10^{-18}\,\mathrm{cm}^2$
14	$\approx 1.5 \times 10^{-18}\,\mathrm{cm}^2$

Tab. 2.4: Calculated cross sections for excitation of vibrational levels of H_2 molecules in electronic and vibrational ground state by 40 eV electron collisional excitation through the B and C states. Data by J. Hiskes taken from [4]. Hiskes believes the total cross section (i.e. including processes via higher electronic states than B and C) to be 25 % to 40 % higher. The sum of the cross sections for $\nu \geq 5$ yields $\approx 3 \times 10^{-17}\,\mathrm{cm}^2$.

than B and C states to be 25 % to 40 % of the one for B and C states. The processes start at a threshold energy of ≈20 eV and peak at 40 eV. Including the estimate for higher electronic states the cross section for the production of $\nu \geq 5$ states via the described process adds up to approximately $4.0 \times 10^{-17}\,\mathrm{cm}^2$ to $4.5 \times 10^{-17}\,\mathrm{cm}^2$. This is sufficiently large for the process to play a key role in H^- formation in negative ion sources. Note that the reaction requires electrons with kinetic energy E > 20 eV and can therefore only take place in the hot driver region of the source but not in the extraction region.

However, some effects to do with the plasma and extraction electrode can not be explained by this model of the excited molecules solely being produced in the hot

plasma region. Several researchers have therefore suggested that rovibrationally excited H_2 molecules are also produced through surface interactions on the wall, the plasma electrode and the collar of the extraction electrode [51, 56]). Evidence for this is seen in the fact that an extraction field protruding into the collar of the extraction electrode enhances the H^- yield. M. Bacal's hypothesis [51] is that rovibrationally excited H_2 molecules are produced by the interaction of atoms with the inner walls of the extraction collar. These interactions are supposed to lead to recombinative desorption of excited H_2. Due to the protruding positive fields the positive ion density in this region is lower and therefore reduces the destruction of H^- by mutual neutralisation with H^+. Experiments with conditioning of the collar surface through heating and positive ion bombardment have lead to increased H^- yields, this could be seen as a confirmation of the hypothesis.

Destruction of H^-

We have discussed the processes of H^- production. However there are a number of processes happening in ion source plasmas which lead to the destruction of H^- ions. It is important to know and understand them as well in order to minimise their effect and be able to extract as much as possible of the H^- produced in the ion source. According to [1, 55] the three main destruction processes that play a role in negative hydrogen ion sources are:

a) Mutual Neutralisation

$$H^- + H^+(\text{or } H_2^+ \text{ or } H_3^+) \quad \rightarrow \quad H^0 + H^0(\text{or } H_2 \text{ or } H_3) \tag{2.5}$$

b) Electron Detachment

$$H^- + e \quad \rightarrow \quad H^0 + 2e \tag{2.6}$$

c) Associative Detachment

$$H^- + H^0 \quad \rightarrow \quad H_2^* + e \tag{2.7}$$

The cross section for mutual neutralisation has its minimum value of $\approx 7 \times 10^{-15}\,\mathrm{cm}^2$ at a centre-of-mass energy of $\approx 20\,\mathrm{eV}$ [57]. At energies below 1 eV the cross section is an order of magnitude higher. It follows that it is beneficial to keep the positive hydrogen ions in the plasma at the highest possible temperature. Electron detachment has its threshold at 0.75 eV [58]. The cross section dramatically increases with energy, especially in the region of a few eV. The peak value at about 45 eV is several orders of magnitude larger than the threshold value and half of the peak value is already reached at about 8 eV. This illustrates the key role of the magnetic filter for the ion source in keeping electrons with more than 1 eV out of the extraction region. Associative Detachment plays a role as the Hydrogen atoms are neither susceptible to magnetic filter fields nor to electric fields created by electrodes and therefore the hardest to control.

As mentioned before, the H^- is produced from rovibrationally excited H_2^* molecules. These molecules are believed to be mainly produced in the hot region of the plasma. Of course they can be destroyed before any H^- is formed by them. This may either happen by their dissociation or ionisation, or by vibration-translation (V-T) transfer in an interaction with a hydrogen atom. M. Bacal [51] states that this is the reason for the existence of an optimum pressure in H^- volume production sources. From a certain pressure on the advantages of higher H_2 and electron densities, which would normally lead to higher H^- densities, will be outweighed by the increase in H_2^* destruction by vibration-translation transfer.

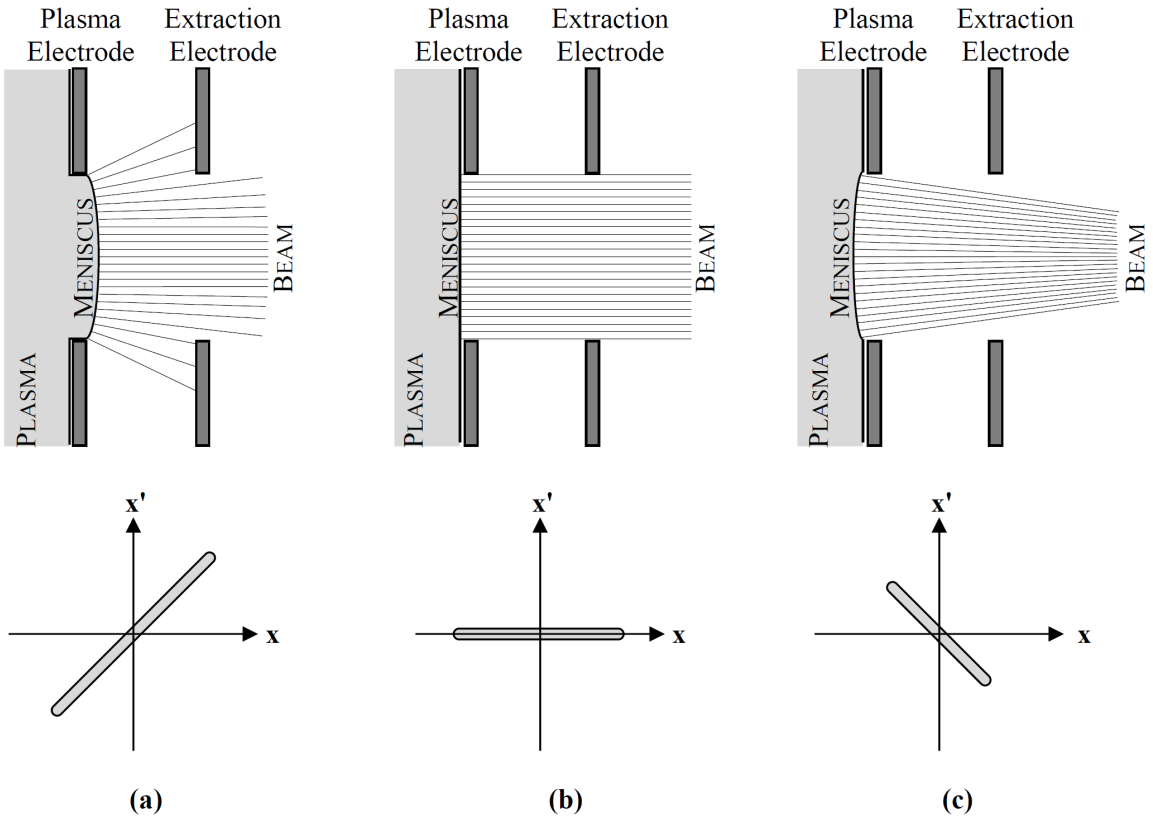

Fig. 2.10: Three different plasma meniscus shapes and their corresponding emittance phase space plots: (a) convex, high plasma density; (b) flat, medium plasma density; (c) concave, low plasma density. Schematic taken from [1] with the author's permission.

Transport Processes and Extraction

The H^- produced in the plasma of an ion source needs to be extracted in order to be accelerated in an accelerator. The extraction usually happens with two electrodes and a voltage between them. The first electrode, the so called plasma electrode is in contact with the plasma and has a (usually round) hole. This electrode has a potential similar to the potential of the plasma. The second electrode, called the extraction electrode, is parallel to the first, has a round hole as well and a (in our case of negative particles) positive voltage several hundreds or thousands of volts higher than the first one. The edge of the plasma in the hole of the first electrode is called the plasma meniscus. The shape of this plasma meniscus depends on the plasma density as well as on the extracting fields and can vary from convex for high plasma densities over flat

to concave for low plasma densities as illustrated in Figure 2.10. The meniscus shape has a strong influence on the divergence of the beam and therefore on the matching for beam transport in subsequent accelerator components.

The current density that can be extracted by a set of extraction electrodes with a certain extraction voltage has a physical limit set by space charge. Simply speaking this means that at the space charge limit the field created by the charge of the beam is so strong that it cancels out the extracting field. Even if surplus charge carriers (e.g. H^- or e) were present at the plasma boundary they would not be extracted. The maximum extractable current density j is given by the Child-Langmuir equation, here given in practical and very convenient units [1]:

$$j = 1.72 \cdot \frac{V^{\frac{3}{2}}}{d^2} \cdot \sqrt{\frac{q}{A}} \tag{2.8}$$

j: maximum extractable current density in $\mathrm{mA\,cm^{-2}}$
V: extraction voltage in kV
d: extraction gap width in cm
q: charge state of extracted beam particles (1 for electrons and H^-)
A: mass of extracted beam particles in atomic mass units

Theoretically an increase of the extraction voltage should only lead to an increase of extracted current if the extraction is space charge limited. Nevertheless in some ion sources voltage increase beyond the space charge limit has been observed to further increase H^- currents [59]. This is explained by the extraction field penetrating through the hole in the plasma electrode and extending into the actual plasma volume. This leads to an expansion of the emission surface into the plasma and may cause optics problems [55] as the meniscus becomes highly concave. However other effects that might increase the H^- current without causing bad optics have been speculated about.

These are either to do with enhanced drift of H^- or with enhanced $H_2^*(\nu \geq 5)$ surface production on the plasma electrode surface [60].

It his highly undesirable to extract electrons along with H^- ions and, apart from trying to produce the highest H^- density possible, there are two ways of dealing with extracted electrons. The first way is another magnetic filter field in front of the plasma electrode (see Figure 2.7). This does not prevent the extraction of electrons, but it deflects them and dumps them on the body of the extraction electrode. The second means is a positive bias voltage applied on the plasma electrode (see Figure 2.9). This bias voltage reduces the plasma sheath potential and makes absorption of electrons on the plasma electrode easier. Together with the magnetic field from the filter which can confine electrons to transverse motion [61], an eventual absorption by the plasma electrode becomes much more likely. Also this field might prevent electrons from more central regions of the plasma from replacing those absorbed by the plasma electrode [62]. This leads to a reduced electron density in the extraction region. In this way electron extraction can be reduced by 50 % and more. At the same time the reduced electron density may lead to an increase in H^- density [62] as the plasma naturally tends to be quasi-neutral.

A second effect of putting a positive bias on the plasma electrode is sometimes observed in volume production ion sources e.g. in the Camembert ion sources at Ecole Polytechnique or at the Berkeley ion sources [60]. This effect is an enhanced H^- current without changing any of the other ion source parameters. This was observed at an optimum bias voltage of 2.5 V. Generally the discharge region plasma and the extraction region plasma have different plasma potentials due to their different temperatures and particle densities. M. Bacal argues that this potential difference is a barrier to low energy charged particles drifting from the discharge region towards the extraction region.

Biasing the plasma electrode would counteract this potential wall and therefore enable or enhance the drift of H^- produced in the discharge area towards the extraction area. However the effect was e.g. not observed in the Culham ion sources.

The general hypothesis that H^- not directly produced in the extraction area could drift to the extraction area has been verified by A Ivanov Jr [63]. Ivanov measured the H^- ion velocities in the extraction region of the Camembert III ion source with a two laser photo detachment experiment. Ivanov found two distinct ion species, one with an energy of $\approx 0.1\,\mathrm{eV}$ and the other with an energy of $1\,\mathrm{eV}$ to $2\,\mathrm{eV}$. According to Ivanov's interpretation the cooler species originates from the extraction region of the source whereas the other species originates from different regions within the source which are at a higher plasma potential and therefore get energy when they drift to the extraction region.

2.8 Control System

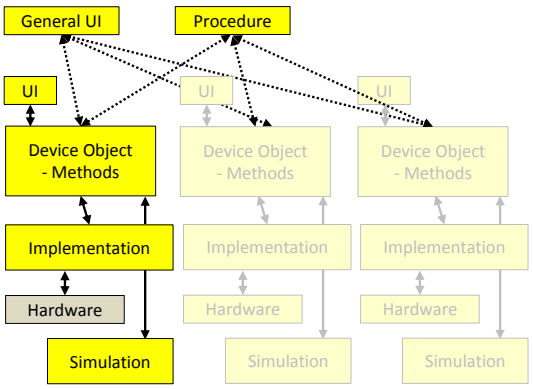

Fig. 2.11: Schematic of the control software architecture. UI means User Interface.

In order to control the whole experimental accelerator system and to be able to run experiments and take data, a control system has been developed using Object Orientated Programming (OOP) in the National Instruments LabVIEW programming environment. The software was developed by myself, using a OOP framework created

for similar experimental systems by our collaborators at the Siemens CT NTF HTC labs in Erlangen, Germany.

The framework provides a structure, where every hardware device is represented by an object with a certain set of methods which represent the actual physical hardware functions of the device. Optionally the object has a user interface (UI) to manually perform operations on the device and display or analyse data. The framework structure allows for the objects to use other objects of the system (see also Figure 2.11, e.g. a power supply object uses serial control objects to communicate), so that the whole hardware structure can be modelled in the software. This allows for high flexibility of the software system in terms of adding or removing hardware. The general framework handles all the objects including their optional user interfaces and therefore the physical hardware associated with them. It also provides the possibility to run applications, i.e. programmes which use the provided objects and perform certain tasks with the actual hardware. In fact this allows running of whole experiments including data acquisition and analysis automatically, always preserving the high flexibility of the system and making the addition of new hardware to the system straightforward. Furthermore any hardware device can be simulated by code which is very useful for the software development. Another option provided by the framework is the use of a simulation of the whole system, i.e. of a number of devices interacting with each other. This has proven very useful for the development and testing of the high voltage conditioning application (see Chapter 3.3). The software was first developed by setting all the device objects into a simulation mode, so that development and testing was safe without danger of damaging experimental equipment. The simulation mode is very realistic, as it creates a whole environment of simulated test system parameters. Any of these parameters can be manipulated to create system behaviour anomalies. The way the

software handles these anomalies can then be verified. Extensive testing within the simulation, trying out all eventualities, was performed and only after that the software was used with the actual hardware without the need for any further changes.

The given approach is very structured, versatile and flexible and allows for constantly adding new hardware to the system, as is the case in our experimental programme. Hardware devices can first be operated and tested singly (e.g. the ion source and the voltage multiplier) and then put together later on and operated jointly.

Devices that are similar to each other, e.g. the five power supplies of the ion source, are represented by different instances of the same object, only with a few different object settings. This reduces the required code and makes the implementation of multiple similar devices easy and quick. E.g. adding an additional power supply to the system can be done in 10 minutes, just by creating another settings file for the respective object.

In total I used three existing device classes and developed 14 new device classes including their implementations for our hardware. Using those device classes I configured approximately forty device instances (see Tables 2.5 and 2.6 for details). I furthermore wrote 5 different applications which can run different experiments using the device instances (see Table 2.7 for details). Many of the experiments discussed in Chapters 3 and 4 have been done using those applications, some of them running for hours on end without user interference.

The presented software system is ideal for the experimental purposes of the current system. For later developments of the accelerator which will be going towards a medical product, the software will have to consider patient and personnel safety. This may require a completely different approach, however the current software is meant to cover all experimental stages with many different hardware setup and is ideal for this task.

Device Class	Descriptoin of Device Class	Instances	Hardware Used by this Device Class	Classes Used
ADIO	Sets or Reads DC Analog and Digital Voltages	4	1x ADIO card or chassis	-
BeamProfile	Does Fits and Corrections on Beam Data from Wire Grid	2	1x Wire Grid	1x WireGrid
FaradayCupPT	Reads Faraday Cup Currents	2	1x PTC Precision Amperemeter F100	1x Serial
FibreThermo	Reads Temperatures from Fibre Thermometer	1	1x Neoptix Fibre Optic Thermometer Card (Including the Thermometer Fibres) in Dedicated Chassis	-
FlukeMultimeter	Configures Multimeter and Reads Measurements	1	1x Fluke Digital Multimeter	1x Serial
Huttinger	Supplies up to 20kW RF Power with Frequency Feedback	1	1x Huttinger RF Power Supply	1x Serial
ISGUI	Sets and Reads DC Output for Ion Source Power Supplies	1	5x Simple DC Power Supply	5x PowerSupplyStd
MassFlow	Sets and Reads Mass Flow Controller Values	2	1x Mass Flow Controller	1x Serial
PowerSupplyStd	Sets and Reads DC Power Supply Output	5	1x Simple DC Power Supply	1x ADIO

Tab. 2.5: Device classes in the control system (1 of 2). The first column states the name of the device class. the third column gives the number of instances of this class used in the control system (e.g. the ion source has 5 different power supplies, hence there are 5 instances of PowerSupplyStd, one for each power supply). Some device classes use instances of other device classes in order to carry out their tasks. The last column states which other classes are used by the device class described in the row, and how many instances of them are used.

Device Class	Descriptoin of Device Class	Instances	Hardware Used by this Device Class	Classes Used
PressureGauge	Reads Pressure from Gauge	6	1x Edwards Vacuum Gauge Controller, 1x Vacuum Gauge	1x Serial
Serial	Configures Serial Port and Sends and Receives Messages	9	1x Serial Port	-
ShuntRead	Reads DC Voltages across Shunt Resistors for Current Measurements on Ion Source Power Supplies	1	Shunt Resistors for Precise Current Measurements in Ion Source	1x ADIO
SignalGenerator	Sets and Reads Signal Generator Output	1	1x TTL Signal Generator	1x Serial
SparkSimulator	Sets System Values (Pressure, Temperature and Power Supply Status) in System Simulation	1	-	-
SysSim	Runs a System Simulation for Application Testing	1	-	-
TekScope	Configures and Reads from Oscilloscope	1	1x Tektronix Oscilloscope	-
WireGrid	Configures Electrometers and Reads Measurements from Wires	2	2x PTC 32-Channel Electrometer I3200, Wire Grid with Wires Connected to Electrometers	2x Serial

Tab. 2.6: Device classes in the control system (2 of 2). The first column states the name of the device class. the third column gives the number of instances of this class used in the control system (e.g. the vacuum system has 6 different gauges, hence there are 6 instances of PressureGauge, one for each gauge). Some device classes use instances of other device classes in order to carry out their tasks. The last column states which other classes are used by the device class described in the row, and how many instances of them are used.

Application Class	Description	Hardware Used	Device Classes
ISLogWhenPush	Logs all ion source data (including current and profile from Faraday Cup / wire grid) either when button is pushed or at a specified rate	Ion Source Faraday Cup Wire Grid	5x PowerSupplyStd 1x FlukeMultimeter 1x PressureGauge 1x MassFlow 1x BeamProfile
ISCharacter	Varies ion source parameters and logs data (including current from Faraday Cup) for each combination of ion source settings	Ion Source Faraday Cup	5x PowerSupplyStd 1x FlukeMultimeter 1x PressureGauge
HuttingerLogWhenPush	Logs all high voltage system data whenever button is pressed or at a specified rate	Huttinger RF Supply Transformer&Shells Oscilloscope Gauge Signal Generator	1x TekScope 1x Huttinger 1x PressureGauge 1x SignalGenerator
ShellConditioning	Carries out a careful conditioning of the shell system in vacuum	Huttinger RF Supply Transformer&Shells Oscilloscope Gauge	1x TekScope 1x Huttinger 1x PressureGauge
Conditioning_Thermo	Carries out a careful conditioning of the shell system in vacuum, using temperature as an additional system property	Huttinger RF Supply Transformer&Shells Oscilloscope Gauge Fibre Thermometer	1x TekScope 1x Huttinger 1x PressureGauge 1x FibreThermo

Tab. 2.7: Applications developed for the control system. The right column states which device class instances are required for the application.

3. GENERATION OF VERY HIGH ELECTROSTATIC FIELDS

3.1 Commissioning of AC Drive System

The transformer was designed and manufactured by Siemens CT NTF HTC in Erlangen, Germany. The primary side consists of four very thin silk insulated litz wire windings, the secondary of ≈200 windings of the same material, all of them together forming a toroid. The components of the transformer were then put together again by us at RAL.

Operation and Feedback System

The Hüttinger power supply (see Figure 2.5) in its normal use for induction heating is operated with an external parallel resonance tank circuit. A phase feedback signal from the tank circuit goes back into the power supply. It is used to adapt the output frequency and keep it always exactly on the resonance frequency of the oscillator circuit. The output waveform of the power supply is not an ideal sinewave. The voltage in the tank circuit however is a sine wave and thus suitable as a feedback signal. In our setup we are of course not using the external oscillator circuit that comes with the power supply, as we want to use the primary and secondary of the transformer as oscillator. We therefore had to adapt the feedback. For experiments we used a signal generator and connected it to the feedback input as a means of manually setting a frequency. We could then carefully adapt the frequency in order find the resonance point where the input current would be minimal (see Figure 3.4). This is a lengthy

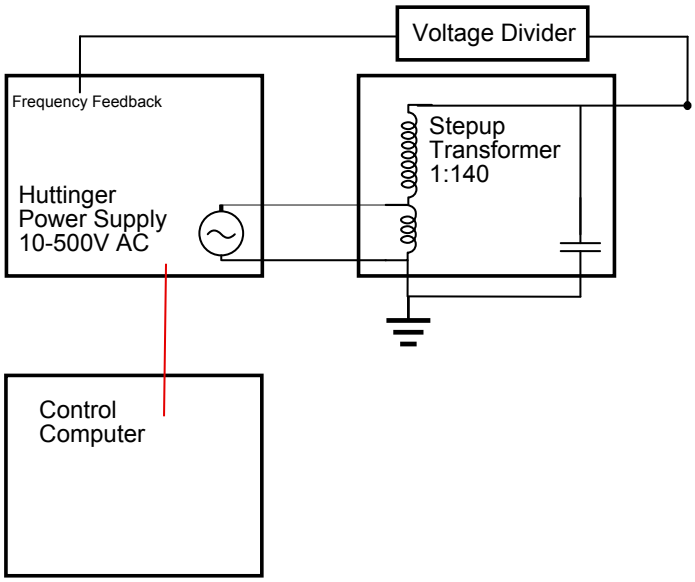

Fig. 3.1: A schematic of the setup of the phase feedback system. The signal is taken from the output side of the transformer. The voltage is reduced by a voltage divider. The signal is then connected to the phase feedback input of the power supply which uses the feedback to adapt its output frequency.

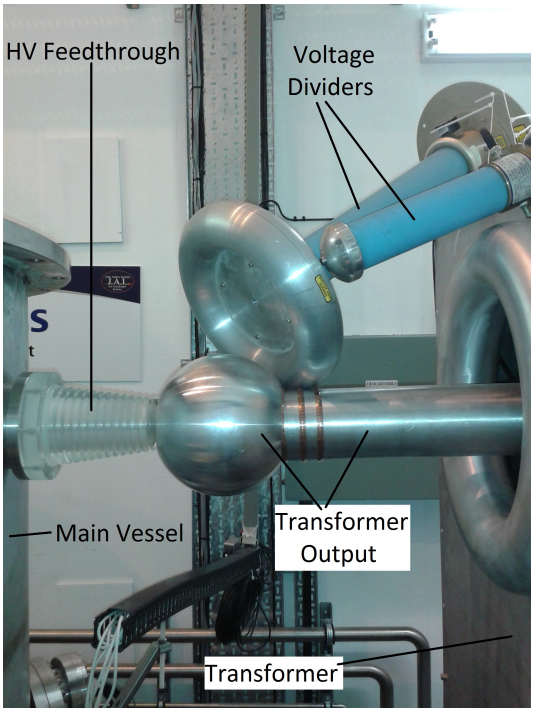

Fig. 3.2: The transformer output side (right) connecting to the AC high voltage feedthrough (left). The feedthrough leads the voltage into the main vessel which contains the shells. On top of the transformer output are two voltage dividers, one for voltage measurement, the other one for phase feedback to the power supply.

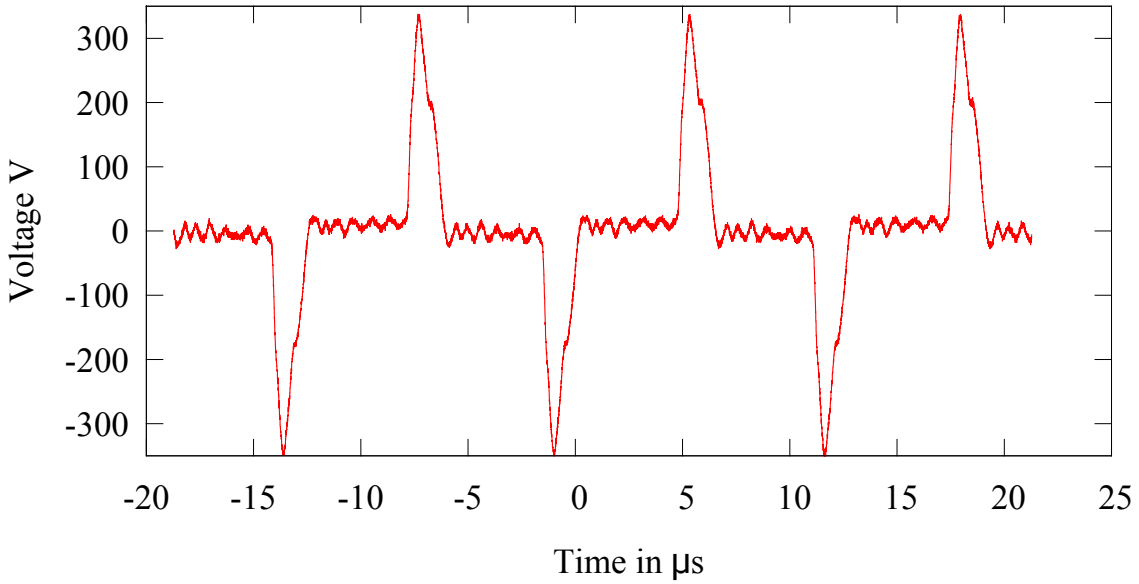

Fig. 3.3: The transformer input voltage waveform at 79.1 kHz, i.e. off resonance. The signal is not suitable as phase feedback for frequency control.

procedure and inconvenient to do frequently during other experiments. However the resonance frequency can slightly change with every change in temperature as well as with changes in stray capacitances caused by only slightly moving a piece of equipment. A genuine feedback system would therefore be better. We tried to take the feedback signal from the input side of the transformer. However the signal was rather noisy and far from being sinusoidal, especially when slightly deviating from resonance frequency (see Figure 3.3). We unsuccessfully tried a number of means to get a better signal, such as reading out the primary current with a current probe or filtering the primary voltage with a two stage low pass filter. We then tried taking the perfectly sinusoidal output voltage on the secondary side as feedback signal, which worked well. For that purpose we attached a 1:1000 voltage divider to the transformer output (see Figure 3.2) which we then connected to the feedback input on the power supply (see Figure 3.1 for schematic). This setup worked well and possible phase shifts between primary and secondary voltage did not present a problem. A second voltage divider is used for voltage measurement with the oscilloscope. Of course the capacitances of the voltage

dividers slightly change the resonance frequency.

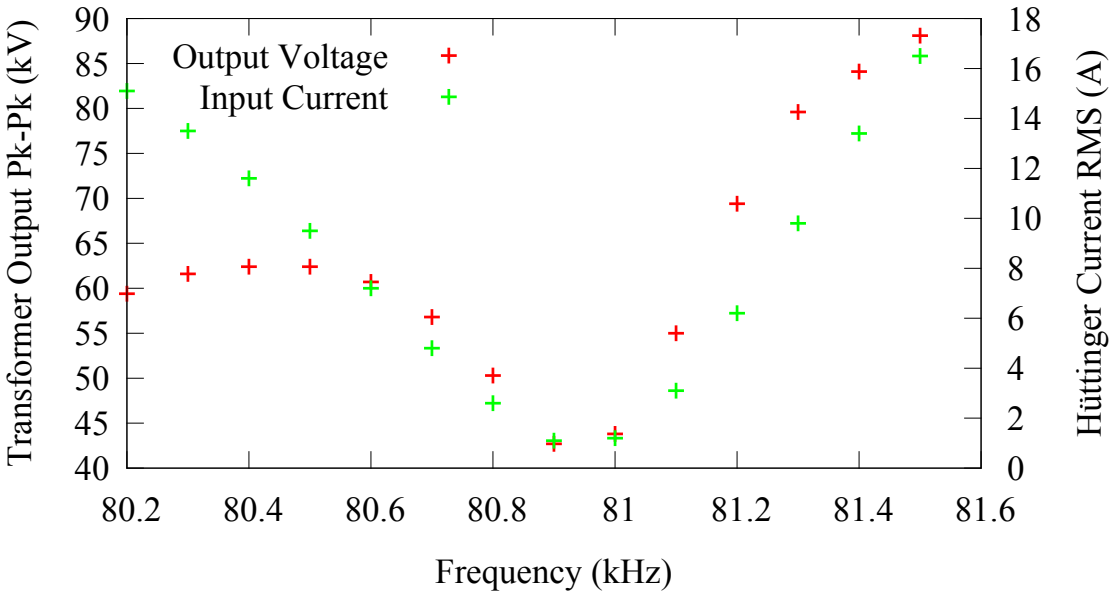

Fig. 3.4: Frequency response of the AC drive system at a drive voltage of ≈300 V peak to peak.

Frequency Response

The frequency response of the transformer was examined with a careful frequency scan using the setup with a signal generator as explained above. The resonance frequency was determined to be ≈80.9 kHz. The exact frequency depends on stray capacitances and of course e.g. the capacitances of voltage dividers. Figure 3.4 shows that both current and voltage increase dramatically below and above the resonance frequency. This is in accordance with the behaviour expected from the simulations in Section 2.4.

Transformer Ratio and Currents

The transformer ratio at resonance was determined to be approximately 137.5:1 (see Figure 3.5) which is only slightly above the simulated value of 125 (see Section 2.4). The input current at 800 V is about 3.2 A which is a bit more than the simulated value of 2.2 A.

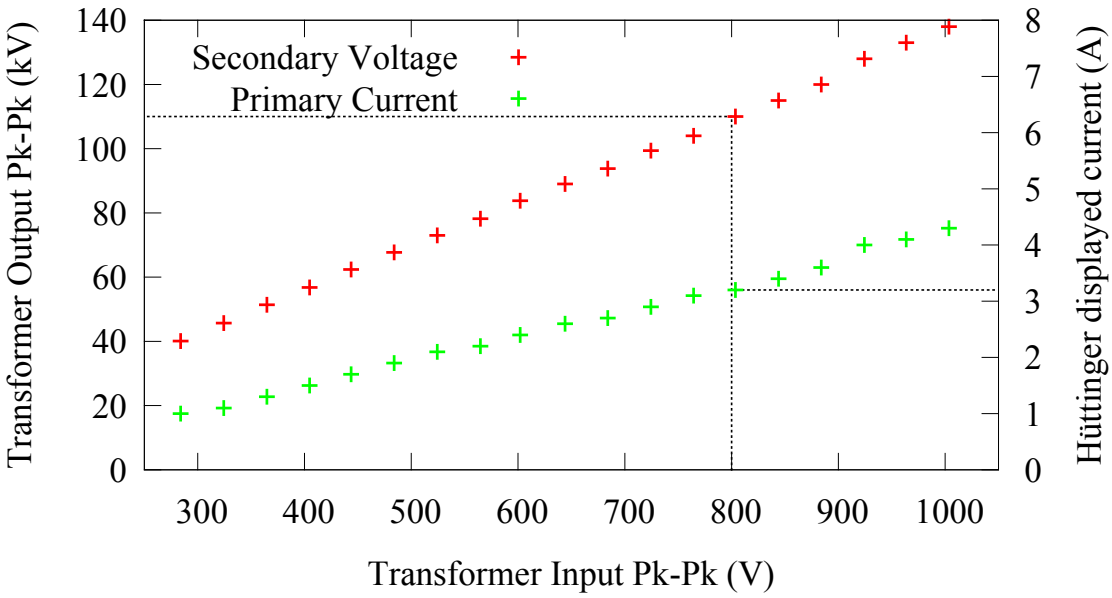

Fig. 3.5: Transformer secondary side voltage and primary side input current versus primary side voltage. The values are in reasonable agreement with the numbers expected from simulations (see Section 2.4).

Maximum Output Voltage

We did a number of tests to determine the maximum output voltage that could be provided by the AC drive system. The limiting factors are breakdowns on the internal shunt capacitor of the transformer as well as breakdowns between the toroidal inductance and the aluminium body of the transformer housing and between the voltage output rod and the grounded housing These would start at output voltages of about 140 kV peak to peak. Given the fact that the whole experiment is situated in a concrete bunker it is very hard to accurately diagnose where the breakdowns happen. We placed cameras inside the transformer and recorded during transformer operation in order to determine where breakdowns happened. However, due to the low sample rate of the camera, it was still hard to accurately locate and diagnose breakdowns. The maximum peak to peak voltage achieved in our various test series was 175 kV.

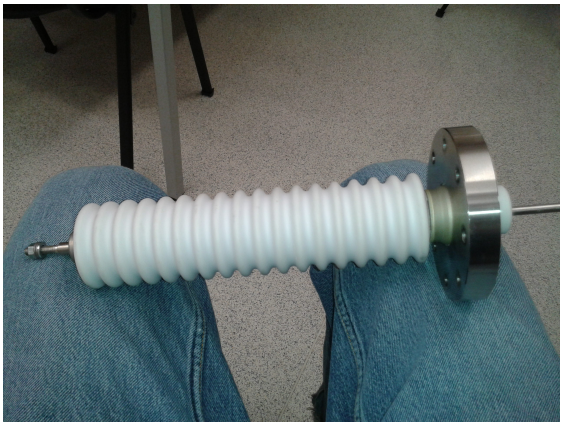

(a) off-the-shelf

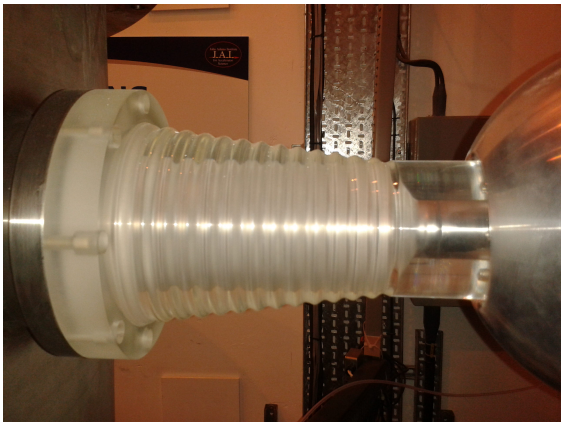

(b) bespoke

Fig. 3.6: An off-the-shelf ceramic feedthrough and our bespoke AC feedthrough.

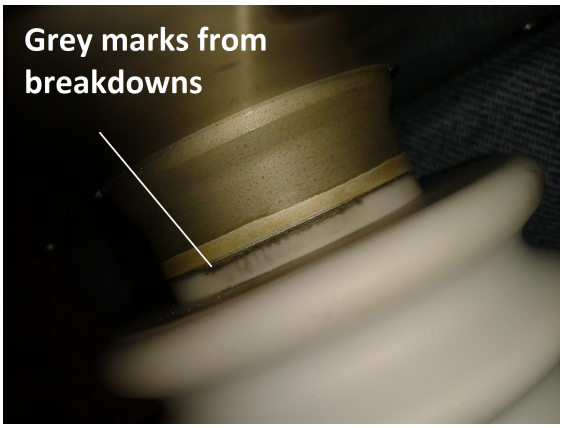

(a) marks from breakdown

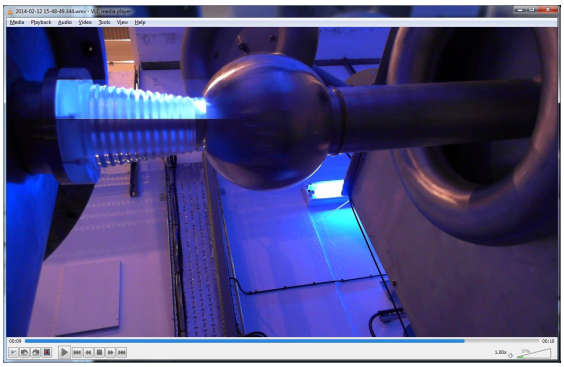

(b) bespoke feedthrough lighting up during breakdown

Fig. 3.7: The ceramic feedthrough had severe marks and damage from breakdowns both on the air side (picture) and on the vacuum side. The breakdowns on our new feedthrough started at 140 kV. However these breakdowns did not leave any damage.

High Voltage Vacuum Feedthrough for AC

The high voltage feedthrough which we initially used to guide the drive voltage into the vacuum vessel was an off-the-shelf ceramic DC high voltage feedthrough rated at 150 kV (see Figure 3.6a). However due to the high dielectric loss angle of the ceramic material the feedthrough severly heated up during operation. Also it happened to break down both on the vacuum side and on the air side (Figure 3.7a). Our team therefore designed a bespoke feedthrough. It has a different geometry to lower the fields near the central conductor and is using Rexolite rather than ceramic as insulator

material. Rexolite has a very low dielectric loss angle and is therefore ideal for AC purposes. The new feedthrough was successfully tested both in AC and DC operation. In DC operation it was able to withstand voltages of up to 130 kV without breakdown, in AC operation first breakdowns (see Figure 3.7b) started at about 140 kV peak to peak. Conditioning could possibly increase this number, however it was not undertaken as the maximum required voltage for our system is 100 kV. During high voltage AC operation of the feedthrough at 150 kV no temperature increase of the insulator was detected.

3.2 High Voltage Testing of Shells and Insulators

A number of experiments have been performed to test the voltage holding capability of the shells and the inter shell insulators, these tests included both testing with AC voltages and testing with DC voltages.

AC Tests These test consisted basically in applying an AC voltage to a system of shells and diodes as they would be used in the actual accelerator setup. This AC voltage would then be increased slowly, usually over a conditioning process of several hours, and the effects on the system would be monitored and observed. Obviously these tests would inevitably test the diode chains at the same time and were considerably limited by diode failure rather than insulator failure (see also Section 3.5 for details of the diode testing). We tested a number of different insulator designs. We encountered various problems with an off-the-shelf high voltage feedthrough, which led us to designing our own high voltage feedthrough (see Section 3.1). For a schematic of the setup see Figure 3.18.

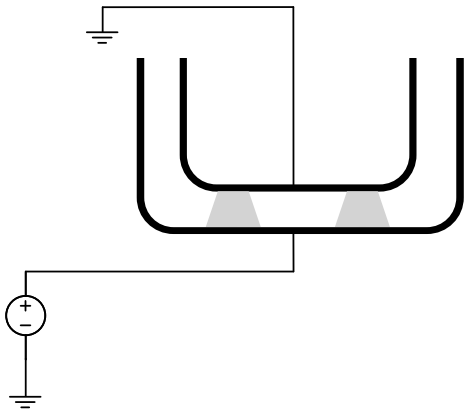

Fig. 3.8: Schematic of the setup for the DC insulator tests.

DC Tests For the DC insulator tests we used a 120 kV DC power supply which would sit outside the vacuum and connect into the vacuum chamber through our high voltage feedthrough. We would then place the insulators between two shells, one of which would sit on grounded rods and therefore be at ground potential, the other one would be connected to the feedthrough (see Figure 3.8 for schematic). For these tests again we would increase the voltage slowly over a prolonged conditioning process. One of the advantages of the DC test is that it is rather easy to monitor the currents of breakdowns and discharges as they can be read from the power supply. This gives a good indication for analysing the voltage holding capability of the insulators.

Test Results of Various Insulator Designs

Threaded Insulators The first insulator tests were done with PEEK insulators which were connected to the shells with screws. The insulators were 10 mm high and had metallic rings for stress reduction. The insulators had threaded holes and were connected to the shells with PEEK screws. During our tests these insulators repeatedly failed during the AC test at an input voltage of 28 kV, see Figure 3.9. The combination of thread, screw and vacuum proved very unfortunate.

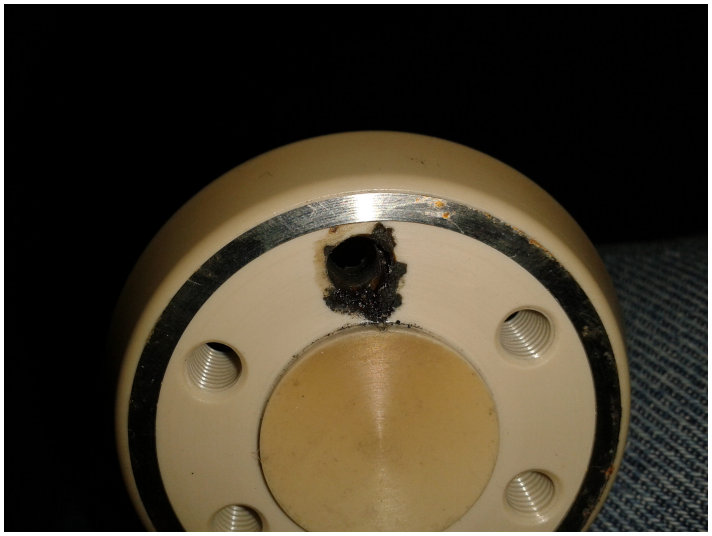

Fig. 3.9: Failure of the insulator with threads. A carbonised path formed through one of the threads.

Threaded Insulators with longer Screws In a subsequent test we used longer screws as field simulations had shown that this would reduce the fields in some areas inside the threads. This approach was partly successful as the insulators were now capable of holding somewhat higher voltages, i.e. about 40 kV. At this point they would fail the same way, i.e. forming a carbonised path through one of the threads. 40 kV is still far below the design goal of 100 kV and therefore the threaded design with PEEK screws was abandoned.

Fig. 3.10: Failure of an insulator. The failure happend at an input voltage of 60 kV Peak to Peak, i.e. a voltage of about 55 kV across the insulator.

Screwless Insulators We subsequently tested the same insulators only without the threadholes. This greatly improved their capabilities, we only once had a severe insu-

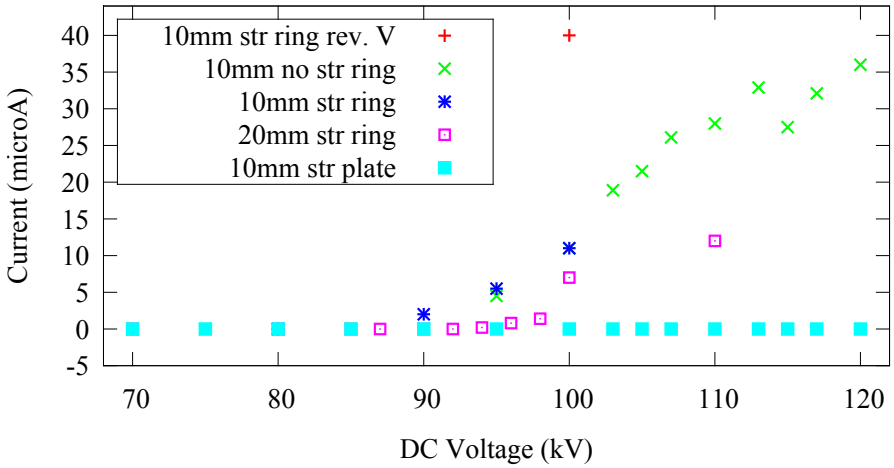

Fig. 3.11: Results of insulator tests using the setup from Figure 3.8. The graph shows the current across the insulator depending on the applied DC voltage. Ideally the current should be zero. The 20mm one has only slightly better performance than the 10mm ones. The stress ring does not seem to make any difference in this experiment, probably due to not very good contact between shell and stress ring. The polarity of the voltage however does make a difference, as expected from the results of other researchers as well as from theory (see Section 2.6 for theory on insulators). The insulator with the stress plate is capable of holding 120 kV and is by far the best design.

lator failure. This failure was most likely due to a defect in that particular insulator (see Figure 3.10). Throughout the entire test series no similar events were observed . In the DC test this insulator type started failing at about 90 kV with currents in the µA range going across it (see Figure 3.11). The damage to the actual insulator surface was not as severe as with other failures (see Figure 3.14), but there was also damage to the shell itself in the form of small pits (see Figure 3.12). As expected from theory (see Section 2.6) the marks are all near the triple point between insulator material, stainless steel shell and vacuum, as the breakdowns are initiated in that region. However, as the stress rings are supposed to relieve fields in that region, it is questionable whether the stress rings worked properly. Probably the contact between the shell and the stress ring was not sufficiently good in this design.

Subsequently another insulator design very similar to this one was tested, the dif-

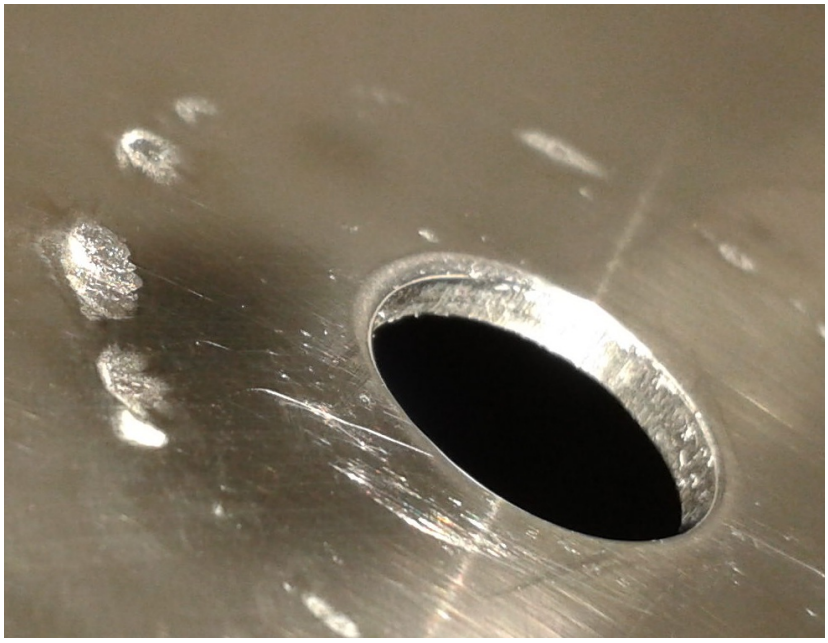

Fig. 3.12: Pits in shells after multiple breakdown over insulator. The pits are exactly at the location of the triple point between insulator, vacuum and stainless steel shell (insulator not present in this photo).

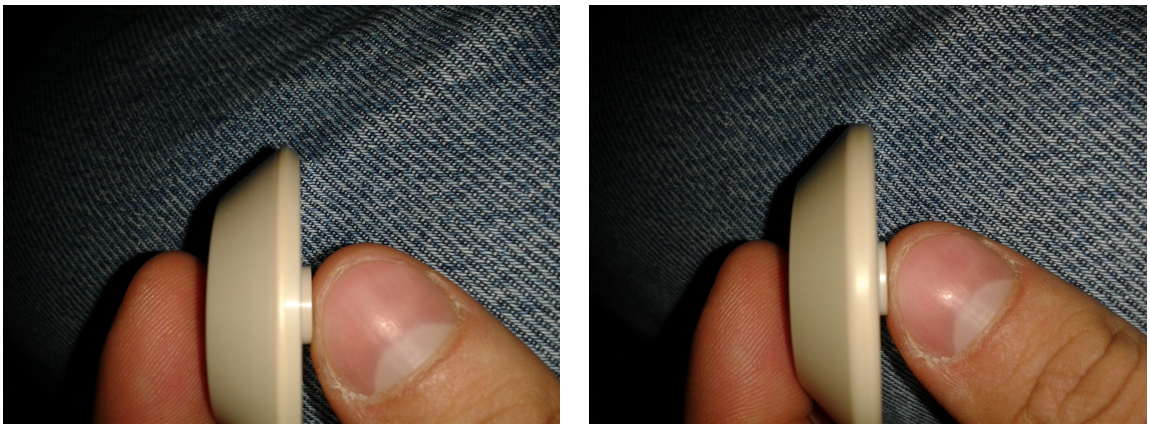

(a) sharp edge *(b)* round edge

Fig. 3.13: The two different flank designs tested on the 10 mm threadless insulators.

ference only consisting in the different geometry of the flank of the insulator, i.e. a sharper edge on the flank (see Figure 3.13 for flank designs). This insulator was tested with and without the metallic stress rings. The version without stress rings started letting current through at 90 kV and showed a similar pattern to the other version (see Figure 3.11). Neither the stress ring nor the flank profile seem to have a major influence on the voltage holding capability of the insulator.

Fig. 3.14: Small traces of carbonisation on insulator surface after high voltage testing of the insulator. The carbonisation happened near the triple point (see also theory in Section 2.6), however this happened to insulators with metallic stress ring as well as to those without. The reason for this is most likely insufficient contact between shell and stress ring.

20 mm *Insulators* In order to explore the voltage capability we used 20 mm high insulators, with their basic geometry looking like two of the 10 mm insulators stacked on top of each other. First breakdown events started at $\approx 95\,\mathrm{kV}$, however the currents were much lower than with the 10 mm insulators. After the tests the insulators only had tiny marks near the triple point, much weaker than the ones on the 10 mm insulators.

Central Tripod The threadless insulators showed good voltage performance, however there is a crucial disadvantage to them. The top set of shells cannot be held together by them and a different means of supporting those shells had to be found. We constructed a PEEK tripod which would sit inside the innermost bottom shell (as in Figure 3.18 on the right hand side). The innermost top shell would then sit on top of this tripod and the other shells would sit on top of it. When we started AC tests in this configuration it turned out that the tripod is prone to breakdowns across it, although the fields are much

lower than across the inter shell insulators. These breakdowns tend to develop into substantial surface glows which are sustained over several seconds. With the 2/3 shell system we were able to reach voltages of up to 90 kV despite those frequent breakdowns, however it turned out that the behaviour deteriorates in a system with more shells. When we tested the tripod with 7 shells heavy breakdowns started at input voltages as low as 20 kV. The most likely cause are secondary electrons from outer shells getting accelerated and hitting the tripod (see Figure 3.15). We unsuccessfully tried a number of means to mitigate this problem, these included the use of ceramic rods rather than PEEK rods and metal screws rather than PEEK screws, as we had damage on the PEEK components (see Figure 3.16). We also unsuccessfully tried different means of shielding the tripod from secondary electrons. These included kapton shields around the tripod and/or around the outermost shells as well as a cardboard shield and an aluminium shield. However none of these means proved successful and they introduced new problems such as reduced pumping between the shells. We therefore abandoned this approach and developed a new inter shell insulator type that could hold the top shell set.

Insulators with Stress Plate Supporting the Shells We developed an insulator which has a stress plate instead of a ring (see Figure 3.17). A thread in the centre of the stress plate creates the capability of being screwed onto a shell. This design avoids the problem of threads in the PEEK as well as the problem of needing a central insulator to hold the top shell set. The insulator design has been tested very successfully. The benefit of tightly screwing it to the shells is good contact between the stress plate and the shell and therefore effective field relief around the triple point area. As the pits in Figure 3.12 show this didn't work well with previous designs. No such pits have been observed with this new design. In a DC high voltage test the design was able to

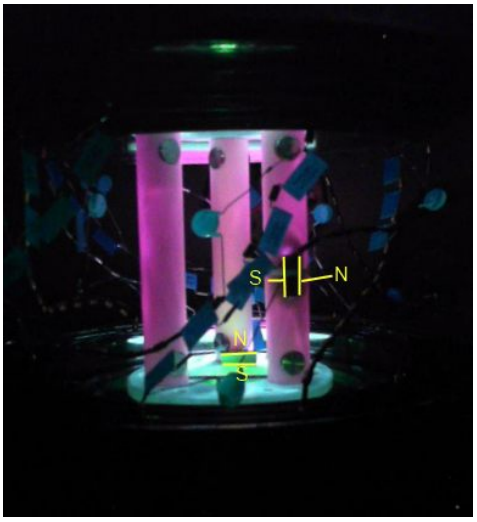

Fig. 3.15: The central tripod (with ceramic rods) breaking down in a sort of glow discharge at an input voltage of 20 kV (corresponding to a total centre voltage of app. 100 kV). Two permanent magnets with a strength of 400 mT have been mounted in two locations to see whether the glow pattern gets distorted by them, which is the case. This supports the hypothesis of the glow discharge being caused by secondary electrons

Fig. 3.16: The top of a PEEK screw from the central tripod assembly, which was destroyed during an experiment.

withstand our maximum test voltage of 120 kV (see Figure 3.11). First conditioning breakdowns started at about 85 kV, but after some conditioning the insulators were capable of permanently holding 120 kV without any permanent currents and thus outperforming all other designs, even the 20 mm one. This design will be used for our prototype accelerator as it meets the requirement of 100 kV per shell.

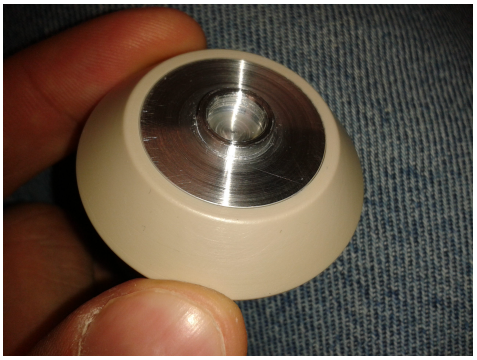

Fig. 3.17: Insulator with stress plate. The stress plate also carries a thread for a screw to tighten the insulator to the shell and therefore enabling a system setup with hanging shells and without tripod insulator. The screws also help to make better contact between stress plate and shell, thus making a crucial difference for the efficiency of the field relief design near the triple point. This design has proven the most successful one in DC high voltage tests (see Figure 3.11).

3.3 A High Voltage Automatic Conditioning Software

The creation of high electrostatic voltages usually involves a lot of the so called conditioning. This is due to dirt and imperfections on the surfaces of the electrodes between which the electrostatic fields are created. Those dirty regions and imperfections cause the voltage to break down, however during the process of breakdown the dirt gets partly or completely destroyed and subsequently the system is able to reach a higher voltage without breakdown than before. These processes are rather complex and some detailed investigations into the nature of these breakdowns have been made by other researchers (e.g. see [64], [38], [65], [66], [39] and [67]). The insulators inbetween the shells take part in the conditioning process as well. They have surface imperfections and trapped gas volumes which need to be conditioned away. E.g. in [48] the initial voltage standoff was only slightly above 50 % of the value achieved after extensive conditioning.

However in our experiments the breakdowns during conditioning do not only have beneficial effects. The released energy can damage the diodes of the Cockcroft Walton circuit and the insulators between the metallic shells as well as the metallic surfaces

themselves. The conditioning of the insulators is particularly delicate as they are very prone to surface damage. If breakdowns happen too frequently or even sustained discharges are developed then this may actually even decrease the voltage holding capability of the system. This effect is called deconditioning. In order to have a positive effect without the negative outcome of deconditioning the conditioning process needs to be done very carefully. This means limiting the number of discharges per unit time as well as the duration and intensity of single discharges. All prolonged discharges are to be avoided and discharges should be stopped as soon as they have started. This can be done by decreasing the input voltage whenever a discharge starts. After some time when produced gas and ion clouds have had time to be pumped away, the voltage can be increased again. This procedure can take many hours, for this reason it is desirable to automate this process. The following sections describe a software which I have developed for the conditioning of our various prototype test setups at the Rutherford Appleton Laboratory.

Setup Figure 3.18 shows a schematic of the hardware setup for the conditioning. The used test system consists of the Huttinger Power Supply which is used to drive the resonant transformer (see Sections 2.4 and 3.1) using feedback from the transformer output side. A separate voltage divider on the output side of the transformer is connected to a digital oscilloscope which uses one of its measurement functions to measure the amplitude (or rather the Peak to Peak value) of the sinusoidal output voltage of the transformer. The control computer reads this measurement from the oscilloscope. The transformer output voltage is also connected to the inside of a large vacuum vessel via a high voltage feedthrough with AC capability, which was designed and commissioned by our group (see Section 3.1). Inside the vacuum is usually a test setup consisting of various metallic shells interconnected by diodes and spaced apart by insulators. The

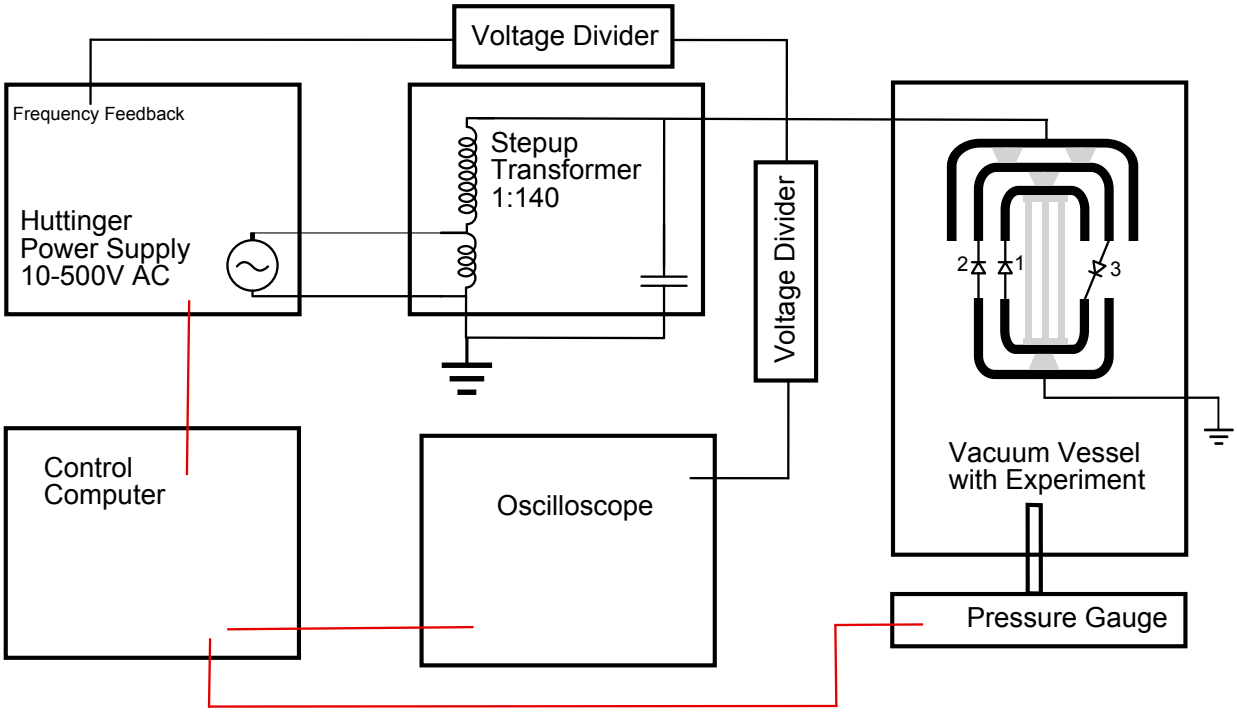

Fig. 3.18: Schematic of the physical setup for the conditioning with the conditioning software. The computer controls the Huttinger Power Supply and reads feedback from that same power supply as well as from the pressure gauge and the voltage divider.

pressure inside the vacuum vessel is monitored by a pressure gauge which is also wired into the control system.

Software Working Principle As described in Section 2.8 the control system architecture which I used for the overall control system allows for the implementation of software applications which can use any of the physical or virtual devices which are represented by LabVIEW OOP classes and use all their methods. Exploiting this, I developed a software application which gradually increases the Huttinger Power Supply voltage and thus the transformer output voltage which is the input voltage to the Cockcroft Walton test system inside the vacuum vessel. The value of the vacuum pressure is used as a feedback to detect breakdown, as every breakdown event creates some sort of gas or ion cloud and therefore increases the pressure. As soon as a breakdown is detected, the input voltage is decreased and kept constant at a lower voltage for some time. After a while the software starts increasing the voltage again. The software also

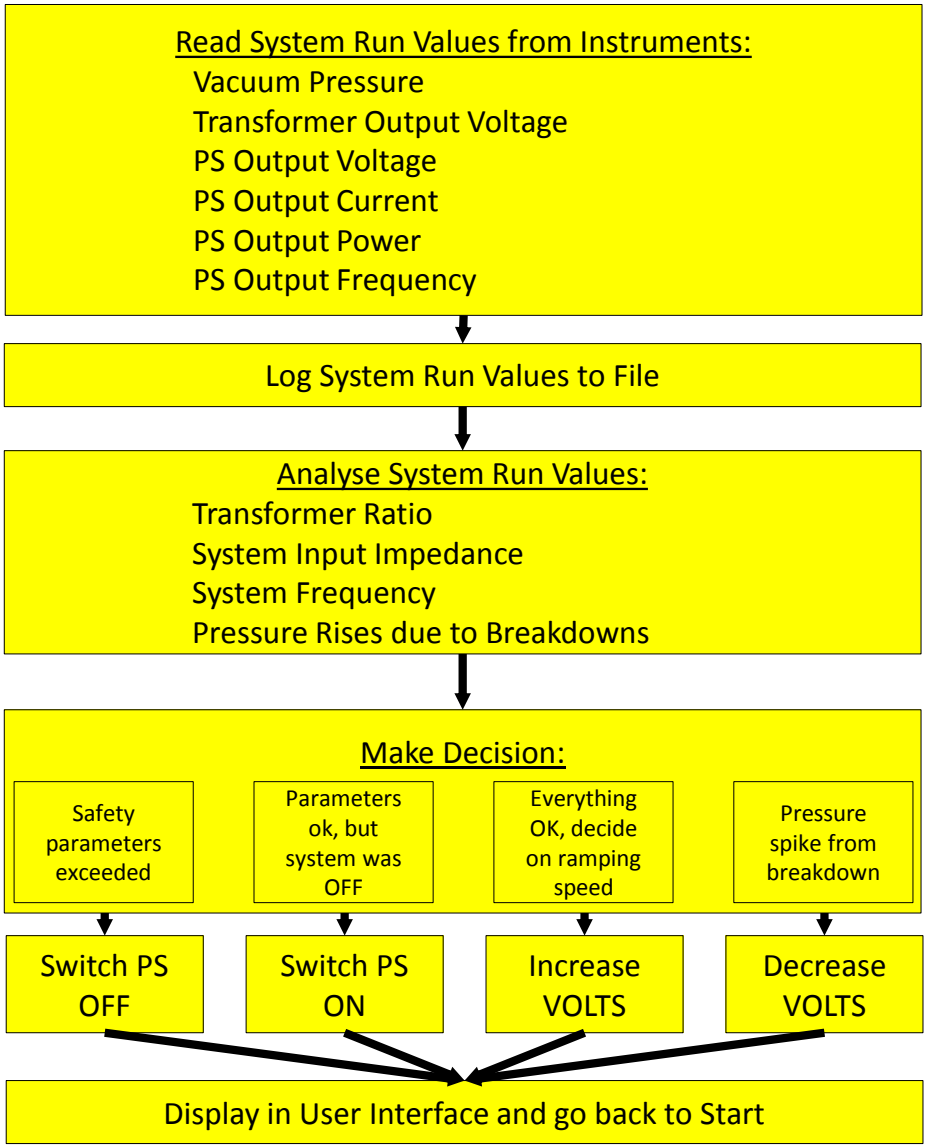

Fig. 3.19: Simplified flow diagram of the conditioning software, showing the main steps of each iteration during the experiment. The data acquisition takes 60 ms to 80 ms. The application can run at 10 Hz, but it can also be slowed down on purpose.

monitors the parameters of the Huttinger Power Supply and the output voltage of the transformer and performs a number of system checks to make sure that everything is running correctly. If any of the monitored values crosses a certain threshold the software stops the experiment. See Figure 3.19 for a flow diagram of the software.

Ramping up the voltage The higher the voltage gets, the more slowly does it need to be increased. Therefore the software has three different speeds of increasing the voltage. The first one is after switching on the power supply and gets the voltage back

up near to the threshold where breakdowns occur. Gradients of up to a few $\mathrm{kV\,s^{-1}}$ are reasonable for this stage. This rather high ramping speed saves time. A conditioning process often involves the safety switch of the power supply to switch the power supply off. After each safety switch-off the software needs to restart the power supply and ramp the voltage again. The second ramping speed is used for the last few kV before the currently achieved breakdown threshold is reached. It is also used to go back to the breakdown threshold when the voltage was reduced as reaction to a breakdown. For this ramping phase a few hundred $\mathrm{V\,s^{-1}}$ up to $1\,\mathrm{kV\,s^{-1}}$ are viable. The third phase is slowly increasing the voltage at the current breakdown threshold. Here low gradients of $50\,\mathrm{V\,s^{-1}}$ and below are appropriate.

Detecting Breakdowns For fast breakdown detection it is important for the software to react even to small pressure increases. The system pressure naturally oscillates slowly over time and normal operation of the system can increase the pressure as well, this too usually happens rather slowly. The system therefore calculates a base pressure and then immediately reacts if this pressure is exceeded by a certain value. From experience with our experiment it is reasonable to set the threshold at 2×10^{-8} to 5×10^{-8} mbar above base pressure. The base pressure is usually of the order of 3×10^{-7} mbar. The base pressure value is calculated from a histogramme of the last 100 measured pressure values with a channel width of 1×10^{-8} mbar for the histogramme. The highest value histogramme channel containing more than 30 % of the measured pressure values is taken to calculate the base pressure. The mean of all values in that channel is used as the base pressure value. This technique ensures that quickly rising pressure values do not effect the base pressure calculation.

Reaction to Breakdown and Safety Switch-Off Whenever a breakdown occurs and the pressure exceeds the threshold the software immediately decreases the input voltage by about 5 kV and then waits for the pressure to come down below the threshold again. If it does not get there within a few seconds, the software decreases the voltage by another step of 5 kV. After the pressure has come below the threshold again, the software waits another few seconds and then slowly increases it at intermediate ramping rate up to the voltage where the breakdown occured. Then it goes back to slow ramping rate. If the power supply is switched off either by the software itself or by its internal safety switches, the software waits for the system pressure to come below the threshold and then switches the power supply on at a rather low voltage. After that it ramps the voltage up to about 5 kV below the breakdown threshold at fast ramping rate. From there it continues ramping at an intermediate rate until the voltage is reached where the switch-off happened.

Safety Checks During operation the software constantly monitors the transformer ratio, the system input impedance, the resonance frequency, the power supply output current and the system pressure. If any of these values are outside the limits specified for them, the software immediately switches the power supply off. After that it will restart it, however for safety reasons it will only do a limited number of restarts before it stops the experiment completely. Events where this happened during our experimental trials include carbonised components as well as a loose connection on the transformer resonance feedback and the safety checks and problem handling system of the software have proven successful and very beneficial.

User Interface and User Interference The software logs all the measured data to a file but it also displays it in a graphical user interface (GUI), so that operators can

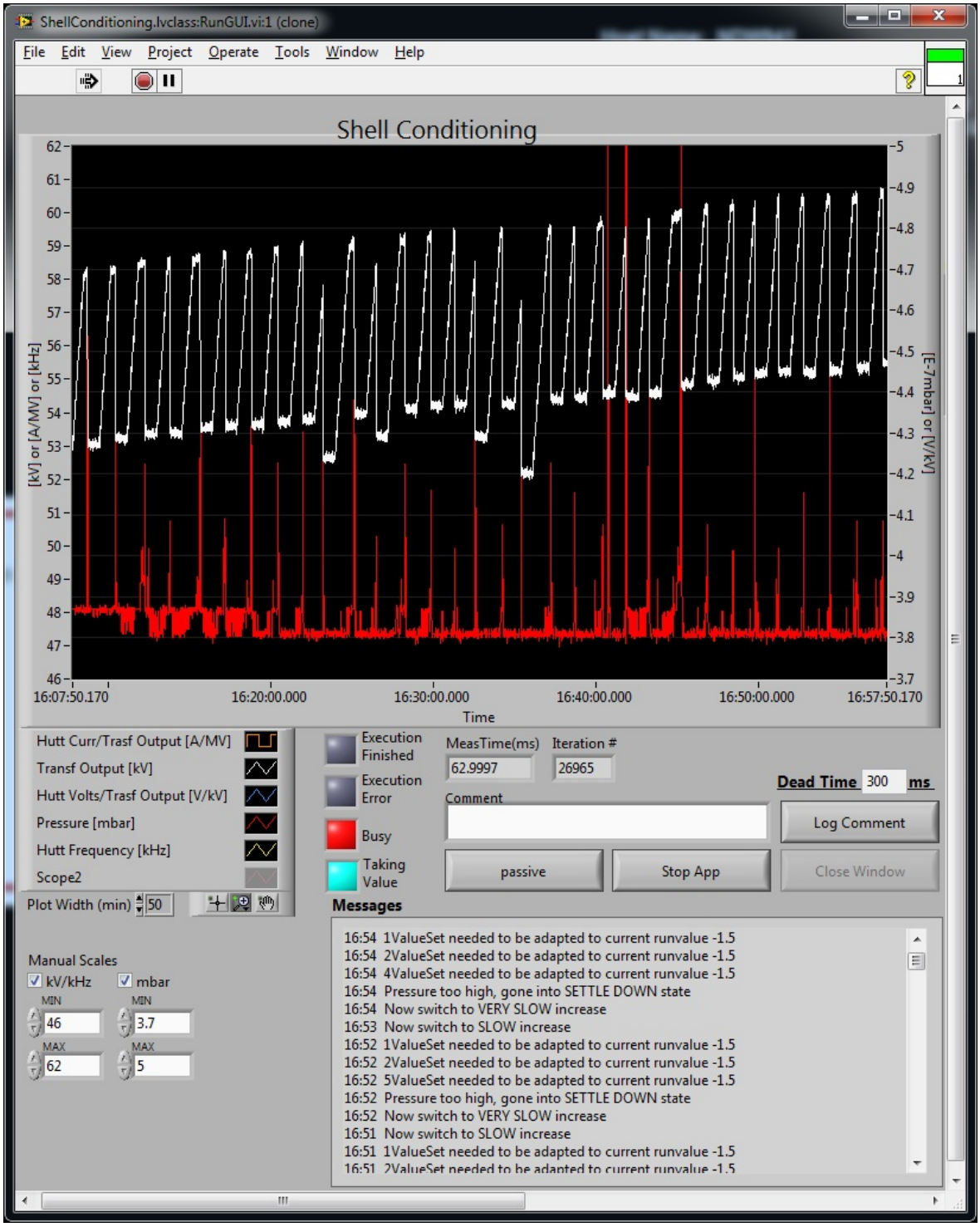

Fig. 3.20: A screenshot of the GUI. The red trace displays the system pressure and the white trace the transformer output voltage. Whenever a breakdown occured (red trace spikes) the software immediately decreased the voltage by 5 kV to stop the breakdown and subsequently increased it again. The displayed conditioning run increased the breakdown threshold by about 3 kV over the course of 50 min. This illustrates that conditioning can take many hours.

watch and supervise the process if they wish to. All operating parameters of the software (like pressure thresholds, safety limits, ramping speeds etc.) can be changed online in this GUI, which enables the user to optimise the process during operation and to tailor it to the current test setup inside the vacuum vessel. The user can also separately open the user interface of the Huttinger power supply and manually set voltages. For this purpose the software can be deactivated with the 'passive' button. It will continue logging and displaying values but will not take any action. It is also possible to manually set values while the software is actively running. To enable this the software always checks the present output voltage before it sets a new voltage. It always does the increase steps from the last voltage measured. This has proven very beneficial, the user can manually increase or decrease the voltage when desired, but longer phases of ramping can be done smoothly by the software and the spark detection is always active and will immediately decrease the voltage in case of breakdown. The reaction time of the software to sparks is in the order of hundred ms and therefore much faster than an operator. From experience with experiments it seems that a reaction time below 500 ms is sufficiently fast. Figure 3.20 shows the user interface with data from an actual conditioning process carried out in our lab.

3.4 Diodes and Circuit Protection

Breakdowns in the novel electrostatic accelerator

The novel accelerator is striving to push the limit of DC field gradients for particle acceleration. Electrical breakdowns during conditioning as well as operation are therefore inevitable. Due to the geometry of the machine these breakdowns are most likely to happen either between adjacent shells or between the most inner shells of the top and bottom shell set. It has indeed been observed in our experiments that sparks between

adjacent shells occur frequently, especially near or across the inter shell insulators (see Section 2.6 for theory and Section 3.2 for experiments). Breakdowns between the top and bottom shell sets have been observed too, however only in the setup with the inter hemisphere insulator which has been abandoned for that reason (see Section 3.2).

Breakdowns between adjacent shells happen in the AC column as well as in the DC column, both have been observed experimentally. During normal operation the electric fields in the gaps on both the AC and the DC side are constant, as the capacitors are charged up during the startup of the machine and do not usually change their charge substantially during operation.

Breakdown between adjacent shells leads to a current that flows through an inductive plasma channel and discharges the capacitive gap in question. The timescale of this discharge depends on the formation time of the plasma channel as well as its inductance and the amount of stored charge to flow through it. In a recent copper electrodes breakdown study at CERN A. Descoeudres et al. measured currents of about 100 A during their breakdown events [68]. The breakdowns would take about 1 µs to develop and current would flow for about 2 µs. However they discharged a capacitance of 27 nF, which is two orders of magnitude higher than the capacitances involved in our system. Breakdown events in our system are therefore expected to last for much shorter times.

The discharge itself might do damage to the surface of the two shells and of the inter shell insulators, however it does not affect any of the other components as long as no other currents flow. However, the decrease of the potential of all shells between this gap and the terminal leads to a discharge of the capacitors on the other column via the diode chains, if those shells are at higher potential than those they are connected to via the diodes. Of course this depends on the phase of the AC drive voltage at the

particular moment in time when the discharge happens. If the breakdown happens on the AC side, the worst case is the drive voltage being at its negative amplitude and if the breakdown happens on the DC side, the worst case is the drive voltage being at its positive amplitude. In both cases the shell breaking down will be connected through a diode chain to a shell on the other stack which has exactly the same potential and the same voltage with respect to its neighbour. The capacitor formed by this shell and its neighbour will discharge through the plasma channel on the other stack, with the current taking its path through the diode chain, the other series capacitors and the ground connection or respectively the shunt capacitance to ground. This discharge current passing through the diodes is one possible cause for the diode failures which have been observed at the novel accelerator prototype. After a capacitor in the column has discharged through a breakdown, the rectifier column will recharge that capacitor, which implies currents through the involved diodes. The recharging currents after a single breakdown are harmless for the diodes, repeated currents caused by frequent breakdowns however might exceed the actual diode power rating. This rating will be much lower than the number on the datasheet as the diodes operate in vacuum.

Breakdown between the inner shells of the top and bottom shell would happen when the AC waveform is at its lowest voltage. These breakdowns do not lead to high pulse currents in any of the diodes. However, they might lead to overvoltages on the capacitors of the AC column and therefore cause further breakdowns along the column. No matter whether this happens or not, all capacitors not at full charge after the event will be recharged during the next cycles. As mentioned before, this is not problematic for a single event but indeed for repeated or continuous discharges as have been observed across the now abandoned central insulator (PEEK tripod) when using it in the prototype experiments (see Section 3.2).

Maximum allowed currents for diodes

Forward currents in diodes put a certain heat load to the p-n junction which leads to temperature increase and to damage if a critical temperature is reached. In their data sheets diode manufacturers usually mention the *max. rectified current*, the *max. surge current* or *max. single surge current* or *max repetitive surge current*. These values usually refer to a $\int I^2 dt$ over a half cycle of a 50 Hz sine wave. According to [69] single surge pulses that do not exceed the limit to damage the diode with a single event can still cause damage through thermal fatigue cumulated over a number of such events. Baschnagel and Schlapbach therefore give two surge current limits for their diodes, one to survive one surge pulse and one to survive one hundred surge pulses. Furthermore measurements presented in the same article suggest that the $\int I^2 dt$ limit depends on the waveform and especially on the length T of the surge pulse. According to their data the $\int I^2 dt$ limit is approximately proportional to $T^{0.6}$, however their lowest data point is at 100 µs. As the standard values on datasheets are usually given for pulse lenghts of 10 ms, this is an important fact to be considered and contributes to the calculation of a minimum time over which the discharge of a certain stored charge Q through a diode needs to be spread out. If S is the $\int I^2 dt$ on the data sheet for the 10 ms pulse, and the $\int I^2 dt$ for pulse length t_p is named ξ it is given by:

$$\xi = S \cdot \left(\frac{t_p}{10ms} \right)^{0.6} \tag{3.1}$$

As it is a complicated task to quantify the effect of the actual waveform one may for simplicity assume a constant discharge current $I = \frac{Q}{t_p}$ over the length t_p of the discharge. With the constraint $I^2 t_p < \xi$ we get:

$$t_p > \frac{Q^2}{\xi} \quad \Leftrightarrow \quad t_p > \left(\frac{Q^2 \cdot (10ms)^{0.6}}{S} \right)^{0.625} \tag{3.2}$$

The *max. surge current* values are usually based on the assumption that between two surge events there is enough time for the whole diode to cool down or respectively for the heat from the first pulse to migrate from the p-n junction into the diode body. Therefore the dead time between two discharges is essential, however one would have to rely on thermal modeling of the diode itself or on dedicated experiments to make reliable predictions on required dead times.

It is therefore not clear whether the diode failures observed in our experiments originate from:

1. one-off single pulses which exceed the one time destruction limit
2. accumulation of thermal fatigue caused by single pulses
3. thermal fatigue caused by an accumulation of heat in the p-n junction due to rapidly succeeding single pulses which on their own would be harmless
4. general overtemperature of the whole diode body. Even normal operation without breakdowns dissipates a certain power in the diodes.

The diode failures so far have all been preceded by a time of successful conditioning which includes a large number of discharges. This seems to rule out point 1. Point 2 can be addressed by limiting the maximum current through the diodes with the help of series resistors. Point 3 can be addressed in the way the conditioning is carried out, i.e. quickly interrupting breakdowns and ensuring sufficiently long intervals between breakdowns. Point 4 can be addressed by improving heat transport away from the diodes. Other options are using faster diodes, diodes with lower reverse currents and generally more robust diodes.

Within the current system there is neither a mechanism to effectively ensure a minimum dead time nor any means of measuring the time between two discharges. After a discharge the capacitors recharge immediately, i.e. within a couple of AC cycles, and a discharge might even be maintained for longer than one AC cycle or revived from cycle to cycle as the lifetime of the plasma can well be in the µs range (see [68]). More or less sustained discharges have actually been observed during the experiments with our system.

Ways of limiting diode currents

A way of decreasing diode currents is of course the use of several diodes in parallel. The most straightforward way of limiting the pulse current in the diodes however is adding series resistance to the diode chains. As surge currents might flow through any diode which is higher in the stack than the breakdown event, all diode chains will need sufficient series resistance as protection, to limit currents according to Equation 3.2. The charge Q can be calculated from the drive voltage U and the capacitance C of the capacitor in question. However, as the current from the discharging capacitor flows through at least one more capacitor (depending on the location within the column), the discharge current comes from an effective capacitance which is substantially lower. With C being the capacitance of the discharging capacitor and C_{series} the capacitance of the whole series of capacitors connected to that capacitor the effective capacitance of the circuit is given by:

$$C_{eff} = \frac{C \cdot C_{series}}{C + C_{series}} \quad \text{or} \quad C_{eff} = \frac{a}{1+a} \cdot C \quad \text{with} \quad C_{series} = a \cdot C \tag{3.3}$$

The current 7-shell prototype has inter shell capacitances of approximately 250 pF, maximum inter shell voltages of 100 kV, and a diode rating of $S = (1\text{A})^2 \cdot 5ms$ (the

HVRT300 diode used in most of our experiments actually has a slightly higher rating, i.e. $3(\mathrm{A})^2 \cdot 10ms$, see Table 2.1 for an overview of high voltage diodes). In every discharge there are always at least 2 capacitances in series, reducing the C_{eff} to 250 pF resulting in a charge Q of 12.5 µC. According to Equation 3.2 the minimum value of t_p would then be 3.6 µs, which would require a constant current of 3.5 A to discharge the capacitor on this timescale. However the current in this RC-circuit decays exponentially, this means we may well allow for currents twice as high to begin with, which corresponds to a series resistance of approximately 15 kΩ. For lower operating voltages during commissioning experiments the required resistance would be even lower. The mentioned number for the resistance is a safe value as the decrease of the AC voltage on µs time scales has not been taken into account, also the extrapolation of the data presented in [69] which was made for Equation 3.1 is likely to overestimate the decrease of S for short pulses. Note also that the presented values are for breakdowns of the lowest capacitors in the stack, higher capacitors will have lower effective capacitances.

The series resistors have to be able to withstand the full shell to shell voltage of the final design of the system, but only for the duration of several µs. This will potentially allow for the use of resistors which are rated much lower for DC voltages, as the short pulse rating of resistors can be several times larger than their DC rating. However most manufacturers do not provide detailed data on this question so that experimental testing is crucial. Also the resistors need to have low inductance and low capacitance in order to be effective. Furthermore the resistor body should be as robust as possible. See Table 3.1 for a selection of high voltage resistors.

A series resistance of 15 kΩ corresponds to low voltage drops during normal operation, e.g. for the typical 100 µA beam current the voltage drop across the resistor would be 1.5 V with a power dissipation of 0.15 mW which is an order of magnitude

Resistor	max. V	Length	D	geometry	Coating	max. P
SLIM-MOX10803	20 kV	52.83 mm	8.64 mm	planar	epoxy	2.5 W
MOX910	15 kV	27 mm	8 mm	axial	silicone	3.8 W
MOX940	45 kV	77 mm	8 mm	axial	silicone	10 W
TT T 44	28 kV	50.8 mm	8.4 mm	axial	?	3.5 W
TT 4505	20 kV	51.2 mm	9 mm	planar	epoxy	2.8 W
TT WHVL 3	28 kV	43.5 mm	8 mm	axial	epoxy	5 W
TT WHVL 7	66 kV	83.5 mm	8 mm	axial	epoxy	10 W
TT WHVL 15	134 kV	158.5 mm	8.5 mm	axial	epoxy	20 W
RMC5WC5KM	25 kV	25 mm	8 mm	ax. bulk	?	5 W
106AS103LDS	15 kV	155 mm	7.9 mm	ax. bulk	dielectric	13 W
256AS103LDS	15 kV	155 mm	11.1 mm	ax. bulk	dielectric	16 W
HTE 152	48 kV	152 mm	9 mm	axial	epoxy	15 W

Tab. 3.1: A selection of high voltage resistors and their properties. For use as a protection resistor in our accelerator the most important property is robustness for short pulses of very high voltages and hence currents and power. These properties are not obvious from the data sheet and thus experimental assessment is required.

below the voltage drop across the p-n-junction of each individual diode in the diode chains (e.g. the HVRT300 diode has a voltage drop of about 45 V).

Another way of protecting the diodes is a further decrease of C_{eff} by adding more series capacitance to the current path or respectively limiting the current with a resistor at a different location. A possible way of doing this would be disconnecting the lowest DC shell from ground and putting a high R component between which would effectively limit the currents to the desired value. However stray capacitance between this shell and the grounded vessel has to be taken into account and will provide a parallel current path which will prove a limitation for this approach in a full scale system where the outermost shells are fairly large and rather close to the vessel, which makes the stray capacitances very large. However for some of the experiments with the 7-shell prototype

this is a promising approach as the effective capacitance of this current path will be of the same order as the stray capacitance between the lowest DC shell and the vessel. One must be aware that this approach induces considerable ripple on the DC side after a breakdown event and will also increase the ripple in the scenario of a load as well as without a load due to reactive currents caused by stray capacitances between the AC and DC columns . However the approach has two more advantages:

- It slows down the recharging of the capacitors and will therefore help to prevent continuous or quickly repeated discharges.

- It allows for diagnosis of the current state of the system at any given time by measuring the voltage dropped over the resistor (However one needs to be aware of possible stray capacitances through the measurement , e.g. in an off-the-shelf voltage divider).

This protection approach could possibly be used for the commissioning phase only, where a lot of breakdowns are expected. During normal operation the system could run with the protective resistors in series with the diodes only. This would also be a good approach for the full scale system. In this case it would be necessary to isolate the vacuum vessel itself from ground potential. It would have to be capable of surviving to float up to voltages of 100 kV above ground, which would involve some additional effort for, e.g. electrically insulating pumps and diagnostics equipment.

Another possible reason for diode damage is reverse overvoltage. One might argue that transients during breakdowns can result in higher reverse voltages across the diodes than during normal operation, although this is not obvious from analysing the circuit behaviour during breakdown. Regardless of whether this applies or not, a simple way to mitigate this is an increase of the number of diodes in series. Our experiments in

this regard showed that reverse overvoltage is not a main failure mode (see Section 3.5) and will therefore not be discussed any further.

3.5 Experiments on Circuit Protection

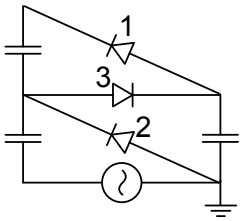

Fig. 3.21: Electrical circuit of the 2-3 shell insulator and diode test system.

The following experiments were done using the setup of Figure 3.18, with two DC shells and three AC shells (see also Section 3.2 for high voltage tests). This has the advantage that it is a small and simple test system which nevertheless tests most of the situations present in a larger scale system (remember that the highest currents flow in the lowest part of the stack). The electric circuit corresponds to Figure 3.21.

Parallel Diodes We performed an experiment where we used four parallel strings of five series diodes each instead of just one string. However this was unsuccessful, the diodes did not survive the conditioning any longer than they did with a single string and they were destroyed at 43 kV peak to peak input voltage (results for a single chain: 40 kV in one trial and 45 kV in another).

More Diodes in Series We have performed experiments with chains of 5, 8 and 15 diodes in series which were rated at 15 kV each. With the chain of four diodes we reached voltages of 40 kV and 45 kV before destruction, with the chain of eight diodes we once reached 60 kV and the chain of fifteen diodes was once destroyed at 50 kV. These results show that reverse overvoltage at these voltages and with the given number

of diodes is not a dominating failure mode. This is not surprising as even the chain of five diodes is higher rated (75 kV) than any voltage reached during those trials (60 kV). Actually during further experiments even a chain of nine diodes rated at 30 kV each, i.e. with a total rating of 270 kV was destroyed at an input voltage of 57 kV.

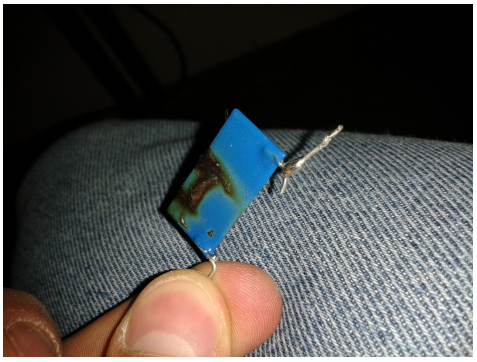

Fig. 3.22: Damaged Ohmite 204E resistor after intense conditioning. Sometimes discharges form between the resistor surface and the metallic shells as the hot resistor outgasses.

Protection Resistors in Series with Diodes For a number of tests three series resistors of 10 kΩ each and rated at 10 kV and 5 W each (Ohmite 204E) were put in series with the diodes on the diode chains (note that the power rating refers to use in air, in vacuum it is far lower). During breakdowns flashes would go over to the resistors on those diode chains. As a result of these tests the resistors were destroyed (one time at 66 kV and one time at 74 kV, see Figure 3.22 for destroyed resistor) with heavy burn marks, the diodes however were fully intact. The experiment was repeated with six of those resistors in series with varying number of diodes and those resistors broke once at 60 kV and once at 70 kV. Again the diodes were fully intact. The conclusion from this experiment is that the failure of the resistors was not due to overvoltage but due to overpower. For this reason a 1 nF capacitor in parallel with those resistors has been tested, so that a part of the impulse current during breakdown would go through the capacitor rather than the resistors. This of course does decrease the protection of the diodes. In this

configuration the resistors were destroyed again at an input voltage of 65 kV. In a new series of experiments we tested the Willow HTE 152 resistor (Figure 3.23. It is a far more robust cylindrical resistor which has a uniform resistive layer covering its entire surface. It protected the diodes very well, however after long operation we would eventually observe sparks coming from the surface of this resistor towards the shells. This lead to damage of the resistor surface. We therefore put three of these resistors in parallel (see Figure 3.24) in order to share the heat load between them. With this setup we did not have any resistor damage or sparking any more. However it increases the size of the diode chains and alternatives are under investigation. So called bulk resistors are a very promising solution (e.g. 256AS103LDS). They have cylindrical shape and the entire cylindrical body carries the current, whereas with conventional resistors it is only the surface that carries the current.

Fig. 3.23: Willow HTE 152 resistor rated at 48 kV. It was much more durable than the planar SLIM-MOX resistor, however after extended operation it started sparking from its surface (see burn mark in centre), which lead to the use of three resistors in parallel, see Figure 3.24

Potting Diodes and Resistors In order to improve the heat transport from the diodes, we potted them in a well conducting epoxy and glued this onto a piece of Aluminium Oxide with a high radiation constant. The measure lead to damage of the diodes at

Fig. 3.24: 3 Willow HTE 152 resistors in parallel. They are in series with the high voltage diodes. The chain also contains some LEDs which are used to qualitatively monitor currents going through the diode chain. This resistor setup is very robust and no damage has happened to the resistors in any of our tests.

much lower voltages than previously and was abandoned for the diodes and tried for the resistors. However it did not work well for the resistors either (see Figure 3.25), they cracked during breakdowns and the idea was therefore abandoned completely.

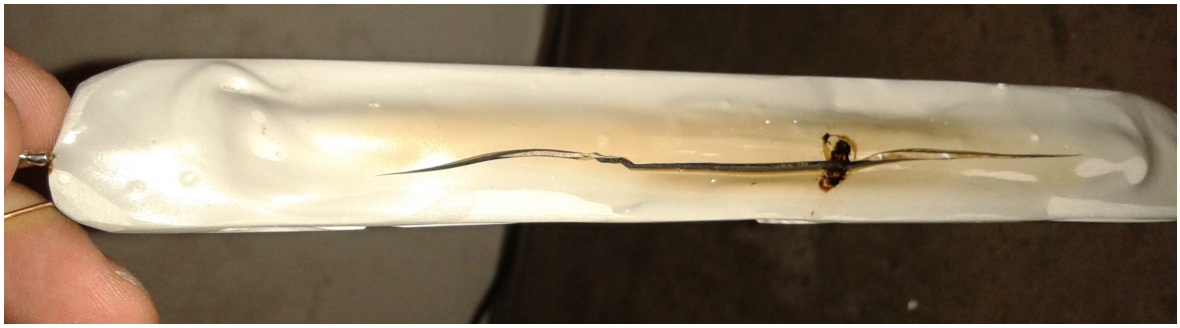

Fig. 3.25: Willow HTE 152 resistor potted in epoxy after an experimental trial. The whole package burst, leading to tremendous outgassing. The approach has been abandoned in favour of several resistors in parallel (see Figure 3.24).

Limiting the Currents to Ground on the DC Side I performed a series of experiments with a setup where the current between the lowest DC shell and ground was limited by a 8 MΩ resistor (see Figure 3.27). Of course the capacitance between the mentioned shell and ground contributes to AC and transient conduction as well. The voltage on the lowest DC shell was monitored with a resistive divider which was calibrated beforehand at 80 kHz. I found that 15±5% of the input voltage was dropped over the

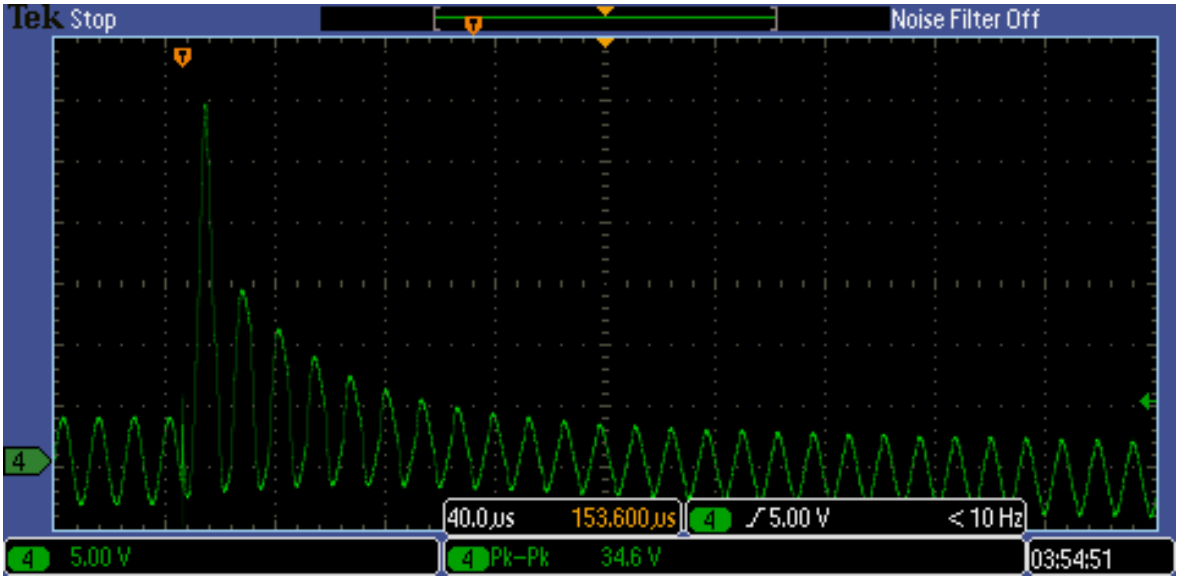

Fig. 3.26: Trace of the voltage dropped over the 8 MΩ resistor during a breakdown event, the divider ratio is about 3000, so the maximum voltage in this trace is approximately 90 kV.

8 MΩ resistor. During breakdowns however larger parts of the input and sometimes even the full input voltage was dropped over the resistor, as shown in Figure 3.26. The voltage dropped depends on the AC phase at the time of the breakdown and on which side of the system the breakdown occurs. The experiments were carried on up to an input voltage of 109 kV. In contrast to all other previous experiments flashes on the diode chains were never observed. After the experiment the diode chains were inspected and both the resistors and diodes on them were fully intact. This together with the voltage drop measured over the 8 MΩ resistor is evidence for the effectiveness of this protection approach. The experiments were stopped at 109 kV input voltage (note that the effective drive voltage is lower, as 15 % was dropped over the resistor, i.e. 93 kV) as the system pressure would increase after a very short period of operation. It points to the heating up of components and is likely to do with limitations of the inter shell insulators. The 10 mm insulators which we used for this experiments do not have threads and have a voltage limit at about 90 kV (see Section 3.2). The reached voltage level of 93 kV is to be seen as a success of this protection method, as comparable

voltages have not been reached with other methods. Future investigations could include similar experiments with a better inter shell insulator design and of course experiments with a larger subset of shells (rather than just 2/3).

3.6 Experiments with more than 2/3 Shells

Experiment with 4/4 Shells

The use of more shells than the 2/3 shell test system requires longer conditioning times and therefore longer operation of the diode chains. Also it involves higher overall voltages and therefore higher energies of potential secondaries. Whereas the 2/3 shell system tests focused on the validation of single components, I also carried out some experiments with a system of 4/4 shells in order to demonstrate the scalability of the approach. Generally in these experiments the diode chains would be the weakest component of the setup and fail after a certain time. Improvement of the series protection resistor together with the use of a faster and more robust diode (i.e. UX-F2CL15 instead of HVRT300) lead to significant improvements of the achieved voltage. With the help of the automatic high voltage conditioning software system (see Section 3.3) I was able to condition the system up to a voltage of about $\approx$55 kV and to stably operate it at that level. The future programme for further increase of voltage includes improvements on the inter shell insulators as well as a structured research programme into the robustness of diode chains. For this purpose a dedicated test system is under development which will be able to measure the currents through the diode chains during operation and breakdown via fibre optic links. It will also be able to measure their temperature using fibre optics. This programme will boost the development of a diode and protection system configuration robust enough to support the required voltages.

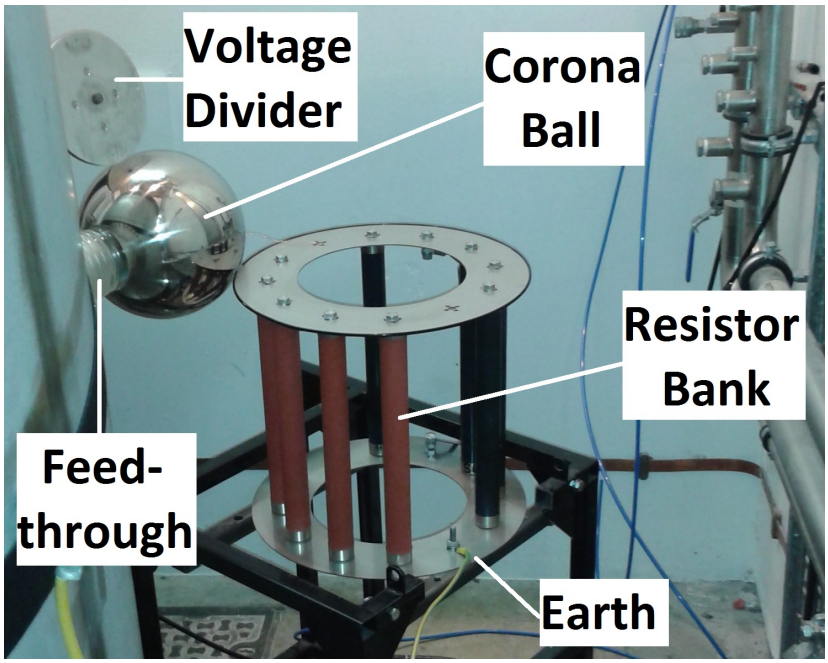

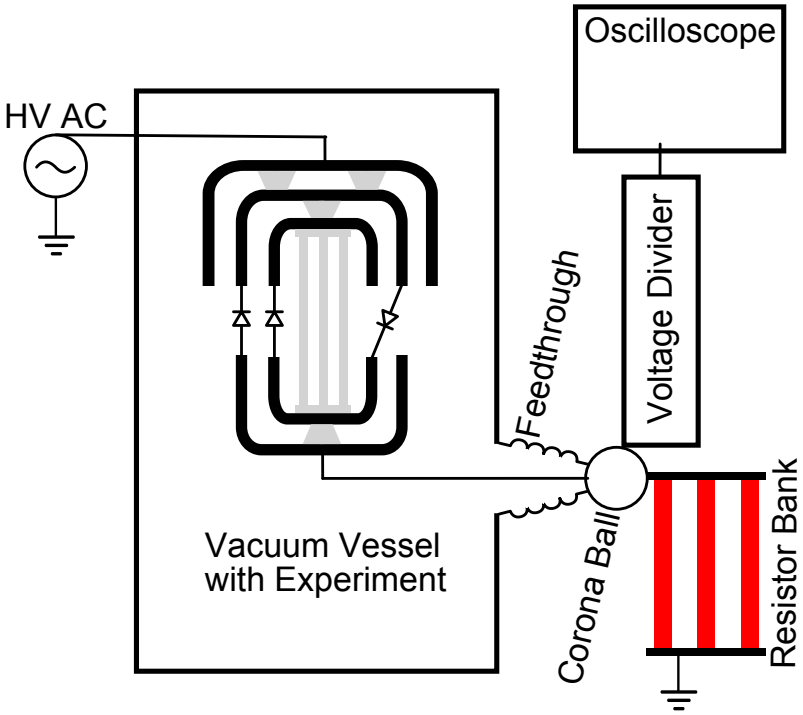

Fig. 3.27: The setup for the earth limit resistor protection. The ground DC shell of the system is connected to a feedthrough, which has a corona ball on the air side. A resistor bank of parallel HV resistors (rated above 100 kV) with 8 MΩ resistance contacts the corona ball by physically touching it. The other end of the resistor bank is connected to ground. The resistor was placed outside vacuum to allow heat dissipation. A voltage divider is connected to the corona ball in order to measure the voltage waveform on the ground shell as shown in Figure 3.26.

Voltage multiplication in 7-shell cascade

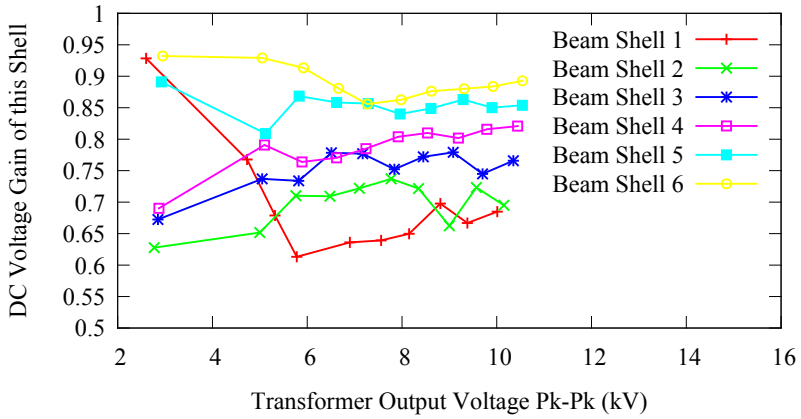

Fig. 3.28: Contribution of the single stages of the system towards the total multiplication. The lines are piecewise linear interpolations to guide the eye. Adding up the single values of all stages leads to the total multiplication ratio of the system. The ideal value of a single stage would be 1.0. Note that the accuracy of the measurement is very low, e.g. the first two values of Beam Shell 1 are far too high.

In order to measure the voltage on the terminal (represented by the centre shell) a resistive voltage divider with a 15 GΩ resistor and a 3 MΩ resistor has been connected to the terminal and brought out through a cylindrical PEEK insulator which comes through a series of holes in the shells. It was found that the system multiplication ratio is roughly 4.8 for the 7-shell system. As every gap between two shells represents a capacitor, the 7 shell-system is a stack of 6 capacitors on each side and the multiplication ratio in an ideal system would be 6. The actual value of 80% of the ideal value is due to stray capacitances between not neighbouring shells as well as finite reverse recovery times and forward voltages of the diodes ([40]). For a more detailed analysis the DC voltages on each individual shell were measured whilst varying the amplitude of the AC input signal. It was found that the stages closer to the terminal contribute less to the multiplication than those closer to the AC input (see Figure 3.28). This confirms theoretical predictions and simulations, which say that the effects of stray capacitances and non-ideal behavior of diodes add up towards the high voltage side

of the system ([40]). Although the accuracy of the measurement is not sufficient for thorough quantitative statements, this is an interesting and useful confirmation of our understanding of the system.

3.7 Conclusion

The work undertaken in this chapter focuses on the testing and development of the key components for the shell based voltage multiplier. The key issues were leakage currents and breakdowns across insulators on the one hand and damaged diodes on the other hand. For the insulator breakdown good contact between the insulator and the shell turned out to be crucial in order to avoid triple junction stresses as far as possible. The stress reducing metal plate insulator design screwed onto the shells turned out to do this task really well. It has passed the test up to a voltage of 120 keV which is slightly above specification. It also has the advantage that the top shells can be held from above by their insulators. Thus no tripod insulator is needed. The tripod insulators in our tests were not stable and showed glowing surface discharges as well as frequent breakdown. The second key issue are the diodes. I experimented with protection resistors with some success. However I only reached about half of the voltage specification for the 7-shell system in this setup. The diodes would still get destroyed during extended operation. The diode protection and heat management will therefore need some more attention in further research programmes. It needs to be understood which mechanism is mainly responsible. Then a more suitable diode type can be chosen or developed and further protection measures can be implemented.

4. DEVELOPMENT OF BEAM DIAGNOSTICS AND CHARACTERISATION OF ION SOURCE

The ion source is an integral part of the accelerator system. Given the compactness of the novel concept, there is no dedicated LEBT. A good understanding of the quality

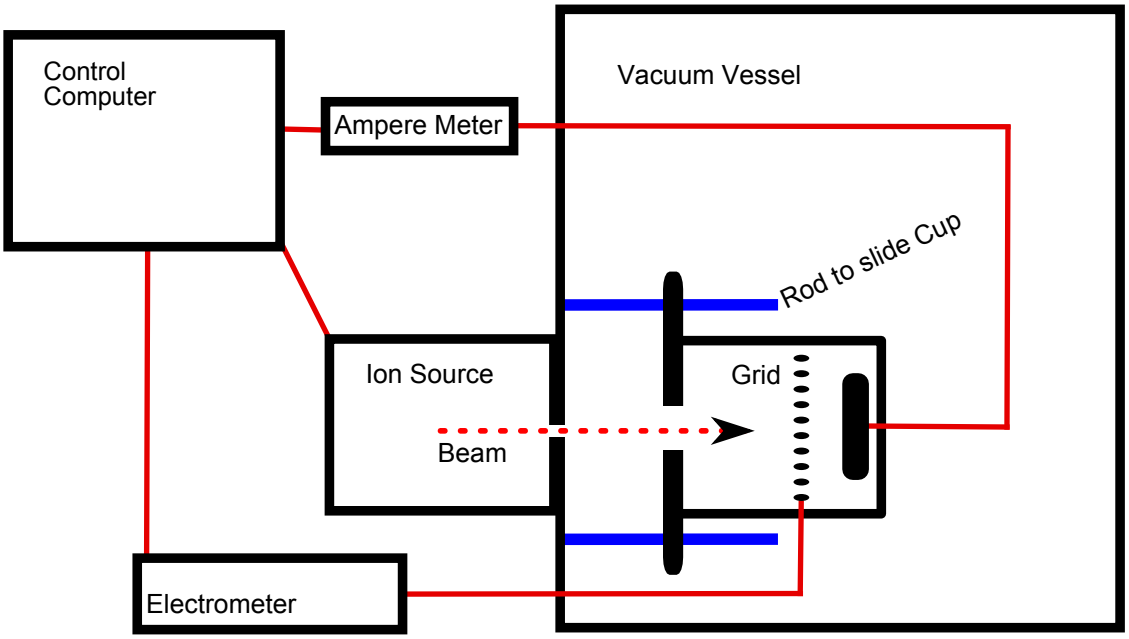

Fig. 4.1: The setup of the ion source and the diagnostics. The Faraday Cup which has the wire grid inside is held by rods (blue) directly in front of the ion source. It can be slid up and down the rods to vary the distance from the ion source.

of the beam coming from the source is therefore an important prerequisite for successful operation of the machine. I have therefore dedicated considerable efforts to the characterisation of the ion source. For beam current measurements I used a Faraday Cup which we manufactured according to an existing design. For measurements of the beam profile I designed and developed a wire grid including a data acquisition system and analysis software (see Figure 4.1). This chapter reports about my work on the

	Required	Achieved
Beam Current	100 µA	140 µA
Beam Diameter	≈8 mm	≈6 mm
Beam Divergence	≈2 deg	≤1 deg

Tab. 4.1: Required and achieved parameters for the ion source.

development of the wire grid and presents the insights on the ion source obtained with the Faraday Cup and the wire grid.

4.1 Faraday Cup

We mounted a Faraday Cup directly in front of the ion source, which can be used to measure its beam current. The cup is held by rods which go through holes on the side of the cup. In order to make measurements at different distances, the cup can be slid up and down the rods, towards and away from the ion source. The Faraday Cup has an entrance aperture with a magnetic filter field which makes it impossible for fast electrons to enter the cup. In this way it is ensured that only H^- ions will enter the cup. The aperture sizes at the entrance can be changed so that the accepted beam diameter or the measured fraction of the beam can be altered. Furthermore the cup has a secondary electron suppression field inside, in order to prevent secondary electrons to leave the cup and falsify the measurement. Figure 4.2 shows that without using the suppressor the measured currents are 10 % lower than the actual beam current.

Of course one always has to keep in mind that the Faraday Cup is not able to tell how much of the actual beam makes its way through the aperture and how much is blocked by it. This could only be achieved by repeated measurements with different aperture sizes, however those would have to rely on the beam being perfectly aligned with the cup. They would also require the ion source being capable of reproducing exactly the

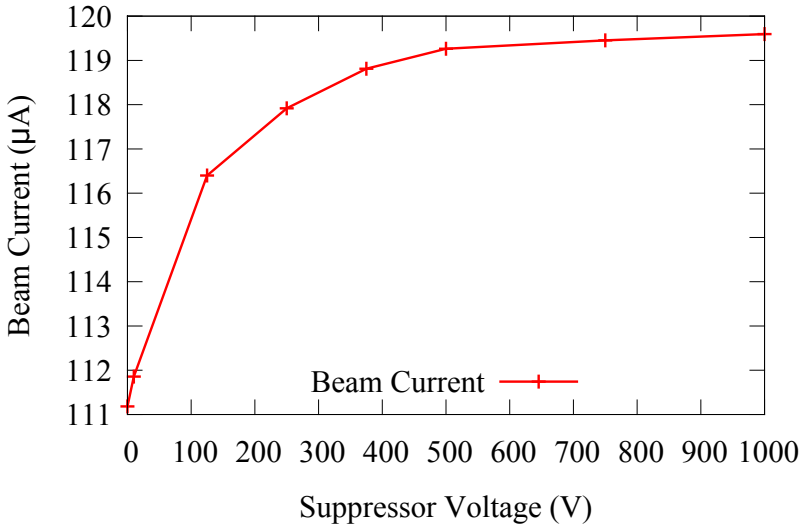

Fig. 4.2: Relation between the applied suppressor voltage and the measured beam current. Without suppression one secondary electron for every ten H^- leaves the cup and falsifies the measurement. 500 V are sufficient to suppress most of this effect. The lines are piecewise linear interpolations to guide the eye.

same beam after the vacuum has been broken in order to change the aperture. These facts bring too many uncertainties for a reliable measurement of the beam profile. I therefore designed a wire grid, which is capable of measuring a projection of the beam profile in two dimensions.

4.2 Wire grid

A very compact wire grid has been developed for the purpose of measuring the beam profile in front of the ion source, i.e. before any additional acceleration.

4.2.1 Mechanical Structure

The wire grid consists of two sets of parallel wires, one of them aligned horizontally and one of them vertically. In order to leverage existing hardware the grid has been designed to be inside the Faraday Cup (see Figure 4.3). This enables use of the electron suppression magnets if required and of the Faraday Cup housing to shield the beam plasma . The grid is designed in a way that it covers the whole area that is visible

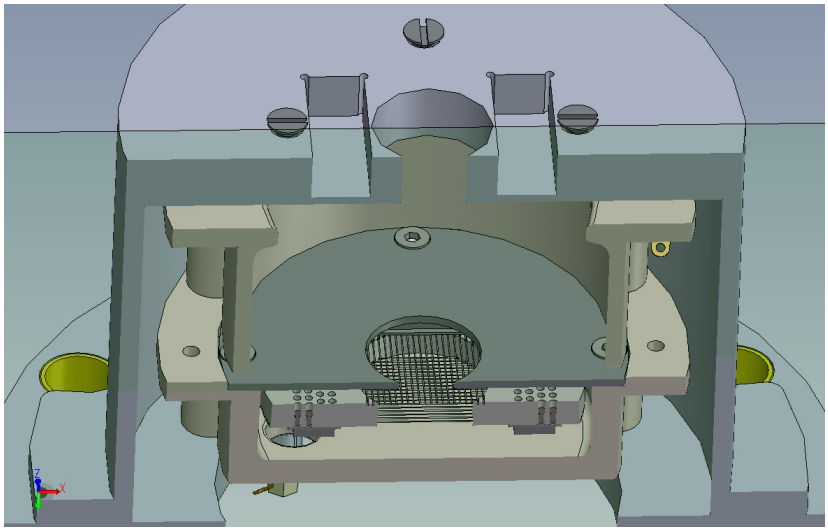

Fig. 4.3: Assembly of Faraday Cup with Wire Grid inside the back part of the cup. Note that the grid in this picture corresponds to the one in Figure 4.7, whereas the final design uses a grid on a PCB (see Figure 4.8). Also after some trials a hole was cut into the back plate of the cup in order to prevent the creation of secondary electrons by H^- incident on that back plate (see Figure 4.9)

behind the maximum aperture of R = 10 mm. From the measurement of the beam profile one can of course deduce a relative measurement of the current from integrating the measured profile. The wire spacing of the wire grid is 1 mm. The wires are made of Silicon Carbide (SiC) with a thickness of 0.2 mm. As a lot of secondary electrons are produced on the surface of the wires, a direct measurement of the beam profile would be rather complicated. We therefore use a positive bias on an electrode surrounding the grid and thus measure the difference of the H^- current and the current of secondary electrons leaving the wires. The measured current is directly proportional to the actual H^- current.

4.2.2 Data analysis and calculation of beam profile

Beam profiles

There are two current density distributions that might be observed with our H^- beam: A Gaussian distribution as observed with most space charge compensated beams or

a Bennett distribution as sometimes observed for non space charge compensated H^- beams (see Figure 4.4 for a plot of the two distributions). It is not entirely clear which one of these distributions we will observe for our beam and therefore the analysis has to be done for both in order to assess which of the two models represents reality better, if the measured data is at all good enough to make a distinction between the two preferred models.

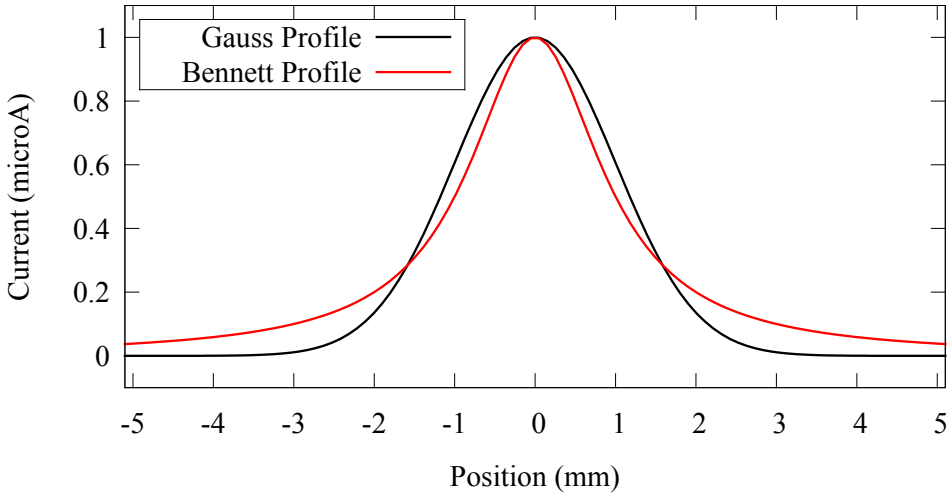

Fig. 4.4: A plot of the Bennett (red) and Gauss (black) distributions with a width b or resp. σ of 1 mm.

Gaussian profile

$$j(x,y) = I_{beam} \cdot \frac{1}{2\pi\sigma_x\sigma_y} e^{-\frac{x^2}{2\sigma_x^2}-\frac{y^2}{2\sigma_y^2}} \tag{4.1}$$

Bennett profile

$$j(x,y) = I_{beam} \cdot \frac{1}{\pi b_x b_y} \frac{1}{\left(1+\frac{x^2}{b_x^2}+\frac{y^2}{b_y^2}\right)^2} \tag{4.2}$$

Profile reconstruction from wire grid

The beam profile can be reconstructed by fitting the experimental data to the expected current density distribution function. When actually doing measurements we never measure the current density directly. We measure the integrated current on a certain

surface area, in the case of our wires this a long very narrow rectangle. Therefore we cannot simply fit to the 2D current density distribution. Some careful considerations on appropriate fit methods are required.

Gaussian profile Assuming an elliptical distribution, we can do the integration over a wire of infinite length in the y-dimension. As the wire is thin, we will approximate the integration along the width d_{wire} of the wire by just multiplying with the width. We then get:

$$\frac{I_{measured}(x)}{d_{wire}} = I_{beam} \cdot \int \frac{e^{-\frac{x^2}{2\sigma_x^2}-\frac{y^2}{2\sigma_y^2}}}{2\pi\sigma_x\sigma_y}\, dy \tag{4.3}$$

$$= I_{beam} \cdot \frac{1}{\sqrt{2\pi}\sigma_x} e^{-\frac{x^2}{2\sigma_x^2}} \tag{4.4}$$

This is a 1D Gaussian distribution. However, our wires are not of infinite length and integration along the length of the wire needs to take into account, that, depending on the x-coordinate of the wire, parts of the wire will be shadowed by the aperture in front of it. Therefore the integration should be performed only along the length that is accessible to the beam. We are using a circular aperture. Also a possible displacement of the whole distribution in the y dimension (z_y) has to be taken into account. The y integration then needs to be performed along the length $2y$ with $y^2 = r^2 - x^2$, r being the radius of the aperture, i.e. from $-\sqrt{r^2-x^2} - z_y$ to $\sqrt{r^2-x^2} - z_y$. This yields the following relation for the current measured on the wire:

$$\frac{I_{measured}(x)}{d_{wire}} = I_{beam} \cdot \int_{-\sqrt{r^2-x^2}-z_y}^{\sqrt{r^2-x^2}-z_y} \frac{e^{-\frac{x^2}{2\sigma_x^2}-\frac{y^2}{2\sigma_y^2}}}{2\pi\sigma_x\sigma_y}\, dy \tag{4.5}$$

$$= I_{beam} \cdot \frac{1}{\sqrt{2\pi}\sigma_x} e^{-\frac{x^2}{2\sigma_x^2}} \cdot \frac{1}{2}\left(\mathrm{Erf}\left[\frac{\sqrt{r^2-x^2}-z_y}{\sqrt{2}\sigma_y}\right] + \mathrm{Erf}\left[\frac{\sqrt{r^2-x^2}+z_y}{\sqrt{2}\sigma_y}\right]\right) \quad (4.6)$$

With Erf(x) being the error function. This is the 1D Gaussian distribution in x from Equation 4.4 multiplied with a correction factor which accounts for the wire not being infinitely long:

$$\frac{1}{2}\left(\mathrm{Erf}\left[\frac{\sqrt{r^2-x^2}-z_y}{\sqrt{2}\sigma_y}\right] + \mathrm{Erf}\left[\frac{\sqrt{r^2-x^2}+z_y}{\sqrt{2}\sigma_y}\right]\right) \quad (4.7)$$

this factor is between 0 and 1 and does only depend on σ_y, z_y and x but not on the fit parameters σ_x and z_x. This means a Gaussian fit in x could be done once the factors have been calculated using the numbers from the y-distribution. Of course for the fit of the y-distribution from the y-wires' data there will be a correction factor depending on σ_x and z_x. Therefore it seems appropriate to adapt the following procedure:

1. Measure data with x and y wires
2. Do a Gaussian fit on the y data, determining σ_y and z_y
3. Use σ_y, z_y to correct the x data with the correct factor given in 4.6
4. Do a Gaussian fit on the corrected x data, determining σ_x and z_x
5. Use σ_x, z_x to correct the y data
6. Do a Gaussian fit on the corrected y data, determining σ_y and z_y
7. Go to step 3

A suitable number of iterations between step 3 and step 6 have to be made until the solution converges. I have implemented this procedure in the LabVIEW control system.

This enables live analysis of the beam profile whilst running experiments with the ion source.

Bennett profile For the Bennett profile integration along an infinitely long wire in the y-dimension leads to:

$$\frac{I_{measured}(x)}{d_{wire}} = \frac{I_{beam}}{\pi b_x b_y} \cdot \int \frac{1}{\left(1 + \frac{x^2}{b_x^2} + \frac{y^2}{b_y^2}\right)^2} \; dy \tag{4.8}$$

$$= \frac{I_{beam}}{b_x} \cdot \frac{1}{2} \cdot \frac{1}{\left(\sqrt{1 + \frac{x^2}{b_x^2}}\right)^3} \tag{4.9}$$

However, according to the argument in the treatment of the Gaussian profile, the limited length of the wires leads to a smaller current actually measured on any wire:

$$\frac{I_{measured}(x)}{d_{wire}} = \frac{I_{beam}}{\pi b_x b_y} \cdot \int_{-\sqrt{r^2-x^2}-z_y}^{\sqrt{r^2-x^2}-z_y} \frac{1}{\left(1 + \frac{x^2}{b_x^2} + \frac{y^2}{b_y^2}\right)^2} \; dy \tag{4.10}$$

$$= \frac{I_{beam}}{\pi b_x} \cdot \left[\frac{\frac{y}{b_y}}{2\left(1 + \frac{x^2}{b_x^2}\right)\left(1 + \frac{x^2}{b_x^2} + \frac{y^2}{b_y^2}\right)} + \frac{1}{2\left(\sqrt{1 + \frac{x^2}{b_x^2}}\right)^3} \cdot \tan^{-1}\left(\frac{\frac{y}{b_y}}{\sqrt{1 + \frac{x^2}{b_x^2}}}\right) \right] \Bigg|_{y=-\sqrt{r^2-x^2}-z_y}^{y=\sqrt{r^2-x^2}-z_y} \tag{4.11}$$

$$= \frac{I_{beam}}{b_x} \cdot \frac{1}{2} \cdot \frac{1}{\left(\sqrt{1 + \frac{x^2}{b_x^2}}\right)^3} \cdot \left[\frac{\frac{y}{b_y} \cdot \sqrt{1 + \frac{x^2}{b_x^2}}}{\pi\left(1 + \frac{x^2}{b_x^2} + \frac{y^2}{b_y^2}\right)} + \frac{1}{\pi} \cdot \tan^{-1}\left(\frac{\frac{y}{b_y}}{\sqrt{1 + \frac{x^2}{b_x^2}}}\right) \right] \Bigg|_{y=-\sqrt{r^2-x^2}-z_y}^{y=\sqrt{r^2-x^2}-z_y} \tag{4.12}$$

this is the distribution from Equation 4.9 multiplied with a correction factor to take account of the finite length of the wires:

$$\left[\frac{\frac{y}{b_y} \cdot \sqrt{1+\frac{x^2}{b_x^2}}}{\pi\left(1+\frac{x^2}{b_x^2}+\frac{y^2}{b_y^2}\right)} + \frac{1}{\pi} \cdot \tan^{-1}\left(\frac{\frac{y}{b_y}}{\sqrt{1+\frac{x^2}{b_x^2}}} \right) \right] \Bigg|_{y=-\sqrt{r^2-x^2}-z_y}^{y=\sqrt{r^2-x^2}-z_y} \tag{4.13}$$

Now a procedure similar to the one for the Gaussian beam profile can be devised. However, the correction factor in Equation 4.13 does depend on b_x, which means that for each iteration step the b_x resulting from the fit of the preceding step has to be used to calculate the correction. Apart from this the procedure can be completely the same one as for the Gaussian profile. I have implemented both fit methods into the LabVIEW control system. They can be used simultaneously in real time measurements in order to work out which distribution represents the actual beam profile better.

4.2.3 Data Acquisition and Software

Every single wire of the wire grid is connected to a separate channel of two 32-channel electrometers (I3200 by PTC Ltd., see Figure 4.5) via multi way vacuum feedthroughs and suitably shielded cables. In this configuration the currents on all wires can be measured individually at the same time and with considerably high precision ranging down to the pA range. The measurements on the I3200 are initiated and read out by the control software via serial communication. Each channel consists of a capacitor, an operational amplifier and an ADC. The integration time of course affects precision and noise but is limited by the capacitance and a maximum voltage of 5 V. The channels have two capacitors 10 pF and 1000 pF and one can choose which one to use for the measurement depending on the actual current. To further increase precision

and reduce noise effects one could of course do statistics with a set of measurements taken at the same beam conditions. The software module (a LabVIEW class within

Fig. 4.5: A photo of one of the two 32-channel high precision electrometers used for the current measurements with the wire grid. The electrometer is an off-the-shelf component sold by Pyramid Technical Consultants Ltd.

the framework described in Section 2.8) that initiates the electrometer measurements displays the results in a user interface in one graph each for the horizontal and vertical wires. The settings for the electrometer are accessible from the same user interface. I also implemented a simulation of the grid which generates measured data for Gaussian and Bennett profiles and adds noise to them. I made another LabVIEW class for the analysis of the measured data. I implemented a method for each analysis step described in Section 4.2.2. The class can get measurement data from the other class, which operates the grid, and then analyse it in its own user interface (see Figure 4.6). As with all classes in the control system, they can be used by each other and also by applications. It is therefore possible to use the data acquisition from the grid and the data analysis module in an application, e.g. to automatically find the parameter with the smallest beam diameter for a given set of other parameters in a multi parameter field like the ion source settings. In fact I developed and used an application that takes

not only the beam profile data, but all the other ion source settings, and stores it all in one file during experiments. The data reconstruction and fitting process has been

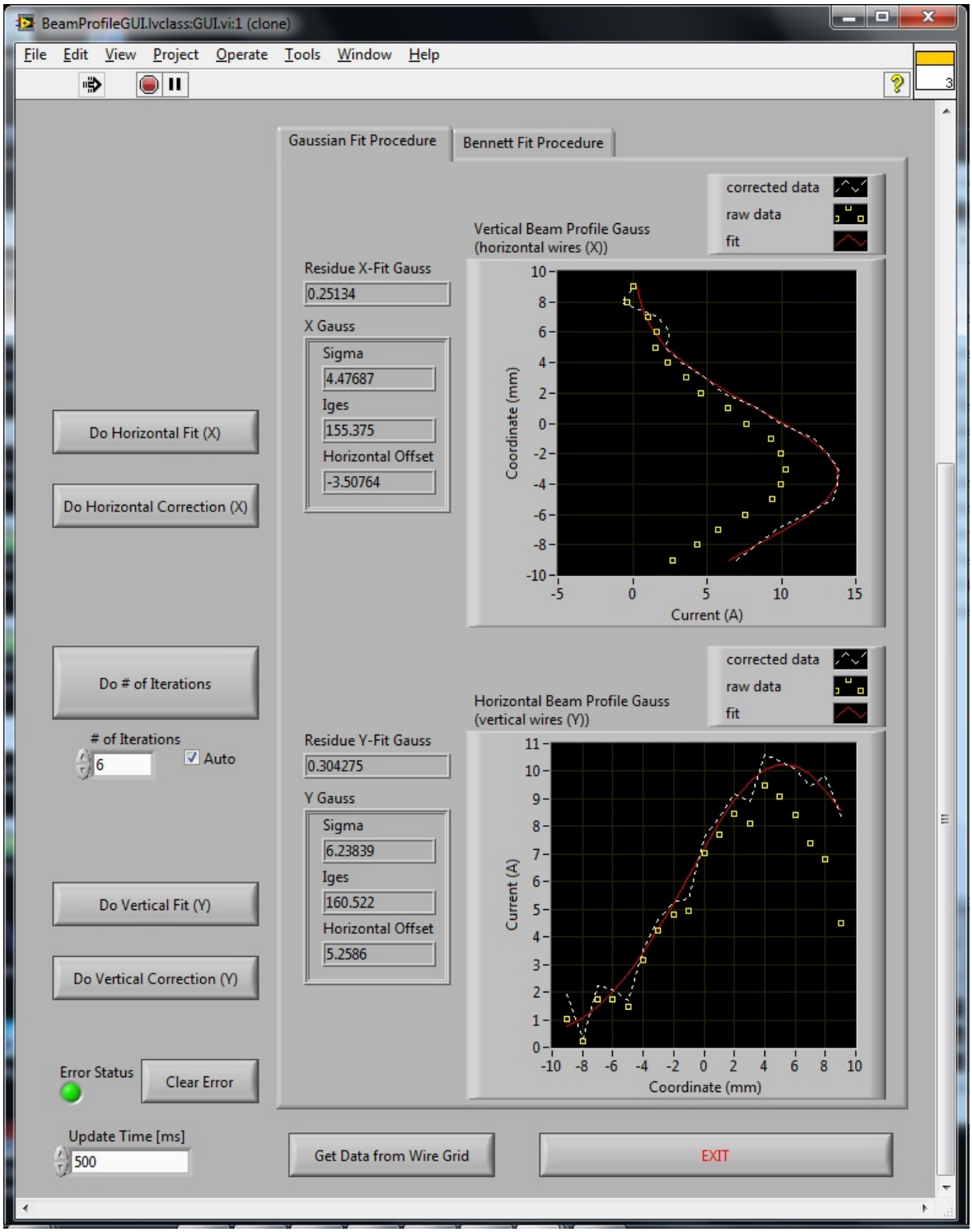

Fig. 4.6: Screenshot from the analysis software module (in this case with simulated data for software validation). The various analysis steps can either be performed manually using the appropriate button or a whole iteration or a number of iterations can be performed at once and automatically with each data taking from the wire grid.

validated for a large number of different settings of simulated beam profiles and noise

levels. Generally the reconstruction of narrow beams is much more robust than that of very broad beams, as with broad beams only a very small fraction of the beam actually hits the wires. At very low noise levels the process is capable of exactly recovering the actual beam profile parameters with perfect accuracy and one can very well distinguish between Gaussian and Bennett shaped beams. With increasing noise levels this changes however, and it gets increasingly hard to distinguish between the two shapes.

4.2.4 Development Process and Commissioning

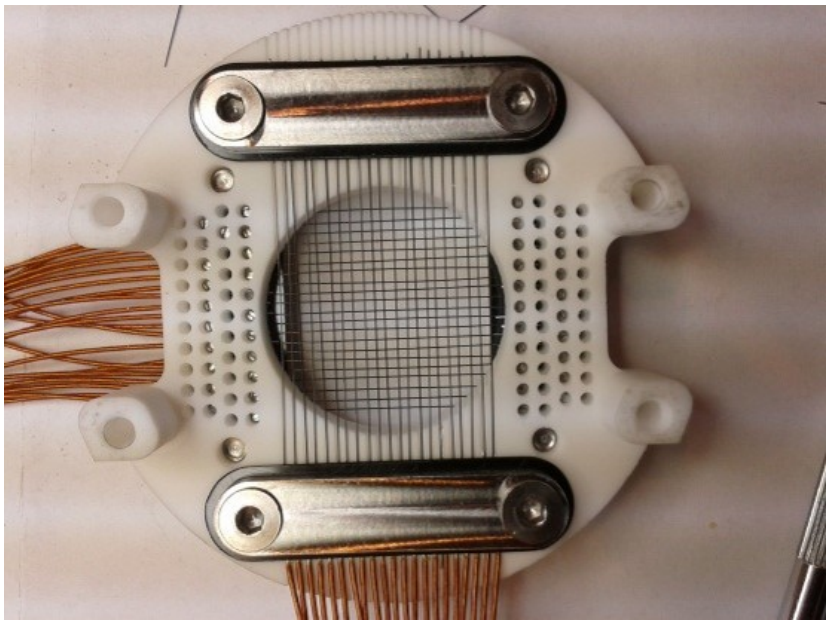

Fig. 4.7: The Wire Grid on a Macor holder. This design is very fiddly to put together and was abandoned in favour of a PCB (see Figure 4.8).

Developing the hardware for a wire grid with just 1 mm wire spacing at reasonable cost turned out to be a very challenging task. All the wires need to be electrically isolated from each other and individually and correctly connected all the way through to the electrometers which are situated in the control room outside the radiation bunker. Also the whole assembly needs to be able to withstand sufficiently high temperatures due to the beam power impact on the wires. Our first design iteration was a ceramic (Macor) holder structure which would hold wires on both sides (see Figure 4.7). The

wires would be guided by appropriate grooves and they would be held in place by tiny screws. Mechanically and electrically putting this together turned out very fiddly. Especially getting the wires straight rather than bent was very hard. Also, due to the many threadholes, the Macor component was prone to physically breaking in halves. We therefore replaced the setup with a different design, i.e. a PCB board suitable for high temperatures (see Figure 4.8). The wires are held by a piece of ceramic with guide holes on one side (electrically insulating) and by custom designed copper clamps soldered onto the PCB on the other side. The copper clamps make electrical connection to a track on the PCB. This design is much easier to assemble with the wires turning out straight and it is also more robust. The correct connection of each wire into the right channel of the electrometer was tested by injecting currents into each wire when it was all wired up as it would be during operation. The software is constructed in a way that the matching of physical grid wires to electrometer channels or respectively coordinates on the screen can be changed in the software quickly during testing in order to correct unintended swaps that occured during the wiring.

Secondary Electrons

Secondary electrons play an important role in the operation of the wire grid. The H^- (or in fact any other particles extracted from the ion source) creates secondary electrons when it hits the wires as well as when it hits the back plate of the Faraday Cup. In order to make the spatial origin of secondaries unambiguous we cut a hole into the back plate of the Faraday Cup after some experimental trials (see Figure 4.9). The beam then goes through the cup and grid assembly and only creates secondaries on the wires. Secondaries created on the wires are emitted in all directions and can therefore hit other wires, thus making the measurement much harder to interpret. We therefore

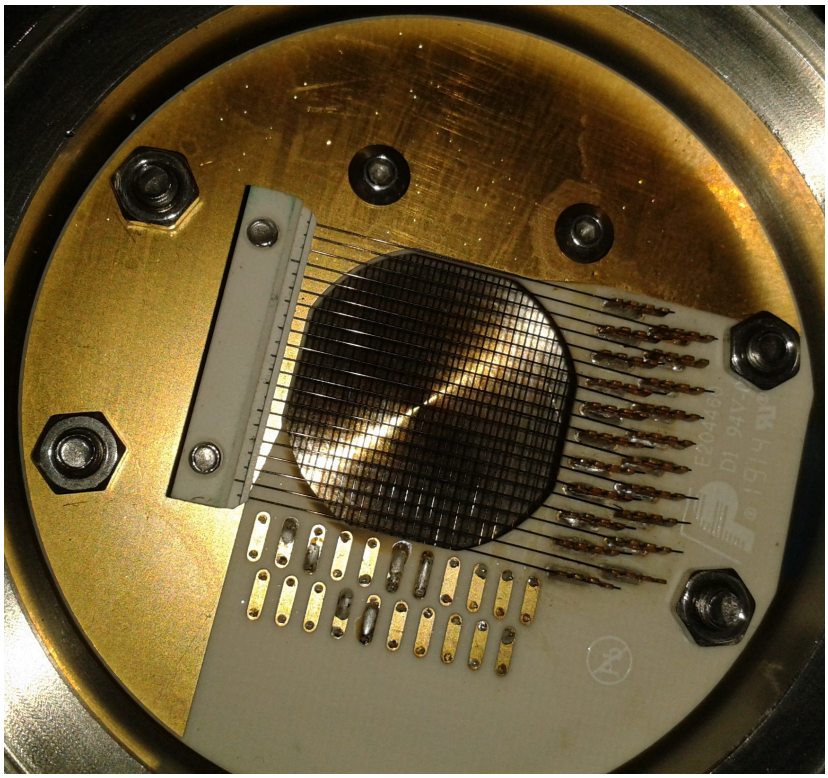

Fig. 4.8: The Wire Grid on a high temperature suitable PCB. The wires are held by little clamps which are soldered onto the PCB. This setup replaced an earlier design iteration which used a Macor holder structure with screws (see Figure 4.7).

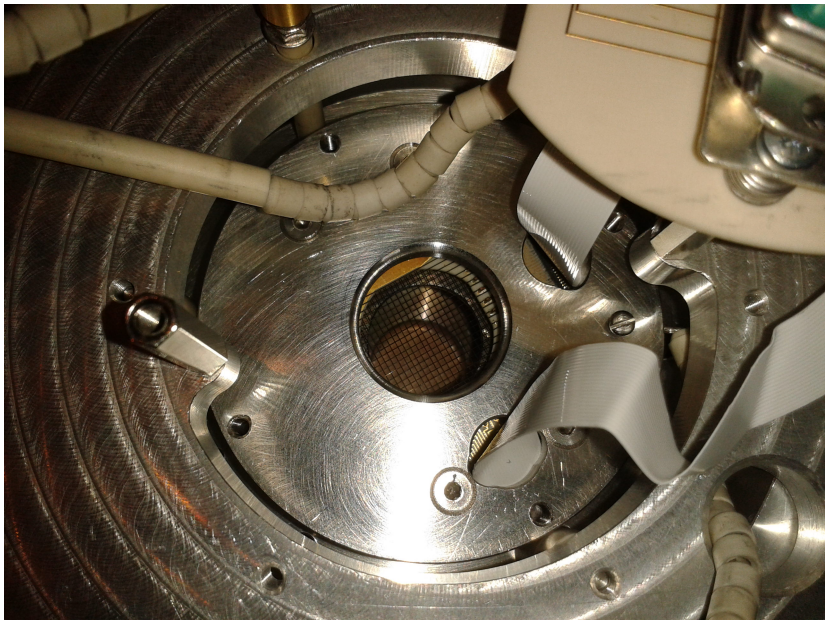

Fig. 4.9: The Faraday Cup based Wire Grid assembly seen from the back. The beam goes through the cup and the grid and leaves the assembly through the hole in the centre. The white 21-way cables serve as electrical connections to the wires of the grid.

introduced a bias on the electrode surrounding the wire grid (i.e. the one which then had an entrance and an exit hole and the grid inside it). The field from this bias must be weak enough not to disturb the beam from the ion source and strong enough to guide all secondaries from their origin onto the electrode without hitting another wire. If this is achieved, the measured electrical current $I_{measured}$ on a given wire will be directly proportional to the actual particle current N_{beam} (i.e. the number of particles per second) hitting that wire, as long as the beam consists of just one particle species with charge state q:

$$\frac{I_{measured}}{e} = N_{beam} \cdot (q + \gamma) \tag{4.14}$$

with the elementary charge e and the secondary emission coefficient γ, which is a function of the wire material, the particle type, its charge state, its energy and its incident angle on the wire. Obviously the instrument is also suitable for measuring neutral beams such as H^0 as these too have a finite γ. Note that there is a scenario where a beam might not be measured or at least strongly attenuated when $\gamma \approx -q$.

It is not easy to find accurate data for secondary electron emission coefficients. A review of the data in [70] suggests that at an energy of 10 keV the coefficients for H^0, H^- and OH^- incident at normal angle are quite similar for most materials and somewhere below or close to 1. However according to the same source the incident angle plays an important role and the coefficients can be several times larger for smaller angles. This suggests that stronger contributions are to be expected from the edges of the wires, where the particles hit at a very flat angle. Given the scarcity of accurate experimental data it seems not appropriate to attempt a rigourous systematic analysis. From our measurements (see next Sections) it is apparent that the coefficient on our wires is well above 1, as otherwise we would not see such a strong signal for a negative beam. However it should be remarked, that a potential signal of H^0 incident on the wires

would appear artificially amplified as it scales with γ rather than $\gamma - 1$ as is the case for H^- and OH^-.

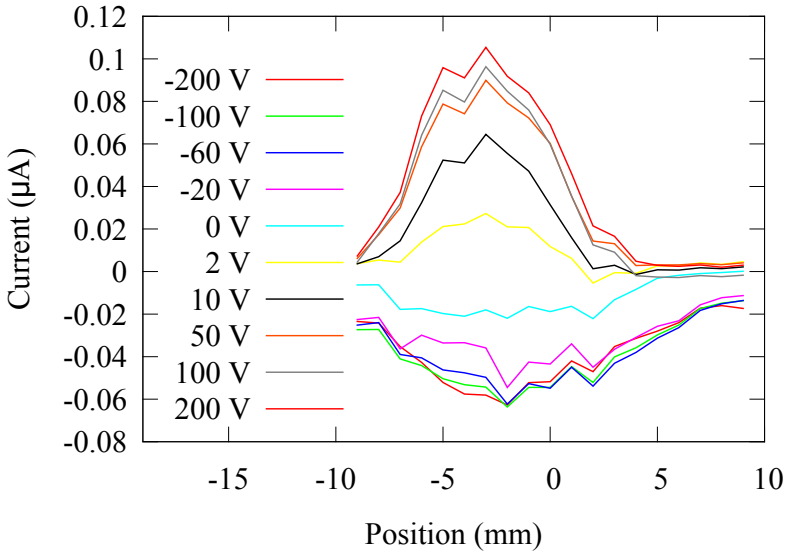

Fig. 4.10: Vertical beam profile measurements (i.e. from horizontal wires, these are in front of the vertical ones, i.e. the beam hits them first) at different bias voltages. Each line in this diagram corresponds to a beam profile measurement at a given bias voltage. The lines are piecewise linear interpolations between the current measurements taken by the individual wires to guide the eye. Bias voltages above 10 V impact the profile mainly quantitatively, whereas the shape does not change very much.

We performed a series of experiments with different bias voltages to study the impact of the biasing and the required bias voltage to achieve measurements which are not significantly distorted by secondary electrons hitting the grid wires (see Figures 4.10 and 4.11). For the profile on the first set of wires a bias voltage of 10 V is sufficient to get accurate beam shape data, further increase of the bias voltage only leads to an increased signal, without changing the shape of the signal very much (Figure 4.10). The second set of wires is affected by the secondaries from the first set and therefore behaves differently (Figure 4.11). Here a higher bias voltage is required to prevent the secondaries from the first set to hit the wires of the second set and thus obscure the beam shape. A voltage of 200 V removes most of the beam shape distortion and is practicable in terms of the voltage capability of the PCB design. As the insulation

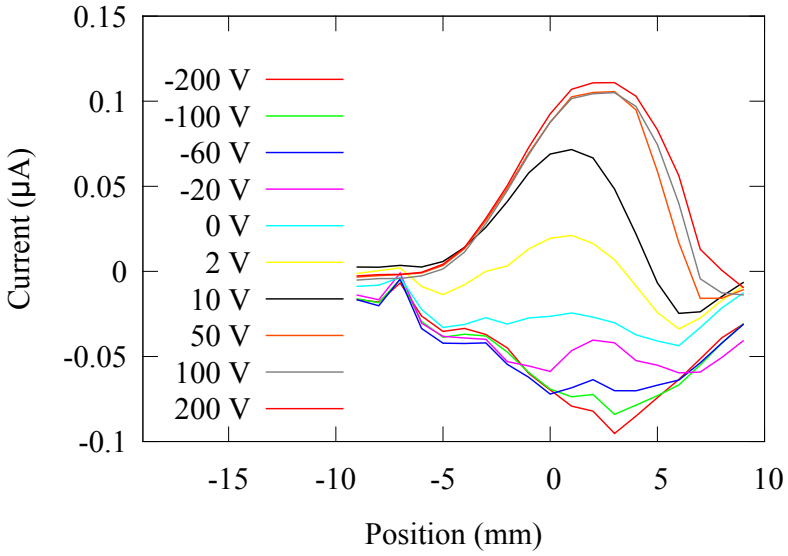

Fig. 4.11: Horizontal beam profile measurements (i.e. from vertical wires, these wires are behind the horizontal wires) at different bias voltages. Each line in this diagram corresponds to a beam profile measurement at a given bias voltage. The lines are piecewise linear interpolations between the current measurements taken by the individual wires to guide the eye. The centre of the beam shape moves by about 1 mm between bias voltage values 10 V and 100 V. This is due to the secondary impact being stronger on the right side of the profile. This effect is likely to be caused by secondaries coming from the first set of wires and thus a much stronger bias field is required to suppress this effect.

between the wires and the surrounding electrode is somewhat delicate, we did not experiment with higher voltages.

4.3 Dipole Magnet for Energy Measurement

For purposes of mass or energy analysis we borrowed a dipole magnet from one of the other groups at RAL. The magnet has relatively small dimensions and was designed to be used inside a vacuum chamber. I measured the fields on axis as well as the Hysteresis (see Figures 4.12 and 4.13) using a hand held Gauss Meter. The magnet creates a field strength on axis in the centre of the yoke of about 10 mT per A. The integral $B \cdot dl$ is about 0.0011 T m A^{-1}. This makes the magnet strong enough to both deflect beams coming out of the ion source and accelerated beams coming out of the accelerator

prototype. The hysteresis of the magnet is relatively small and not significant for low accuracy experiments.

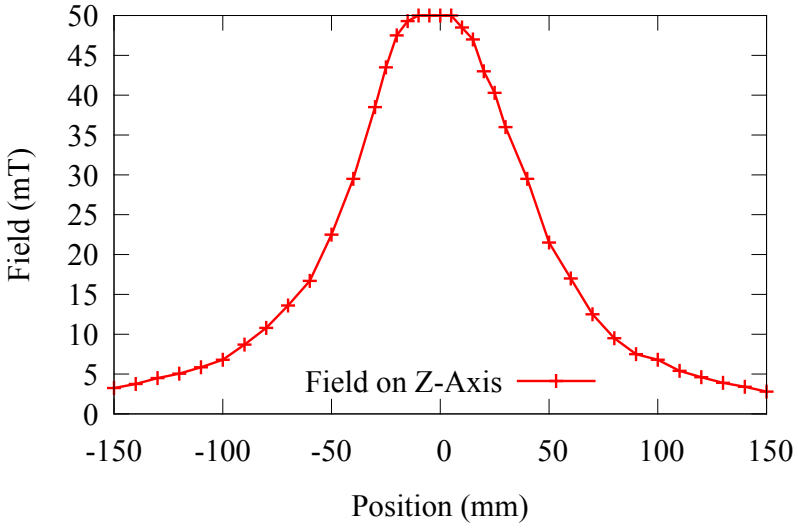

Fig. 4.12: The magnetic field along the z-axis at a current of 5 A. 0 on this scale is in the very centre of the magnet poles. The lines are piecewise linear interpolations to guide the eye.

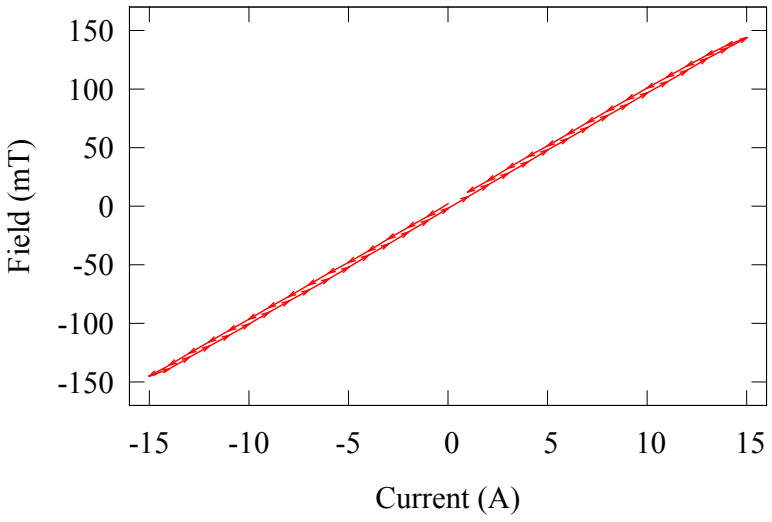

Fig. 4.13: The magnetic field in the centre of the yoke of the dipole magnet in relation to the current flowing through the coil. The current was increased from 0 to -15, then decreased to 0, then increased in reverse direction to +15 and then decreased back to zero. The lines are piecewise linear interpolations to guide the eye.

4.4 Ion Source Commissioning and Characterisation

A number of experiments on the ion source have been carried out in order to analyse how beam current and beam quality depend on the different settings of the source and to find a set of suitable settings for experiments with the accelerator. For this purpose the voltage multiplier has been removed from its position subsequent to the ion source and the various diagnostics described in earlier sections have been placed in front of the ion source.

4.4.1 Beam Current

The first set of experiments focuses on the overall beam current. For this purpose the Faraday Cup described in Section 4.1 has been fitted with a 20 mm aperture and placed at a distance of 6 cm from the ion source.

The first procedure was the variation of the G2 voltage (for details on the ion source settings see Section 2.7 and in particular Figure 2.9) at a fixed G1 voltage of 10 kV. It was found that a ratio of 1:7 is the optimum for G2 and G1 (see Figure 4.14). This has been confirmed at lower and higher values of G1 later on.

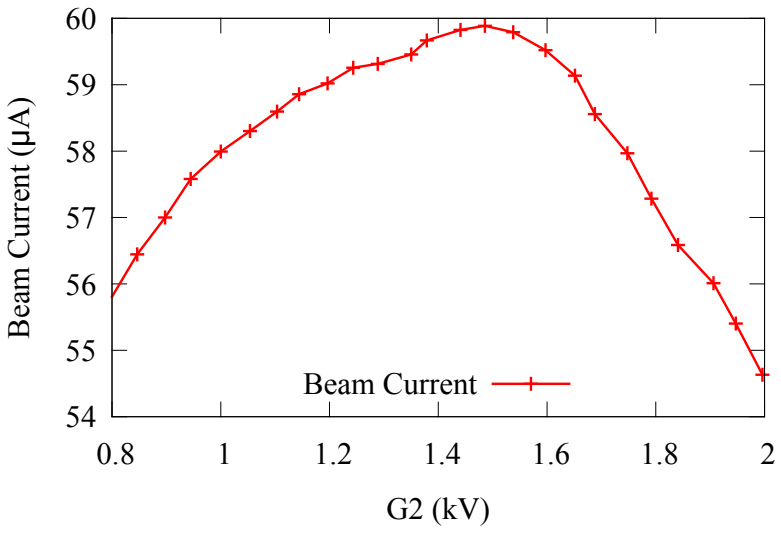

Fig. 4.14: Dependence of the measured beam current on the G2 voltage value at fixed G1 of 10 kV. The lines are piecewise linear interpolations to guide the eye.

The next analysed parameter is the hydrogen gas flow (see Figure 4.15). The extracted current has a maximum at a gas flow of 6 SCCM (Standard Cubic Centimeters per Minute). This corresponds to the fact that for every volume ion source there is an optimum pressure at which the H^- density has a maximum. According to [71] this pressure increases with the discharge current and voltage. However, in our test setup it was determined only for one current value because it was not possible to investigate the behaviour at gas flow values higher than 6.5 SCCM, as the load on the turbo pumps of the vacuum system reached a critical value there. For the same reason the system is unlikely to be operated at the optimum value and will rather be operated at 4 SCCM, where the load on the pumps is manageable. A possible future improvement on the ion source would be an enhanced pumping system that would allow to run the source at the optimum gas flow, e.g. employing two stages of turbo pumps.

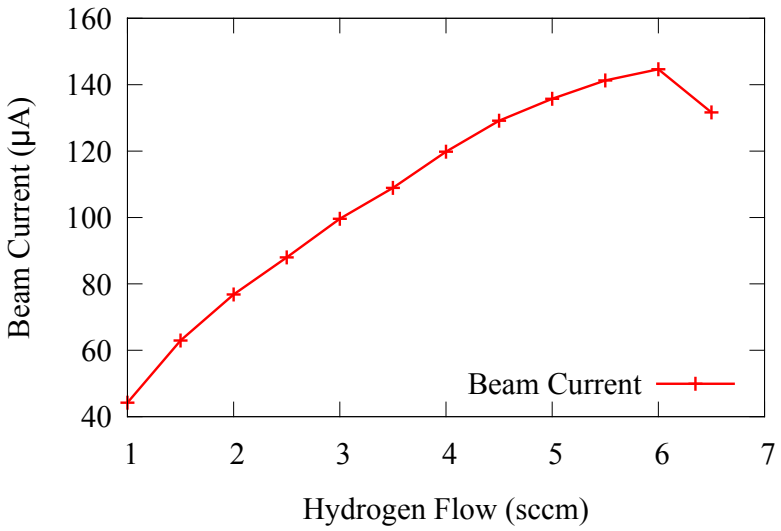

Fig. 4.15: Dependence of the beam current on the hydrogen gas flow (standard cubic centimeters per minute) at a plasma discharge current of 1.23 A. The lines are piecewise linear interpolations to guide the eye.

The next parameter is the bias voltage of the first electrode on the extraction side (plasma electrode). This bias has various affects on transport processes in the extraction region and has to be considered together with the magnetic filter field at

the extraction. According to [55], both the extraction filter field and the plasma bias voltage can be optimised to enhance H^- transport and extraction. However this also effects the transport processes of the electrons. Often a positive plasma bias voltage has been used to reduce electron extraction, but this did not always have a positive impact on the extracted H^- current (e.g. [72]). For our source it was found that the beam current has its maximum at 1.5 V plasma bias voltage. At the same time the G2 current (equivalent to extracted electrons) goes down by approximately 50% and the bias supply current increases rapidly (see Figure 4.16). The plasma bias voltage reducing the extracted electrons and optimising H^- extraction at the same time is a very beneficial feature that has been observed at other ion sources before (e.g. the ECR driven volume source in [73]).

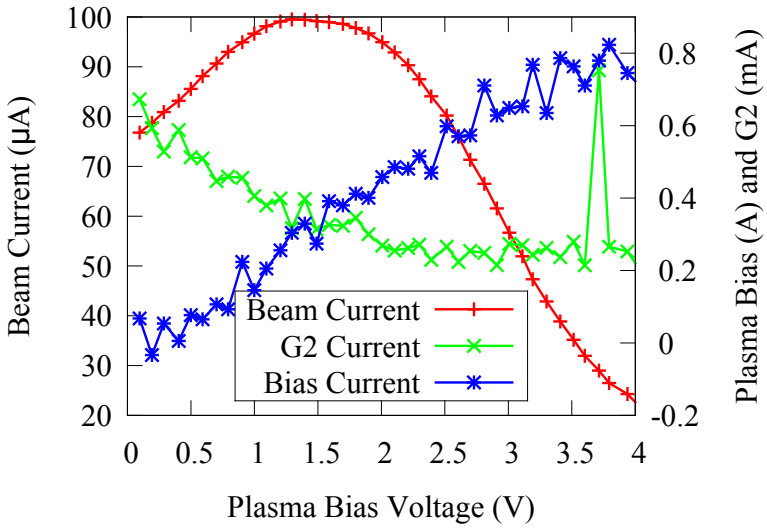

Fig. 4.16: Dependence of the beam current, the plasma bias supply current and the G2 current on the plasma bias voltage. The lines are piecewise linear interpolations to guide the eye.

The next parameter to look at is the voltage between the filament and the walls of the plasma containment. As this parameter heavily impacts the discharge current, the measurement has been repeated with adjusted filament currents to keep the discharge current constant and another time keeping the power of the discharge constant, as

the discharge power is the chief source of heating the system and therefore one of the limits to the overall performance of the source. It has been found that the optimum Arc voltage is 70 V (see Figure 4.17).

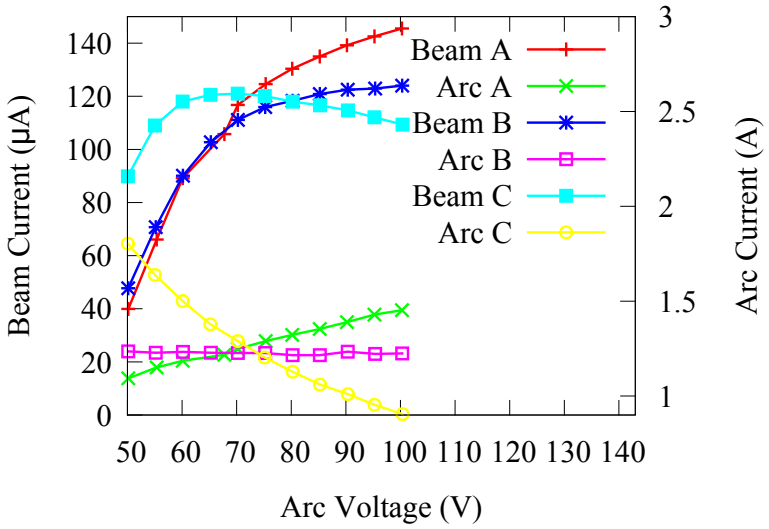

Fig. 4.17: Dependence of the beam current of the Arc voltage. For trial A only the Arc voltage has been modified, and thus the Arc current changed. For trial B the Arc current has been kept constant. For trial C the Arc power has been kept constant. The lines are piecewise linear interpolations to guide the eye.

The next parameter is the G1 voltage. The higher G1, the higher the electric field which pulls ions out of the source at a given G1/G2 ratio. It has been found that the beam current increases monotonically with G1 (see Figure 4.18). This behaviour can not be explained by the space charge limits of the Child-Langmuir law ([1]), as 250 V would be sufficient to overcome the space charge limitation for the extracted current densities of approximately 0.002 mA/mm^2 with the given distance of about 1 cm. However, the H^- production processes in the source should not depend on the extraction voltage and similar behaviour is usually not observed in high power H^- sources or results in bad optics ([55]). Further tests on this have shown however that increasing the extraction voltage does not affect the beam quality and therefore the effect appears different to the one described by Marthe Bacal in [55]. A very likely explanation for the effect would be an enhanced drift of H^- in the plasma by the

fields near the extraction aperture. The relation between the actual plasma discharge

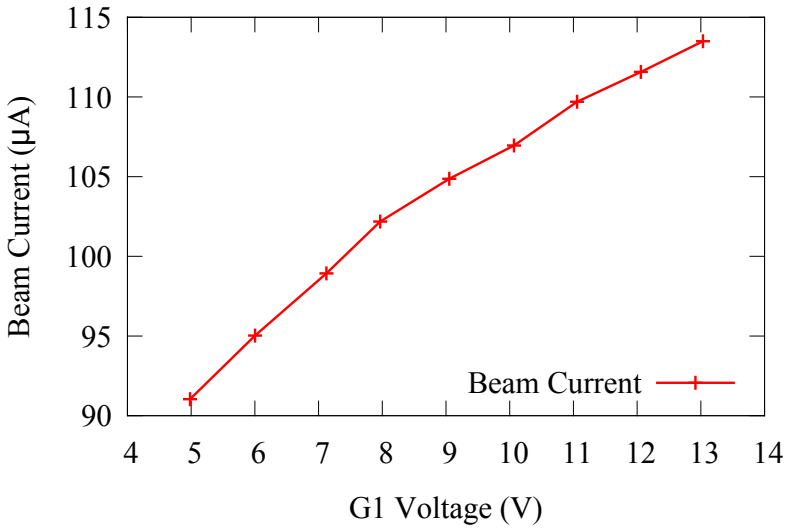

Fig. 4.18: Dependence of the beam current on G1. For every G1 value G2 has been adapted to the optimum value of G1/7. The lines are piecewise linear interpolations to guide the eye.

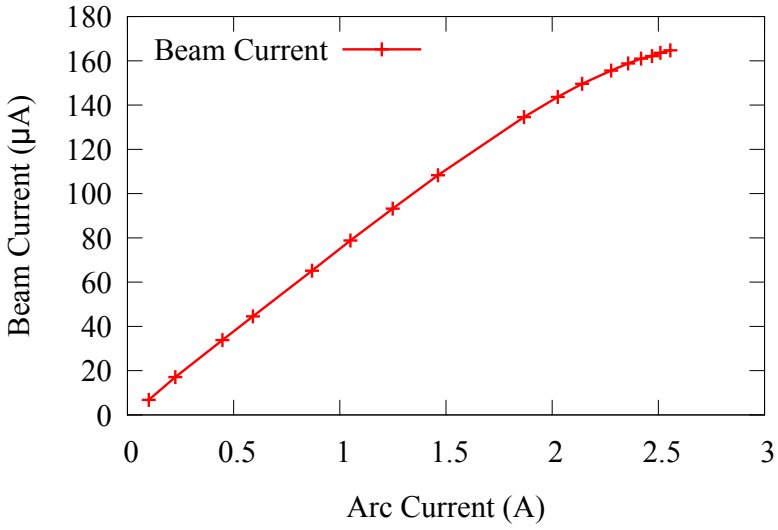

Fig. 4.19: Dependence of the beam current on the plasma discharge current. The lines are piecewise linear interpolations to guide the eye.

current and the beam current was determined by varying the filament current (see Figure 4.19). It starts off linear and then shows a saturation which starts at about 2 A. However, this characteristic also depends on the gas flow. The presented measurement was taken at a gas flow of 2 SCCM and the observed saturation effect has been lower at higher gas flows. The peak value of 160 μA is not the limit of the ion source, at higher

gas flows I extracted beams of 300 μA at a plasma power of about 300 W. Given the 8 mm extraction electrode and the inner surface of the source body one can calculate the ion source efficiency ψ, which is defined by:

$$\psi = j_- \cdot \frac{A}{P} \tag{4.15}$$

j_-: extracted H^- current density
P: arc power
A: chamber surface area

Which in our case is about 2mA/W. Within experimental errors this is roughly the same value as for the commercially available d-PACE ion source developed at TRIUMF (see [74]), and therefore a satisfying result.

4.4.2 Beam Profile and Divergence

In order to examine the beam profile the wire grid described in Section 4.2 has been placed in front of the ion source and measurements have been carried out to determine the beam profile and the influence of the ion source parameters on the beam profile. Also measurements at two different distances from the source have been performed in order to get insights about the divergence of the beam.

The signals have been fitted with both the Bennett and the Gaussian profile. In most cases neither of the two fits seemed to match the measured beam profile much better than the other one. Depending on the ion source settings there were a few cases where either of the two profiles definitely fitted better. However these measurements were inconclusive and unfortunately would require more detailed attention which would be beyond the scope of this thesis. It is not essential for the acceleration experiments to have a very accurate model of the beam shape. The beam shape does not play a key role in the isotope production process in a target either.

Plasma Bias Voltage In a first experiment the plasma bias voltage was varied to observe the effect on the beam shape (see Figure 4.20 and Figure 4.21). In accordance with the Faraday Cup measurements in the previous section, the plasma bias voltage did influence the overall beam current. It did however not change the beam shape. This makes sense as the plasma bias voltage is believed to increase the H^- density in the extraction region but not change the plasma temperature or density and thus leave the extraction meniscus unaffected. The optimum voltage is about 1.4 V which is in good agreement with the measurement of Figure 4.16.

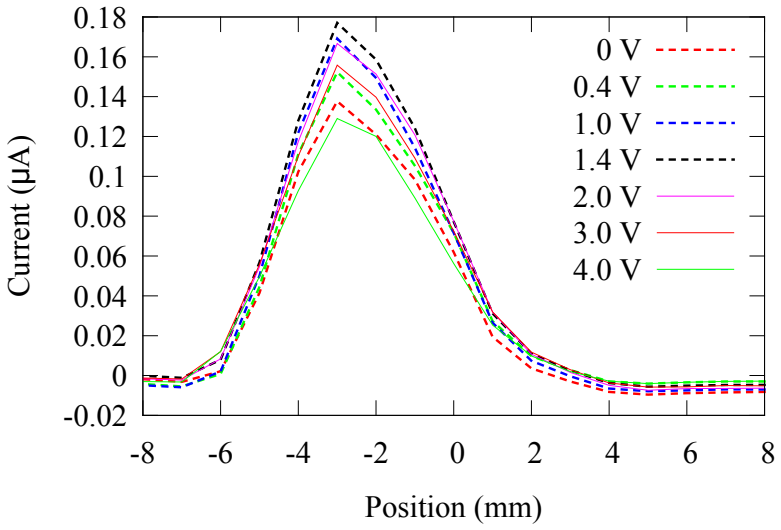

Fig. 4.20: Influence of the plasma bias voltage on the vertical beam profile. As expected it mainly affects the beam current, but not the beam shape. The lines are piecewise linear interpolations to guide the eye.

Gas Flow I conducted a series of measurements where I varied the hydrogen gas flow going into the ion source plasma chamber. As expected, the gas flow hugely impacts the amount of extracted H^- current. However, as can be seen in Figure 4.22, it does not affect either the beam width or the beam shape very much.

G2 Voltage As expected, the G2 Voltage has a very strong influence on the beam shape. Figure 4.23 displays how the G2 voltage defines the beam profile measured at

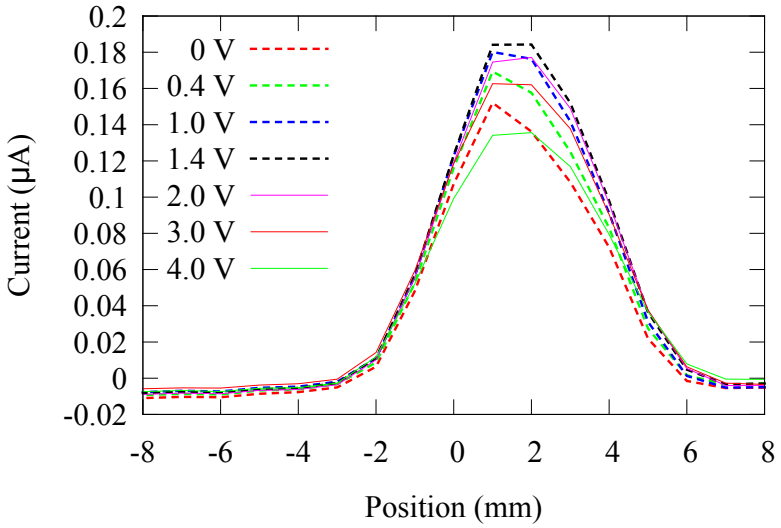

Fig. 4.21: Influence of the plasma bias voltage on the horizontal beam profile. As expected it mainly affects the beam current, but not the beam shape. The lines are piecewise linear interpolations to guide the eye.

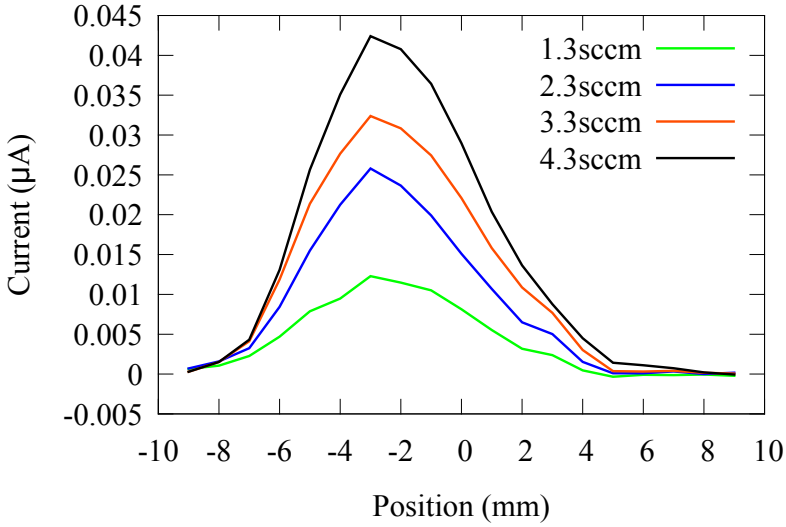

Fig. 4.22: The beam profile at different gas flows. The gas flow hugely influences the extracted currents, however it does not affect the beam shape. The lines are piecewise linear interpolations to guide the eye.

a distance of 73 mm from the extraction of the ion source. At low G2 values the beam is very wide and looks like a gaussian with the top cut off. At higher G2 values it becomes more gaussian shaped with the best focus reached at 1.1 kV with a 3σ beam width of ≈5 mm.

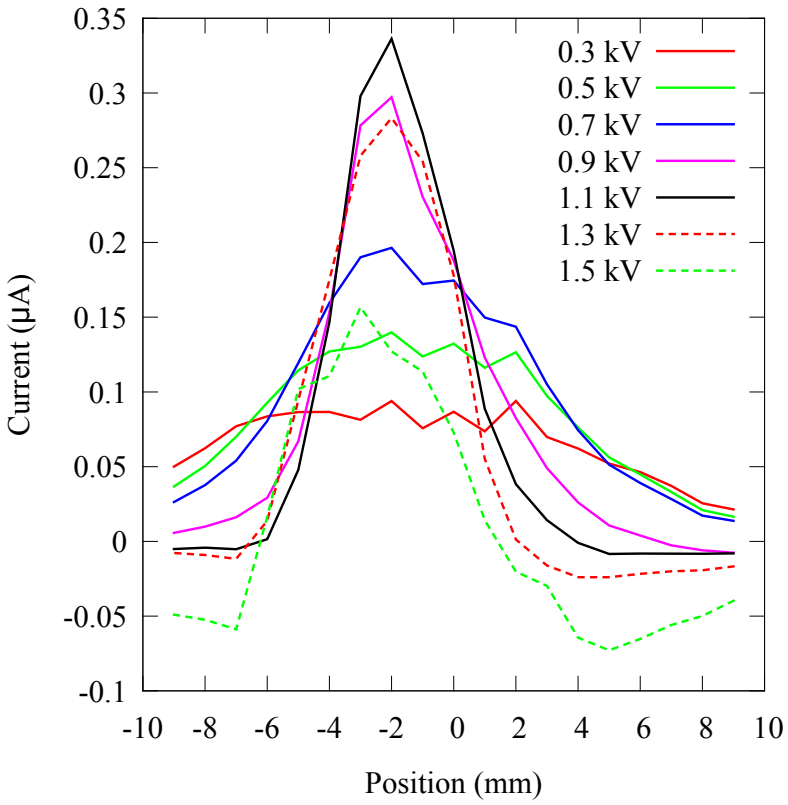

Fig. 4.23: The vertical beam shape at 73 mm distance from the source at 1 A discharge current for various G2 values. The optimum G2 value is 1.1 kV (see also Figure 4.24). Note how the beam shape changes for higher G2 values. The lines are piecewise linear interpolations to guide the eye.

Discharge Current The discharge current does have a strong influence on the plasma temperature in the first section of the ion source. However due to the magnetic filter we would expect it not to have a direct impact on the plasma in the extraction region or on the extraction meniscus. I have performed an analysis of the beam shape and the focusing for various discharge currents to investigate this (see Figure 4.24). The beam width does not strongly vary with the discharge current and neither does the optimum G2 voltage which is at 1.1 kV. This suggests that the meniscus shape is

rather unaffected by the discharge current. Only for extremely low discharge currents the optimum G2 voltage is somewhat smaller (1.0 kV).

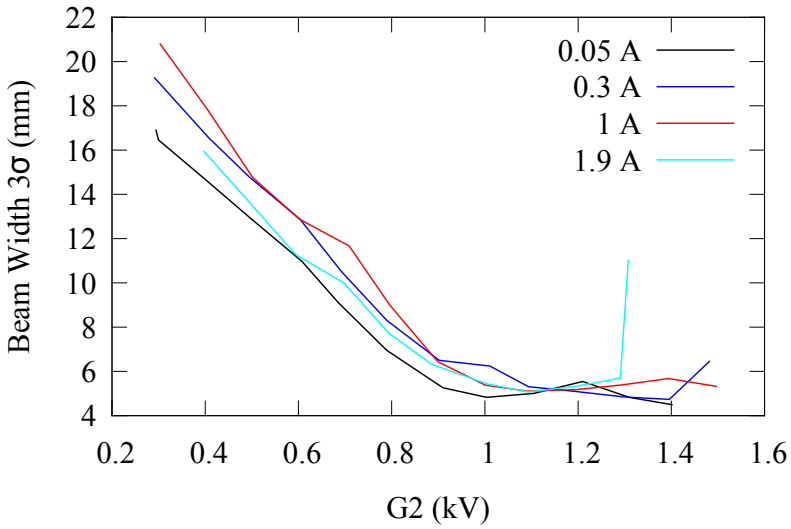

Fig. 4.24: The beam width measured with a gaussian fit taking 3σ at 73 mm distance from the source for different discharge currents. The discharge current does not have an influence on the beam shape. The optimum G2 value is 1.1 kV. Only for the very low discharge of 0.05 A the optimum G2 voltage is somewhat lower, i.e. 1 kV. Note that the plotted width from 1.2 kV upwards are slightly misleading as the beam shape started strongly deviating from the gaussian shape (see Figure 4.23), resulting in the fit method not being ideal for these values. The lines are piecewise linear interpolations to guide the eye.

Beam Divergence The beam divergence is an important property to consider for the injection of the H^- beam into the prototype accelerator. As established by the other measurements, the G2 voltage is the main factor influencing the shape and width of the beam and thus its divergence as well. I performed beam width measurements at two different distances (73 mm and 148 mm) from the ion source for various G2 values and compared them (see Figure 4.25). For the optimum focus value of about 1.1 kV at 73 mm the beam has a width of ≈ 5 mm. At the distance of 148 mm this width has increased to about twice that value, i.e. the beam is quite divergent as it was going through a waist at 73 mm. For slightly higher G2 values however the beam width at 148 mm decreases to reach a minimum value of ≈ 7 mm for 1.4 kV. At this G2 voltage

the beam width at 73 mm has increased quite a bit to about 6.5 mm. This suggests an almost parallel beam which is only slightly divergent. It may seem counterintuitive that the beam should be less focussed for the higher G2 value of 1.4 kV (i.e. parallel instead of having a waist at 73 mm) than for the G2 voltage of 1.1 kV. It is to be noted that the G1 voltage in all these experiments has been kept constant at 10 kV, so that a change in G2 voltage affects both focussing elements in the ion source extractor at the same time (see Section 5.1.1 for simulation results of this effect).

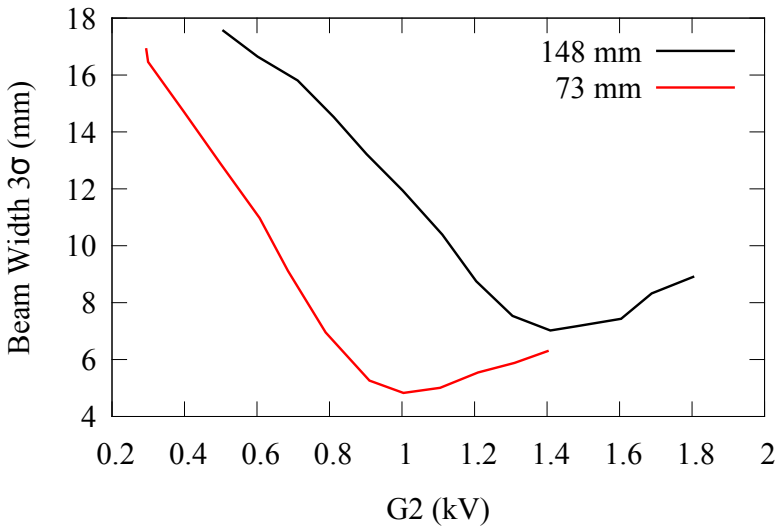

Fig. 4.25: The gaussian beam width 3σ in relation to G2 at 148 mm and 73 mm distance from the ion source at a discharge current of about 0.1 A. At 1.4 kV the beam is almost parallel with a width just below the ion source aperture diameter of 8 mm. Due to breakdown problems in the ion source, no data was taken for G2 larger than 1.4 kV at the close position. The lines are piecewise linear interpolations to guide the eye.

4.4.3 Particle Species

I installed the previously mentioned dipole magnet between the ion source and the wire grid (see Figure 4.26) in order to deflect the H^- beam to validate its energy and also investigate the presence of H^0 in the beam. As calculated from the geometry and the magnetic field distribution, the main H^- portion of the beam should get deflected on the wire grid by approximately 0.5 mm per mT magnetic field in the centre of the dipole

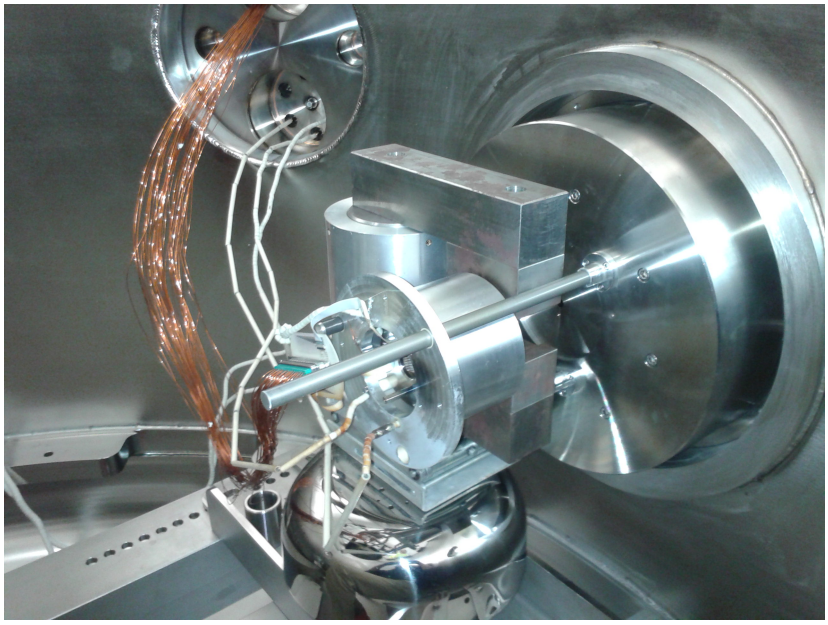

Fig. 4.26: The setup with the dipole magnet between the ion source and the wire grid. The beam deflection of the dipole can be tracked on the grid.

yoke or respectively 5 mm per A current through the coils of the magnet. Figure 4.27 shows a plot of the measured beam profile at different dipole strengths. One can clearly see how the main H^- portion of the beam gets deflected and how a second portion of the beam remains, which is deflected much less. This can only be a particle fraction of either higher mass or higher energy or less charge. Less charge would mean a neutral particle such as H^0, however this would not be deflected at all. Higher energy is not possible as the maximum energy in the source is 10 keV. It must therefore be a particle with higher mass. According to [75] the main other type of negative ion that has been extracted from similar ion sources is OH^-, which is due to residual water in the ion source. As Figure 4.28 shows, the observed fraction of the beam is deflected four times less than the H^-, thus having an approximately sixteen times higher mass, as would be the case with OH^-. It is thus very likely that the observed portion of the beam consists of OH^-. According to [75] the portion of OH^- in a beam can be reduced to below 1 % by performing a very good bakeout or extended running of the source as this removes residual water. A few experiments have been done to analyse how the

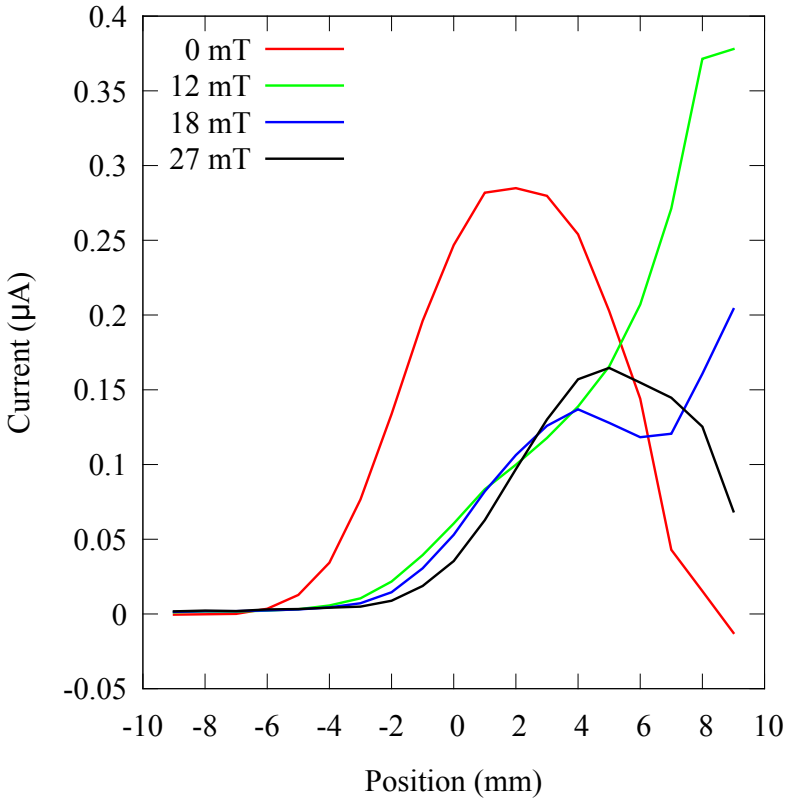

Fig. 4.27: The beam shape for different field strengths in the dipole magnet (see Figure 4.26). Note that the grid overamplifies the beam when it comes to the very edge of the grid, thus the enhancement of the profile at 12 mT. One can clearly see that there is a second particle fraction besides the H^-. The lines are piecewise linear interpolations to guide the eye.

discharge current and gas flow influence the OH^- fraction of the beam. Figure 4.29 shows the beam fractions for two different discharge currents. The OH^- portion of the beam decreases slightly with higher discharge currents. An increase of the gas flow (see Figure 4.30) increases the portion of OH^- in the beam. This might point to water contamination coming from the gas pipe and a bakeout of the gas pipe might be considered. Note that these measurements are not quantitative. As discussed above, the OH^- portion might not scale 1:1 with the H^-. The potentially different secondary emission coefficients γ of the two particle types are illustrated by the different reaction of the signal to the bias voltage, see Figure 4.31. A more detailed investigation of these effects is beyond the scope of this thesis. Generally the OH^- fraction of the beam should be kept as low as possible, the ion source should therefore be run in a bakeout

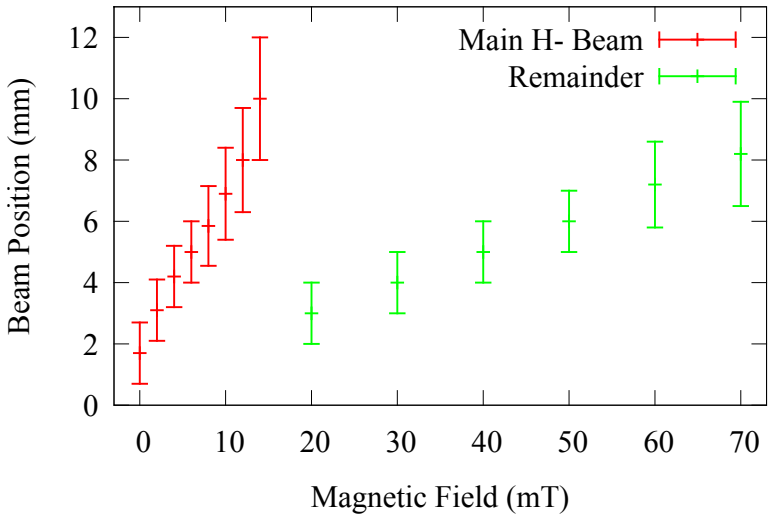

Fig. 4.28: Beam position in relation to magnetic field strength in the dipole. The beam position was estimated from measurements similar to those in Figure 4.27 by looking for a local maximum in the beam current distribution. The main beam (red) is off the grid at about 20 mT, when the remainder (green) becomes visible. The main beam moves by $\approx$500 µm mT^{-1} whilst the remainder moves by $\approx$125 µm mT^{-1}. This supports the hypothesis of the remainder being OH^- and thus having $\approx$16 times higher mass.

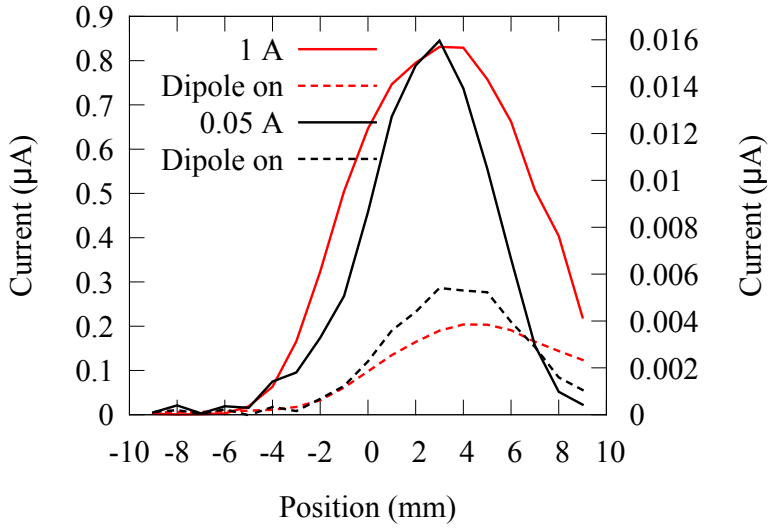

Fig. 4.29: Beam profiles at 1.3 SCCM gas flow for two different discharge currents. The signal remaining after switching the dipole on at 22 mT is not H^-. The proportion of byproducts decreases with increased discharge current. The lines are piecewise linear interpolations to guide the eye.

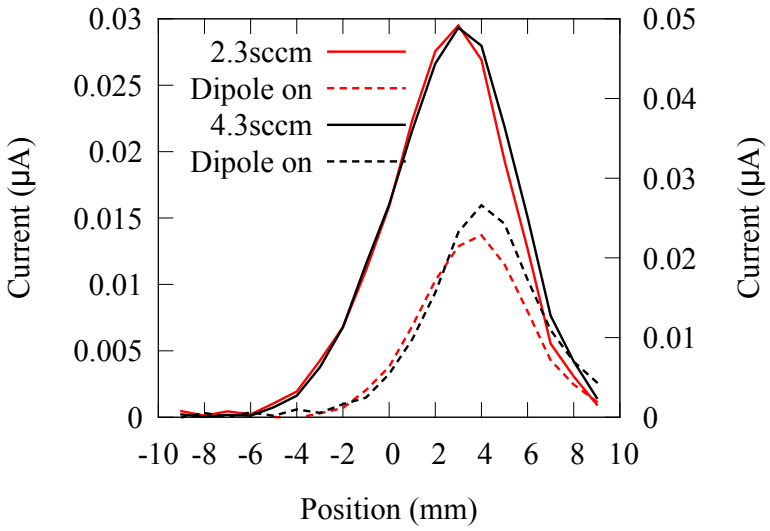

Fig. 4.30: Beam profiles at two different gas flows. The signal remaining after switching the dipole on at 22 mT is not H^-. The proportion of byproducts increases with increased gas flow. The lines are piecewise linear interpolations to guide the eye.

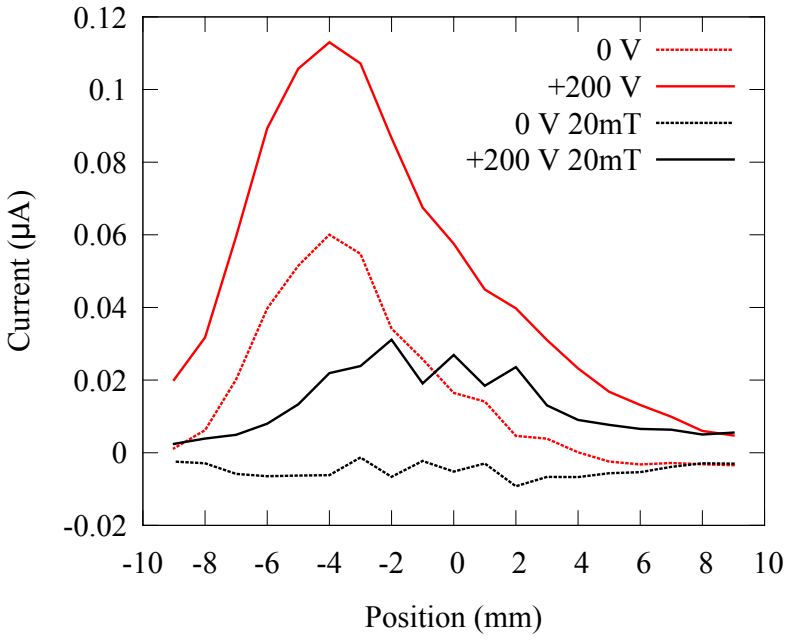

Fig. 4.31: The beam profile with and without the wire grid bias voltage (red plot). The same measurement with a magnetic dipole field of 20 mT (black plot). The signal in the black plot should not contain any H^- as this is deflected by the magnetic field, the remaining signal is most likely due to OH^-. The lines are piecewise linear interpolations to guide the eye.

regime and the gas pipe should be investigated. Note that the ion source had been vented for an extended time before these experiments, which explains the non-ideal state in terms of contamination with water. The fact that the beam can be completely deflected proves that there are no substantial portions of H^0 in the beam.

5. BEAM TRANSPORT AND ACCELERATION

5.1 Simulation of Beam Transport

I have carried out a series of systematic simulations in order to understand the beam transport inside the ion source as well as in the accelerator formed by the shells. I first set up a simulation model in the VORPAL code ([76], now VSim) by the commercial code supplier Tech-X. However after some work I realised that it was not the most suited code for the task. I therefore developed a new model in Vector Fields Opera by the commercial supplier Cobham ([77]). Opera is an interactive tool with a user interface. However it seemed more suitable to set up a fully parameterised model which could then be run via batch processing to systematically investigate the impact of essential parameters. The following sections present the findings of the simulation studies.

5.1.1 Ion source extraction

The extraction processes in negative ion sources are fairly complex. The beam is not emitted from a fixed surface, but rather from a whole region within the plasma boundary, which may move according to space charge and electric fields (see [78]). For our ion source, which has a relatively low plasma density and low beam currents, space charge does not play a major role. One can therefore assume a concave shaped relatively stable plasma meniscus. For my simulations I have assumed a meniscus radius of $\approx$40 mm.

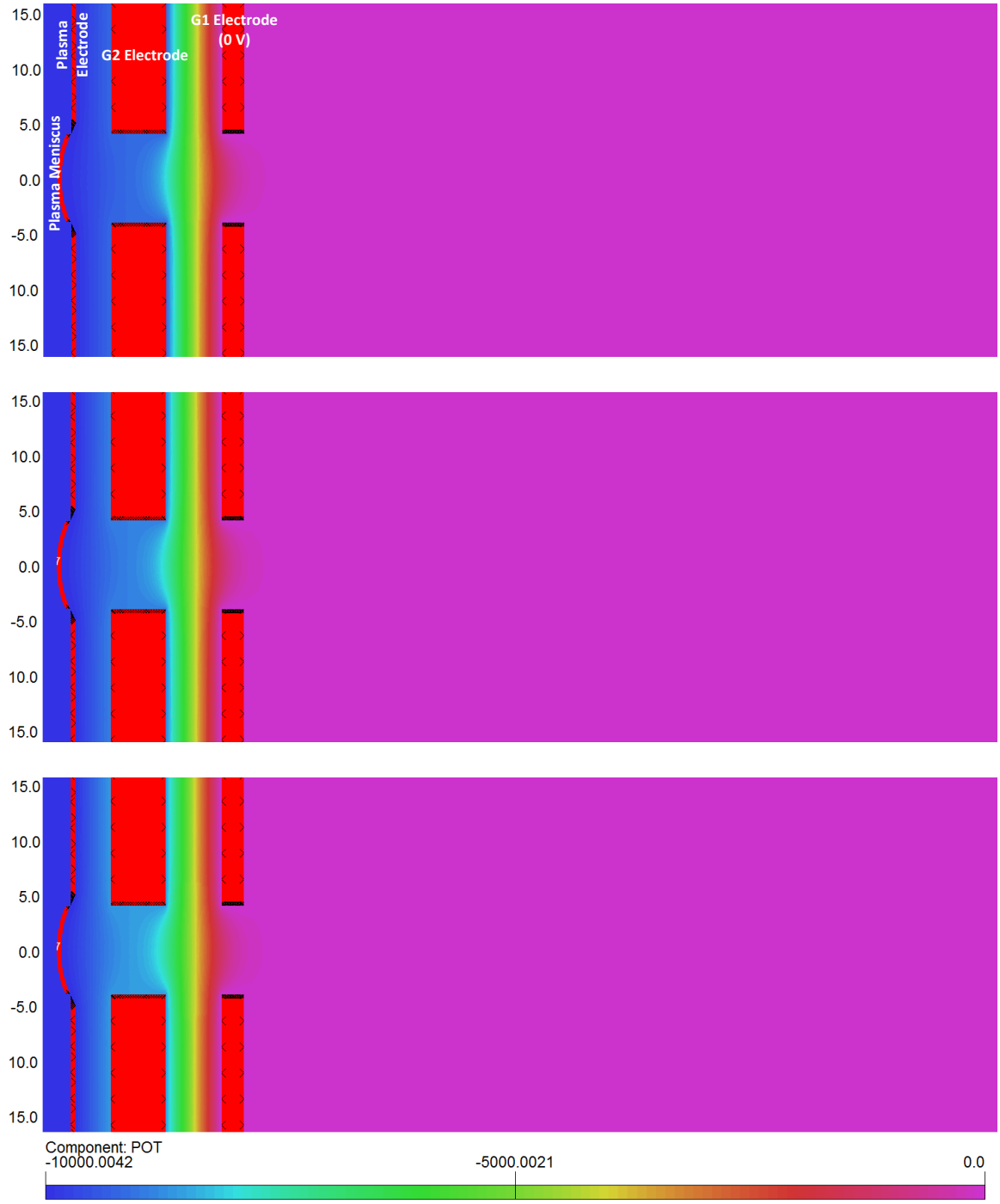

Fig. 5.1: The electric potential in the ion source extraction system at a G1 of 10 kV for varied G2 values. The ion source plasma is the very left part of the image (blue). It touches the plasma electrode (flat red electrode). The plasma meniscus is modelled as a circular arc in red. To the right of the plasma electrode are the G2 and the G1 electrode. On the right of the G1 electrode is a free vacuum space (pink) where the diagnostics can measure the beam or where it could be injected into the accelerator. The colour scale for the potential ranges from −10 000 V (blue) to 0 V (pink). The y-scale is in mm. At G2 of 0.8 kV (top) the second gap has a very strong focus. At 1.1 kV (middle) and 1.4 kV (bottom) the focus of the first gap gets stronger and the second gap focus weakens. See Figure 5.2 for the effects on the beam.

The main parameters for the beam formation in the ion source extraction section are the voltages G1 and G2. All other ion source parameters do affect the H^- density in the ion source plasma, however they do not significantly affect the extraction process itself in terms of the beam profile and divergence. Both gaps in the extraction system, i.e. the one between the plasma electrode and the G2 electrode and the one between the G2 and the G1 electrode, have a strongly focussing effect. For a fixed G1 of 10 kV the overall focussing effect is strongest for low G2 values (see Figure 5.1 for the fields in the extraction region and Figure 5.2 for the beam divergence). This results in overfocussed beams with small width very close to the source and rapid growth of beam width further away from the source. For larger G2 values the beam focus moves away from the source and for ≈1.4 kV the beam is almost parallel. For larger values there is no focus and the beam diverges as it leaves the source. See Section 4.4 for corresponding experimental results.

5.1.2 Acceleration through the shells

As soon as the shells of the accelerator are added to the system, the situation changes because the first gap has a strong focussing effect. The aim of these studies is to predict a good setup which will result in good beam transport in experiments planned for the near future. Figure 5.3 shows the beam with the shells for different G2 values with G1 fixed at 10 kV. Good beam transport is only given for very low values of G2. The system could be operated at a G2 of 0.8 kV, however this is not conducive to the exctraction of maximum H^- currents from the ion source. In order to deliver high H^- currents, the ion source needs a far higher G2 value (see experiments in Section 4.4). A means of weakening the focusing effect in the first shell gap is to increase the aperture size of the first shell (see Figure 5.4 for a comparison of the focussing potentials in

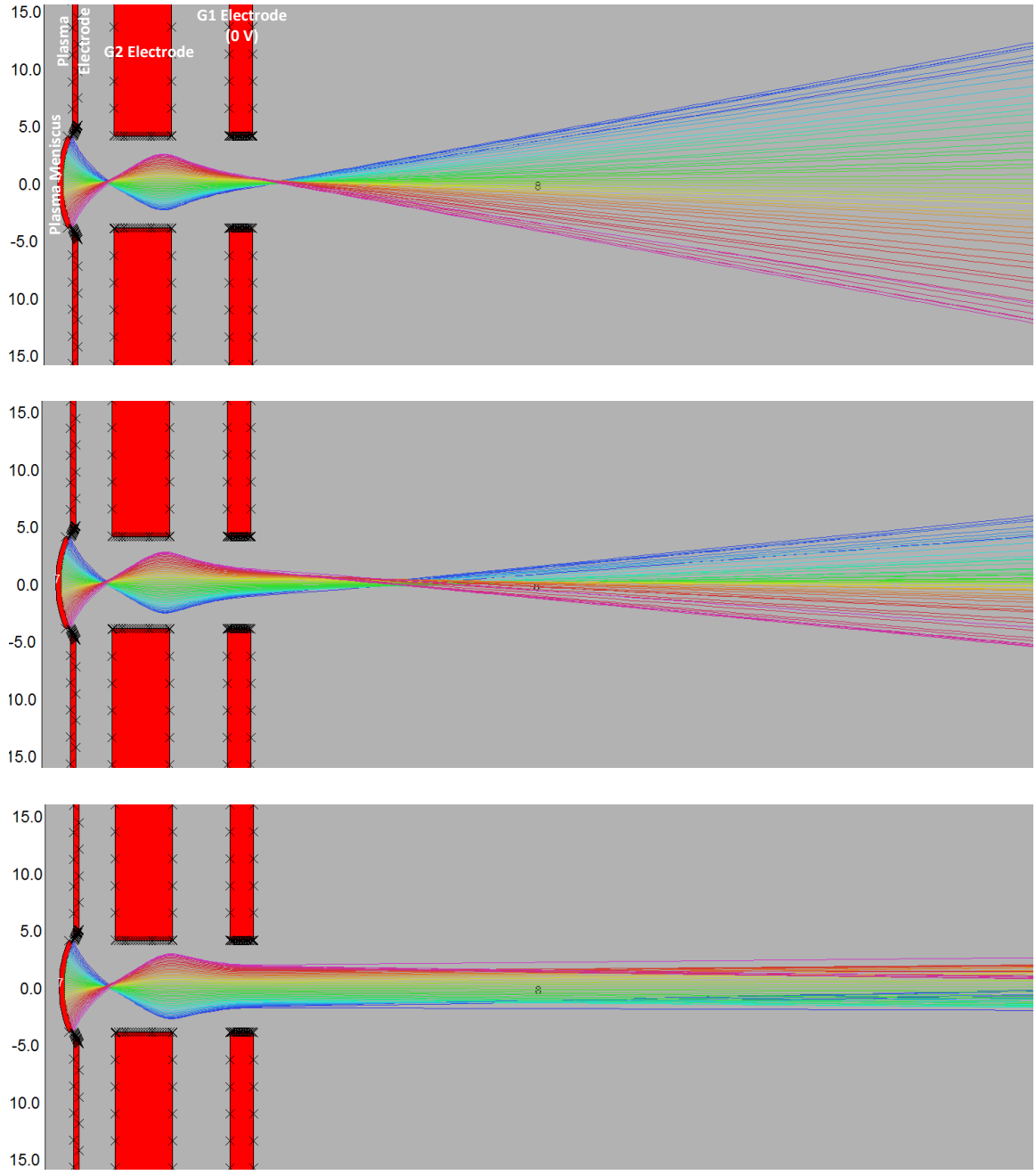

Fig. 5.2: The ion source extraction system with beam at a G1 of 10 kV and varied G2 values. The y-scale is in mm. The coloured rays are the trajectories of H^- ions extracted from the surface of the plasma meniscus. At a G2 of 0.8 kV (top) the beam is overfocussed. At 1.1 kV (middle) it is focussed on a point close to the ion source. At 1.4 kV (bottom) the beam is almost parallel. See Section 4.4 (especially Figure 4.25) for the experimental results which match this simulation.

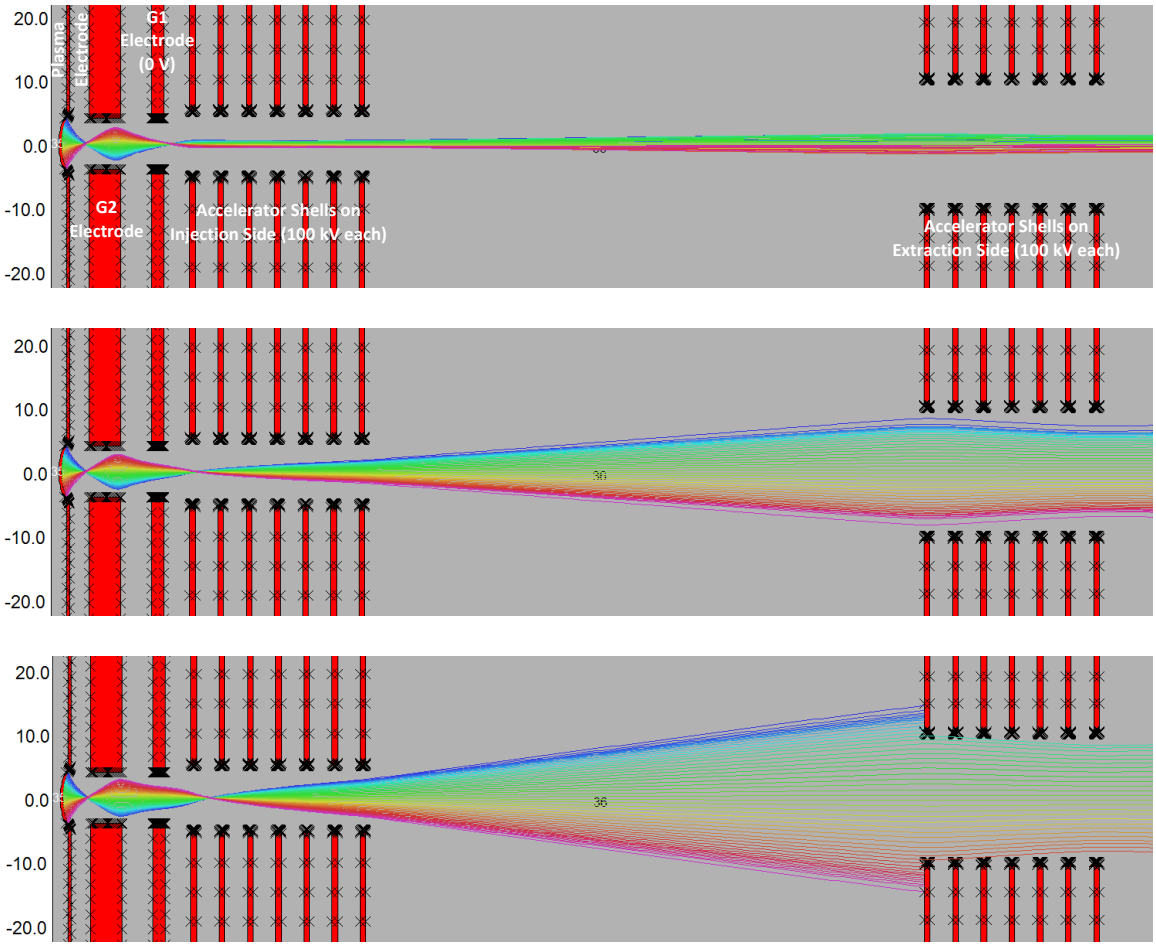

Fig. 5.3: Beam acceleration through the shells at a G1 of 10 kV for different G2 values. The y-scale is in mm. The first three electrodes on the left are part of the ion source, as depicted in previous figures. The subsequent electrodes are part of the electrostatic accelerator formed by the shells, or more particular by a series of holes through the shells (see also Figure 2.2). The hole diameter of the shells is 10 mm on the injection side (left) and 20 mm on the extraction side (right) of the electrostatic accelerator. The coloured rays are the trajectories of H^- ions extracted from the surface of the plasma meniscus. The shell to shell voltage of the accelerator is 100 kV. The first shell on the injection side is at ground potential. The first inter shell gap has a very strong focus, therefore the parallel beam from the ion source (bottom, G2 1.4 kV see also Figure 5.2) gets strongly overfocussed. For lower G2 values (1.1 kV middle, 0.8 kV top) the focus of the first gap converts the divergent beam from the ion source into a more parallel beam.

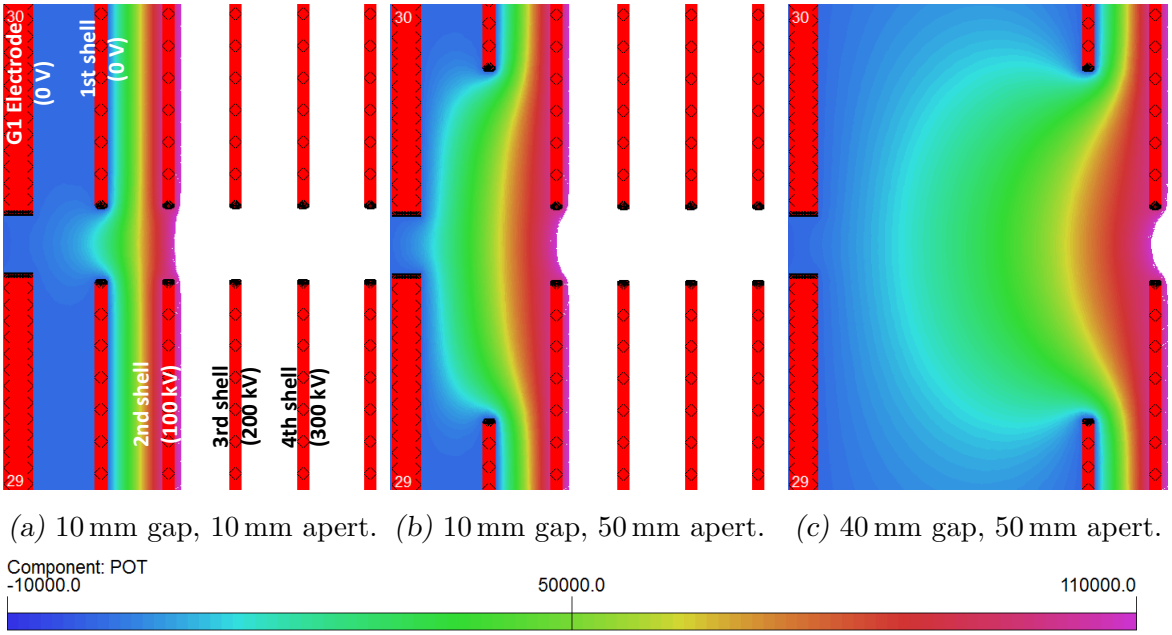

(a) 10 mm gap, 10 mm apert. *(b)* 10 mm gap, 50 mm apert. *(c)* 40 mm gap, 50 mm apert.

Fig. 5.4: The electrostatic potentials in the shell injection region. The colour scale goes from −10 kV (blue) to 110 kV (pink). The white areas have voltages above 110 kV. The first electrode on the left is the G1 electrode, i.e. the last electrode of the ion source as depicted in previous images. All other electrodes are part of the electrostatic accelerator formed by a series of holes in the metallic shells (see also Figure 2.2 for reference). The lens effect on the left is extremely strong, it weakens towards the right. See Figures 5.5 and 5.3 for the effect on the beam.

the shell injection region for different setups) . A further reduction could be achieved by increasing the size of the second aperture. However changing aperture sizes is an irreversible mechanical process and therefore not suitable as the only means of adaptation in experiments. As the voltage per gap in experiments might vary according to the currently reached performance of the 7-shell system, another means of varying the focus of the first gap would be very useful. Varying the width of the gap between the ion source and the first shell is a good way of achieving this. Increasing the gap leads to a weaker focussing. As Figure 5.5 shows, a fairly parallel beam can be achieved at a G2 voltage of 1.4 kV at a shell-to-shell voltage of 100 kV if the gap between ion source and first shell is increased to 40 mm. For lower shell-to-shell voltages the gap could be smaller.

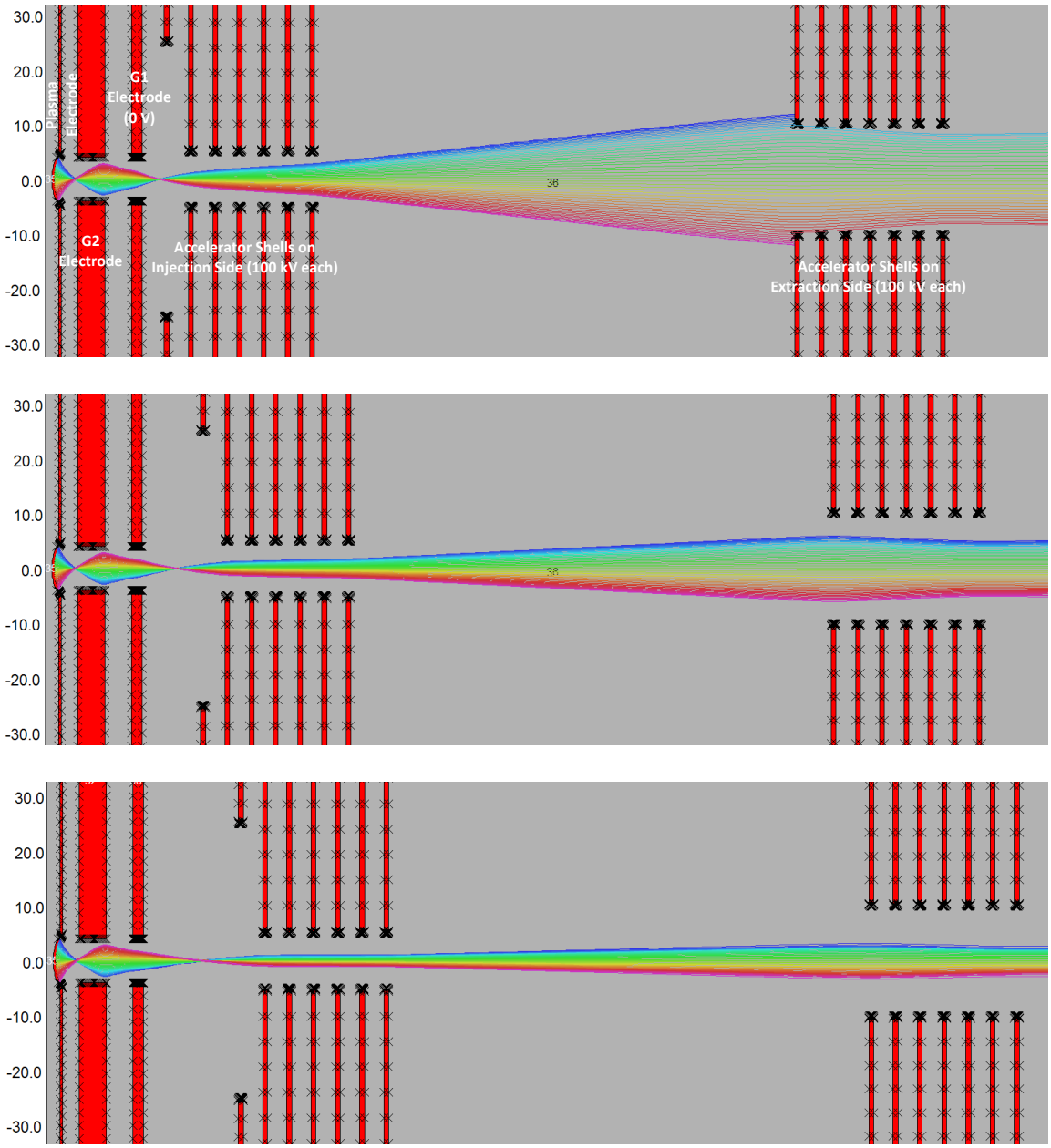

Fig. 5.5: Beam acceleration through the shells with an enlarged first aperture (50 mm diameter) for different gap width between the ion source and the accelerator shells. The hole diameter of the other shells is 10 mm on the injection side (left) and 20 mm on the extraction side (right) of the electrostatic accelerator. The y-scale is in mm. The first three electrodes on the left are part of the ion source, as depicted in previous figures. The ion source voltages are G1 10 kV and G2 1.4 kV. The subsequent electrodes are part of the electrostatic accelerator formed by the shells, or more particular by a series of holes through the shells (see also Figure 2.2). The shell to shell voltage of the accelerator is 100 kV. The first shell on the injection side is at ground potential. The coloured rays are the trajectories of H^- ions extracted from the surface of the plasma meniscus. For the closest gap of 10 mm (top) the beam is strongly overfocussed. For larger gaps (25 mm middle, 40 mm bottom) the beam becomes more parallel. For the potentials in the injection region see Figure 5.4

5.2 Stripper at the Terminal

5.2.1 Requirements for the Stripper

In order to run the novel electrostatic accelerator in tandem mode, a stripper system is required. One might think that this could be provided in a straightforward manner by copying a system used for larger hadron accelerators. However, due to the low energy of the stripped beams in our experiments, the foils have to be far thinner than in larger hadron accelerators and the challenges and requirements are therefore very different. I have therefore undertaken a substantial amount of literature research and I have dedicated this entire section to the development of a suitable stripper system.

The final machine setup will have 50 shells and voltages of up to 100 kV per shell. That results in maximum energies of a few MeV/q of ions to be stripped in the centre of the accelerator. The machine is required to run with H^- ions with a goal of 100 µA extracted proton current. The beam diameter in the stripping area of the accelerator is in the range of ≈7 mm. The 7-shell prototype system involves a beam energy of ≈500 keV. This has to be taken into account for the considerations on appropriate stripping systems. A different stripper foil will be used for the 7-shell system than would be required for a full-scale 10 MeV system. As the stripping system will be placed inside the centre of the accelerator, the installation, maintenance and replacement of it is complicated and time consuming. The vacuum has to be broken, and the shells have to be dismounted. Therefore the stripping system should be able to stay functional for a long period of hundreds of hours of beam operation. Further criteria are:

- Reliability and durability
- Stripping efficiency

- Energy loss
- Scattering
- Cost

Besides very recent elaborate stripping methods like laser stripping, which works without beam-matter interaction ([79]), gas stripping and foil stripping have been the two main approaches for decades. Gas stripping requires differential pumping and a mechanism to control the gas pressure in the stripping area. Both of these are very difficult to realise with the geometry of the accelerator. I have therefore decided to design a foil stripping system.

5.2.2 Foil Materials

Foil stripping is the most common approach for charge stripping in today's accelerators. The working principle is quite simple: A thin solid foil is placed in the beamline so that the beam traverses the foil. During traversing the foil the charged beam particles interact with the matter of the foil. There are various types of interactions which lead to energy loss, scattering and ionisation of the beam particles. At the same time they cause structure damages, heating and evaporation of the foil. The ionisation of the beam particles is the desired effect, all other effects are side-effects which are to be minimised. The damages to the foil do not only lead to foil rupture at the end of its lifetime, they also cause a severe degradation of the foil's stripping efficiency over its lifetime ([80]). The properties of a stripper foil are defined by several parameters. These are the material itself, its thickness and the assembly of the foil. The most common element for stripper foils is carbon and there seems to be no alternative in terms of durability of these foils. However there are various types of manufacturing methods for carbon foils which result in different physical structures. These differ

significantly in their properties, especially in their durability, which is a main concern for accelerator reliability. Therefore the production process of the foil itself is the key variable for the lifetime of the foil ([81]). In some cases slight variations in the production process may result in significant changes of the lifetime ([80]). The results in terms of lifetime are better known than the specific variations in the microscopic structure. Generally it turns out that an appropriate pre-heating process of the foils enhances their lifetimes ([80]). For the use of metals in stripper foils the process of erosion of the foil by the beam has to be taken into account. The material released by the eroding foil will deposit inside the accelerator, possibly on insulators what might cause serious problems like breakdowns or sparks ([82]).

Arc evaporated Carbon (standard) Arc evaporated carbon foils are the standard material for strippers and are commercially available at reasonable rates of 20-200 $ per foil depending on their thickness ([83]). Usually all other foil types are compared to these standard foils in terms of handling and durability. They are available with densities from less than 1 µg cm^{-2} up to more than 1000 µg cm^{-2}. They have been used for decades in cyclotrons all around the world and therefore a large amount of expertise and data is available in the scientific community ([84]).

Polycrystalline Graphite (PCG) Polycrystalline graphite foils are composed of graphite microcrystals with a grain size of the order of 1 µm ([84]). Therefore polycrystalline graphite is not appropriate for very thin foils as desired for the accelerator prototype. It is rather used for thicker foils with densities larger than 400 µg cm^{-2} (i.e. more than 2 µm thickness). For these thicknesses they have the advantage of easier handling and are cheaper to produce than arc evaporated foils ([84]).

Pyrolytic Graphite The pyrolysis (cracking) of hydrocarbons is a carbon deposition method with a long history ([85]). The resulting foils have good properties as a stripper and have performed better than arc-evaporated foils for example in the experiments of [86]. However, these foils are very labour-intensive to produce and therefore rarely used ([87]).

Diamond Like Carbon (DLC) Diamond Like Carbon Foils are carbon foils containing a nearly isotropic distribution of nanocrystals and a certain fraction of sp^3 bonds ([88]). There are several methods for the production of DLC foils and the resulting microscopic structure ranges "from impure superficially amorphous thin films showing evidence of partial tetrahedral coordination among C atoms, to thin-film and bulk structures showing substantial tetrahedral coordination but no long-range order, to polycrystalline and single-crystal diamond structures with little or no evidence of atomic impurity." ([85]). DLC foils are commercially available from a thickness of $2\,\mu g\,cm^{-2}$ (approximately 10 nm) up to $1000\,\mu g\,cm^{-2}$ (approximately 5 µm) from micromatter ([89]), which is a Canadian company selling foils which were originally produced and developed for TRIUMF. The prices are in a comparable range as those of arc-evaporated carbon foils by ACF metals ([90]). V. Kh. Liechtenstein et al. worked with very thin DLC foils, which were produced at the Kurchatov Institute in Moscow ([86]). They investigated the use for applications in the energy range of 0.1 MeV to 2 MeV. This is interesting as most other publications deal either with cyclotron energies of 15-30 MeV or with synchrotron energies above 200 MeV. Liechtenstein found that 5 $\mu g\,cm^{-2}$ DLC foils which were tested in a 2.0 MeV 150 µA 3mm diameter He^+ beam lasted longer than comparable amorphous graphite and pyrolitic foils. The lifetime of the DLC foils, defined as the time after which the extracted beam dropped to half of its initial value, was 8 times longer than that of standard graphite foils and 40 % longer than that of

the pyrolitic foils. Liechtenstein also investigated the use for atomic mass spectroscopy (AMS). For AMS scattering plays an important role as it limits the final resolution of the system. Liechtenstein found that the scattering of 18 MeV gold ions in a DLC foil of 0.6 µg cm^{-2} thickness was almost negligible and therefore very thin DLC foils qualify for the use in high sensitivity AMS. The third issue investigated by Liechtenstein is the stripping of H- ions in a relatively low energy tandem (100 kV terminal voltage). The transmission for the 0.6 µg cm^{-2} foil was above 80%, for 2 µg cm^{-2} (this is the thinnest commercially available) above 50% and for 5 µg cm^{-2} (these can even be produced self-supporting) approximately 30%. This is encouraging as it shows that stripping and therefore beam operation is realistic for the 7-shell prototype.

Polycrystalline Diamond Polycrystalline diamond foils are usually grown on silicon substrates by CVD processes and then afterwards separated from the substrates. These foils are produced with densities above 300 µg cm^{-2} and successfully used in high power machines ([91]). Ultrananocrystalline diamond foils are commercially available starting with a thickness of 1 µm ([92]). However these foils are too thick for our purpose. The main disadvantage of diamond foils for several hundreds of MeV class accelerators seems to be the graphitising of the diamond above temperatures of 1800 K ([93]).

Carbon Boron In order to get extremely durable stripper foils for the J-PARC rapid cycling synchrotron with a beam energy of 200 MeV for H- and an average beam current of 335 µA, I. Sugai developed hybrid type 250-400 µg cm^{-2} thick boron doped carbon stripper foils ([94]). These were tested with a 3.2 MeV Ne^+ 2.5 µA DC 3.5 mm diameter beam at the Tokyo Institute of Technology Van de Graaff accelerator. As a comparison commercially available carbon foils of 200-400 µg cm^{-2} and pure diamond foils of 350 µg cm^{-2} to 780 µg cm^{-2} were tested with the same procedure. The results

were very encouraging, as the average lifetime of the hybrid type foils exceeded that of diamond foils by a factor of 60 and that of carbon foils by a factor of 280. According to Sugai the problem with the diamond foil might be the high temperature (above 1800 K) which makes the diamond change into graphite structure ([93]). Encouraged by Sugais results S. Zeisler and V. Jaggi developed boron containing stripper foils for their 30 MeV 1 mA H^- beams at the TRIUMF cyclotrons ([95]). They tested a triple layer foil containing a layer of boron between two layers of carbon as well as a compound boron-carbon foil containing 5% boron. For the compound type the lifetime was 20-50% higher than for DLC foils which have been in use at TRIUMF cyclotrons before. The triple layer type foil (45% DLC, 10% B, 45% DLC, total thickness 2.5 µm, 500 µg cm^{-2}) showed an increase in lifetime of 10 % to 15 %. However they have outstanding mechanical strength and flexibility what makes them superior to the 5% compound boron carbon foil whenever mechanical properties play a key role.

Carbon Silicon In a similar way to their boron carbon foils Zeisler and Jaggi tested silicon carbon compound and multilayer foils ([82]). However these proved to be inferior to the boron carbon foils in terms of lifetime as well as in terms of mechanical properties.

Nitrided Carbon I. Sugai produced stripper foils of 15 µg cm^{-2} containing carbon and nitrogen with a ratio of 9:7 by reactive nitrogen-ion-beam sputtering ([96]). He performed lifetime tests with these foils and commercially available foils from Arizona Carbon Foil Co using a 3.2 MeV 4 µA neon ion beam. The nitrided carbon foils showed lifetimes approximately 30 times longer than those of the commercially available carbon foils. In the same investigation Sugai also tested carbon foils containing hydrogen or oxygen. These two approaches were not promising and no further tests were undertaken.

Carbon Nanotubes Recent efforts at the University of Texas in Dallas to produce thin foils of carbon nanotubes for applications as stripper foils have led to interesting results ([97]). The tested very thin single layer nanotube foils with an areal density of approximately 2.7 µg cm^{-2} were able to reach the same performance in terms of durability as comparable graphite foils produced by Chemical Vapour Deposition (CVD). However, in comparison to a laser-ablated carbon foil the carbon nanotube foil did not reach the same ionisation efficiency for the tested 20 MeV $^{58}Ni^{-}$-ions. Multi-layer carbon nanotube foils resulted in lower transmission and did not enhance the ionisation efficiency in an adequate way. According to the authors this is due to the insufficient area coverage of the nanotube bundle strands in the foil. Therefore only a part of the foil contributes to the stripping process while other parts of the foil ("holes") can be traversed by ions without interaction. Stacking of several layers might even increase the inhomogeneity, as there will be very dense points at the crossings of strands of several layers whereas there will also be points of very low density at points with no strand at all (like in a grid). Nevertheless there is a big advantage on carbon nanotube foils. They are very easy to handle and not as fragile as comparable conventional carbon foils of the same thickness (a few µg cm^{-2}). Therefore the production, transportation and the assembly in the accelerator, which is a very critical point for conventional foils of very low thickness, is much easier. Efforts towards densification of the foils to reduce rather than promote inhomogeneity were announced in the paper by von Reden et al and therefore carbon nanotubes might become an interesting option for Hydrogen stripping in the future.

5.2.3 Thickness

The thickness of a stripper foil is an important parameter that impacts the handling and robustness of the foil as well as its lifetime in the beam. It also affects the stripping efficiency, the beam quality and the beam energy. The thicker the foil is, the more do the longitudinal and transversal emittance of the beam grow. This is caused by multiple scattering of the beam particles while propagating through the foil. The emittance growth can also effect the overall transmission of the accelerator. For good robustness and stripping efficiency the foil should be as thick as possible. If we have the beam quality in mind, the foil should be as thin as possible. Therefore a trade-off has to be made between these two requirements.

Energy Loss The energy loss of the protons during the penetration of the foil can be calculated from the stopping power of protons in carbon. Well-established theories exist and good values can be calculated with the TRIM Monte-Carlo code which uses semi-empirical data ([98]). For Carbon the stopping power has its highest value of $0.72\,\mathrm{keV\,\mu g^{-1}\,cm^2}$ at a proton energy of 100 keV. For a foil thickness of $15\ \mu\mathrm{g\,cm^{-2}}$ this would be an average energy loss of about 10 keV. At 500 keV proton energy however the energy loss is just 50% of this value, i.e. 5 keV which is 1% of the beam energy. As for higher beam energies (5 MeV: $0.07\,\mathrm{keV\,\mu g^{-1}\,cm^2}$, 5 keV energy loss with the $15\ \mu\mathrm{g\,cm^{-2}}$ foil, so just 0.1%) the energy loss further decreases, we can see that energy loss is not a serious problem for our machine. However, the energy spread does change. The relevance of this effect of course depends on the application of the machine. In our case the energy spread of the delivered beam is not a problematic issue.

Transverse Scattering and Emittance Growth When penetrating the foil the Hydrogen ions experience multiple scattering and therefore gain transverse momentum. This sets

a limit to the foil thickness as increasing foil thickness means increasing transverse scattering and therefore increasing the emittance which will cause problems with the beam optics. Studies of the scattering with the TRIM Monte-Carlo code ([98]) have shown that noticeable scattering has to be expected for energies below 1 MeV. A 100 keV point-like parallel beam gains a diameter of about 1 cm at a distance of 1 m to a 2 µg cm^{-2} stripper foil. However, for 300 keV this decreases to 3 mm and for 1 MeV to less than a millimetre. For a 15 µg cm^{-2} foil the 1 MeV beam blows up to 2 mm diameter and a 3 MeV or 5 MeV beam to less than a mm. The distance between the terminal and the extraction of the accelerator is less than 1 m, therefore the calculated numbers are sufficient in respect of the beam dynamics. The stripper foil needs to be placed close to the extraction side of the terminal. This ensures a small distance between the foil and extraction and also utilises the focussing effect of the first of the second set of holes.

Stripping Efficiency The charge exchange from H^- to H^+ can happen via two ways, either via double ionization

$$H^- \rightarrow H^+ + 2e^- \tag{5.1}$$

or as a two step process

$$H^- \rightarrow H^0 + e^- \tag{5.2}$$

$$H^0 \rightarrow H^+ + e^- \tag{5.3}$$

of course there are competing processes

$$H^+ + e^- \rightarrow H^0 \tag{5.4}$$

$$H^0 + e^- \rightarrow H^- \tag{5.5}$$

$$H^+ + 2e^- \rightarrow H^- \tag{5.6}$$

The cross sections for all these processes depend on the energy of the incoming particle. Generally in our energy regime the cross sections for higher order processes (as 5.1) are very low ([99]). Therefore these will be neglected in the following considerations. We then get the following rate equations for the quantities of H^- (n_-), H^0 (n_0) and H^+ (n_+):

$$\frac{dn_-}{dx} = n_0\lambda_{0-} - n_-\lambda_{-0} \tag{5.7}$$

$$\frac{dn_0}{dx} = -n_0\lambda_{0+} + n_+\lambda_{+0} - n_0\lambda_{0-} + n_-\lambda_{-0} \tag{5.8}$$

$$\frac{dn_+}{dx} = n_0\lambda_{0+} - n_+\lambda_{+0} \tag{5.9}$$

λ_{xy} are the cross sections per unit length of the ionisation or electron capture processes to go from charge state x (i.e. -,0 or +) to charge state y. Above energies of 100 keV the cross sections for the electron capture processes are very small and can therefore be neglected [100], the equations then have the following solutions:

$$n_-(x) = e^{-\lambda_{-0}x} \tag{5.10}$$

$$n_0(x) = \frac{\lambda_{-0}}{\lambda_{-0} - \lambda_{0+}}\left(e^{-\lambda_{0+}x} - e^{-\lambda_{-0}x}\right) \tag{5.11}$$

$$n_+(x) = 1 - n_-(x) - n_0(x) \tag{5.12}$$

The values λ_{xy} can be obtained from either theoretical calculations as demonstrated in [101, 102, 103] or experimental data from numerous publications which are quoted in the above mentioned papers. [101] and [102] show that the sum of the cross sections of process 5.1 and 5.2 for a single Carbon atom can be described by the following equation:

$$\sigma = 8\pi a_0^2 \frac{\alpha^2}{\beta^2}\left(I - \frac{\alpha^2}{\beta^2}J\right) \tag{5.13}$$

with:

a_0 Bohr radius

α fine-structure constant

β relativistic beta

$I = 16.85$, $J = 13.75$ dimensionless constants

As explained in [99] the cross section for process 5.1 is negligible and therefore the above cross section can be used for process 5.2. Experimental data confirms this equation for energies between 0.4 MeV and 1 GeV. For lower energies however the Born-approximation employed in the calculation breaks down. The cross section for process 5.3 is calculated in [103] and described by the same equation, with $I = 5.83$

and $J = 9.77$. The deviation of the experimental data for energies below 10 MeV is significant for this case, therefore cross sections 30 % and 10 % below the theoretical value have been used for the plots in figure 5.6 and 5.7.

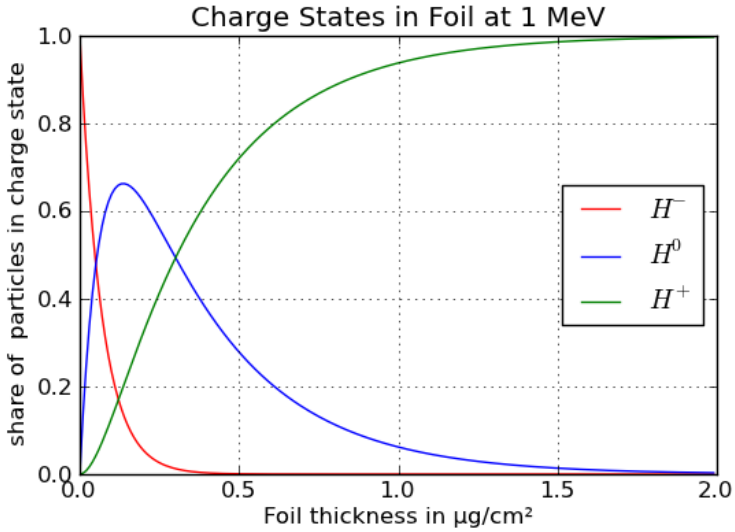

Fig. 5.6: Charge states of ions while traversing through the foil at 1 MeV energy

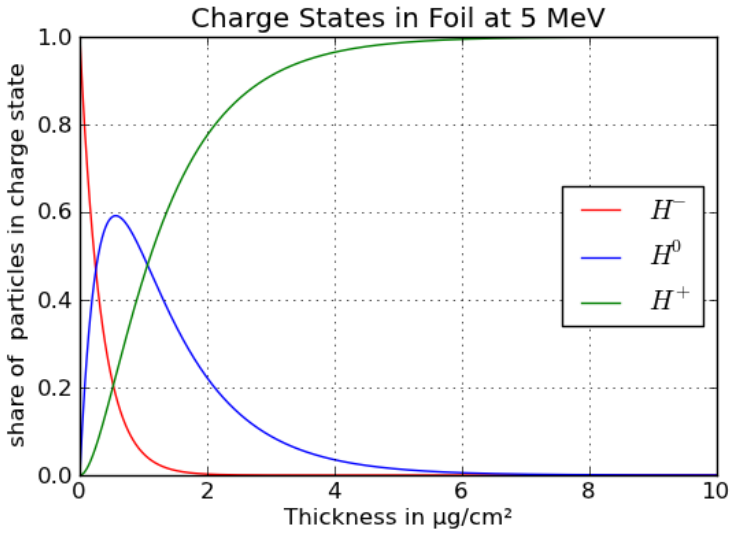

Fig. 5.7: Charge states of ions while traversing through the foil at 5 MeV energy

For energies below 1 MeV a foil thickness of 2 µg cm^{-2} is sufficient to fully strip the ions. For 5 MeV ions charge equilibrium is achieved after ≈6 µg cm^{-2}.

Foil Lifetime Of course the thickness also has an influence on the lifetime of the foil. However, this is very difficult to estimate but generally it can be said that thicker foils

tend to have a longer lifetime than thinner ones. Together with their higher robustness towards handling this is a strong argument to accept more scattering as a trade-off to get more reliability. This will especially apply for a full scale 10 MeV system.

5.2.4 Mounting

The mounting of the stripper foil is an important issue because especially thin foils are very sensitive to mechanical damage. Therefore the mounting should be as supportive to careful foil handling as possible. In order to get access to the inner shells of the accelerator, the whole large vessel has to be vented, the lid has to be taken away with a crane and the frame holding the shells in place has to be lifted out of the vessel with a crane. Some of the diodes interconnecting the shells may have to be removed to gain access to the stripper. This is a very labour-intensive procedure that takes at least a day and also involves risks of damage to some of the involved components. Furthermore it changes the alignment of the shells to the vessel and the ion source. Therefore it is highly recommendable to have a multi-foil system in place to avoid the whole procedure of taking out the shells every time a foil breaks. The assembly of the stripper foil on the foil holder itself is an important variable on foil lifetime as C. Jolivet and J. Stoner reported in [104]. The assembly should avoid stresses due to heat expansion or shrinkage as far as possible. Mounting with fixation just on one side of the foil or on a fork with a wavy shape of the foil would guarantee this. Albeit these constructions are appropriate for rather thick foils (>0.5 µm), they cannot be used for thin foils because these are too fragile to be mounted without assistance. The 0.6 µg cm^{-2} (approximately 3 nm!) DLC foil in [86] was mounted on a ring and supported with a 90 % transmission copper mesh. Foil support with carbon fibres (see [104]) is also widely used. Commercially available foils are usually delivered on a

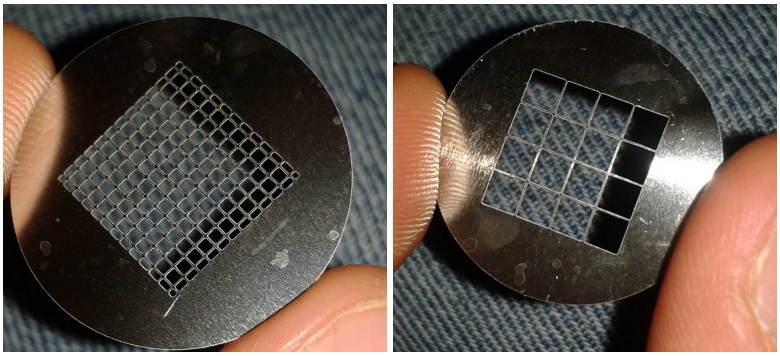

(a) fine grid *(b)* medium grid

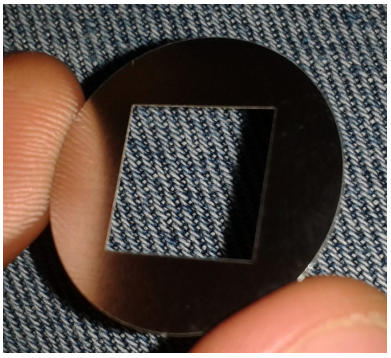

(c) no grid

Fig. 5.8: Stainless steel foil holders with different grids or no grid. The depicted ones are the second generation, the first generation holders had round apertures rather than quadratic ones.

substrate, to make sure that the foil does not experience any harm during transport. The common size is either the size of a standard microscope slide (65 mm × 25 mm) or less (25 mm × 25 mm). To get the foil from the microscope slide onto the holder or grid assembly (for very thin foils) it has to be detached from the slide in a liquid bath, e.g. hot water. The foil floating on the liquid can then be picked up with the mesh or any other assembly. In the case of a mesh the foils usually stick to the mesh so no special fixation is required [89]. This process has to be carried out very carefully because it involves high risk of foil rupture. The transport of the assembly into the accelerator is also very critical, therefore the preparation of the foil assembly should take place as close to the accelerator as possible. Pumping and venting of the vacuum system have to be done very carefully as these can also lead to foil rupture.

5.2.5 Experiments with DLC Foils

There is a large variety of stripper foil production processes resulting in different foil structures and properties. Albeit these might not be the absolute optimum for the whole range of applications, commercially available arc-evaporated carbon foils and laser-ablated diamond-like carbon foils have proven to be reliable and have been tested and used by a large community of cyclotron facilities. As [86] implies, DLC foils have some advantages towards arc-evaporated carbon foils, including lifetime and the very positive experience of [86] with low energies and very thin foils. I therefore decided to do some experiments with DLC foils. A mounting system to hold the foils was developed. It consists of thin stainless steel grids (etched from stainless steel sheets, see Figure 5.8) which hold the foils. The grid is then put into a stainless holder and fixed with a copper piece as heat sink (see Figure 5.9). I ordered DLC foils from Micromatter Inc to test

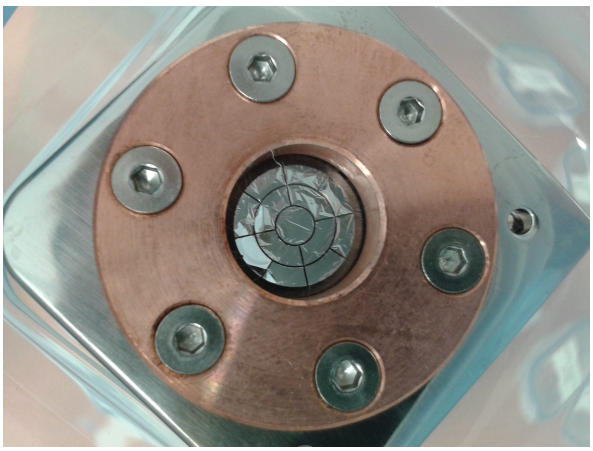

Fig. 5.9: The stripper foil assembly with a 400 atomic layer foil mounted. The round aperture of the grid has proven unfortunate and therefore been abandoned.

the mounting of the foils. The first test involved foils of 100 atomic layers thickness and 400 atomic layers of thickness. These were mounted on round grids (as in Figure 5.9). The floating onto the grids was done in the target laboratory of the CLF (Central Laser Facility) at RAL, as the staff there have expansive experience with DLC foils. The 100 atomic layers foils always ripped during the process of pulling the grid out

of the water. The 400 layer foils ripped in 70 % of the cases and it seemed that this was to do with the round geometry. We then made a new quadratic grid design (as in Figure 5.8) which turned out to be better. With this design it was possible to increase the yield of the 400 layer foils, only $\approx 20\,\%$ of them would rupture during the floating off, the 100 layer foils would still always rupture, independent of the grid. However after storing the foils for some weeks they were all ruptured which was accounted to effects of moisture. The test was repeated with a desiccant in the storage box, the 400 layer foils now survived a couple of month without rupture.

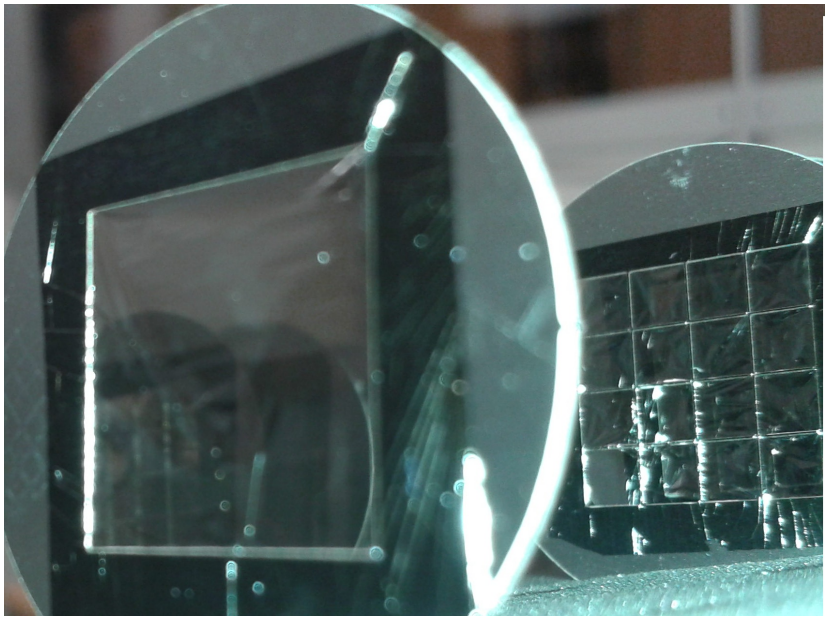

Fig. 5.10: DLC foils of 300 atomic layers thickness after 2 months in a dry storage box. Both of them showed no deterioration, the wrinkle on the front one and the crack on one of the grid fields of the rear one had been there from the very start.

For beam testing with a small number of shells the foils should be as thin as possible. We therefore tested 200 and 300 layer foils as well. The 200 layer foils ruptured whilst pulling them out of the water or during the process of drying. The 300 layer foils however worked well and were still good after 2 months in a storage box with desiccant (see Figure 5.10). It is to be noted that the foils survived on all three grid sizes. The quadratic aperture without grid therefore seems best, however experiments will have

to show whether this is still true with beam operation. Thin foils are very sensitive to even slightest movements of air. Pumping down and venting of vacuum systems is therefore always a potential danger to stripper foils. We performed a series of dedicated tests with our foil setups. The foil assemblies had to undergo a cycle of several pump downs and vents of our genuine vacuum system which is used for the accelerator. The tests were successful with no visible damage to the foils. Generally only one pumpdown will be required for a given foil setup, the result is therefore absolutely satisfactory.

5.2.6 Conclusion

Extensive literature research and conversations with experienced researchers have led to the choice of Diamond Like Carbon as stripper material. Foils with thicknesses from 100 to 700 atomic layers have been bought from a commercial supplier. My tests with different mounting systems and supporting grids led to the conclusion that a rectangular grid shape is far superior to a round grid shape. Tests with pumping have confirmed the suitability of the foils and at the time of writing first beam stripping tests with a 250 keV beam have successfully been completed by other members of the research team.

6. CONCLUSION AND OUTLOOK

Substantial progress towards a full scale system of the novel accelerator concept has been achieved.

The lightweight high voltage drive system has been very successful, operating at 80 kHz with voltages up to 140 kHz peak to peak. Many hundreds of hours of trouble-free operation have proved the robustness and reliability of this part of the system. However, keeping the goal of a very compact overall system in mind, the transformer is relatively large. Future work should therefore investigate ways of reducing the size of the transformer and the research team has indeed already started developing a much more compact replacement.

Successful operation of the voltage multiplier has been demonstrated experimentally. A proof of principle experiment with a 7-shell system at very low fields showed the feasibility of the overall concept. Subsequent work focused on the improvement of the components, especially the inter shell insulators and the diode chains, in order to make them capable of supporting operation at high fields.

The basic design of the inter shell insulator is a cone shaped PEEK insulator of 10 mm thickness and ≈30 mm radius. We tried various designs varying the edge shape as well as ways of reducing the fields at the triple point. The inter shell insulators also have the task of supporting the upper shell set. We therefore tried different ways of attaching

the insulators to the shells. The final design iteration has aluminium stress plates on the top and bottom face of the insulators. They relieve the field at the triple point and also contain a thread for a very flat screw. They can thus be screwed to the shells. This does not only help holding the shells, it also helps to make a tight fit between the shells and the insulators, therefore reducing gaps at the triple point. This enables fields of up to $12\,\mathrm{MV\,m^{-1}}$ across the insulator without breakdown. This is an enormous improvement compared to $8.5\,\mathrm{MV\,m^{-1}}$ which was achieved with the insulators without screws. The insulators are therefore suitable for a commercial system which would aim at $10\,\mathrm{MV\,m^{-1}}$.

We also tested a central structure between the two shell sets which would support the upper shell. The insulators would not have to fulfill this purpose then. This design was not feasible and was therefore abandoned.

As part of the control system I developed a software application which automatically commissions the high voltage system inside the vacuum chamber in a very careful way. It slowly increases the drive voltage until a breakdown happens, then backs it down for some time before increasing it again. It also monitors a number of safety parameters to ensure the proper operation of the system. The software has been successfully validated in simulations and then tested in the real system. It has been used to run most of the high voltage experiments and therefore been a tremendous help throughout the experimental programme. A similar software should definitely be part of a commercial system.

Two ways of protecting the diodes from surge currents during breakdown have been investigated. One consists in limiting the currents between the lowest DC shell and earth. It has been tested very successfully with a 2/3 shell set up to fields as high

as $9.3\,\mathrm{MV\,m^{-1}}$. Due to stray capacitance this method would be very complicated to implement in a full scale system. Therefore a more feasible approach, i.e. series protection resistors in the diode chains, has been tested. Using this protection and a robust and relatively fast diode type, fields of $5.5\,\mathrm{MV\,m^{-1}}$ have been generated in a 4-shell system. After about ten hours of operation at this voltage the diode reverse leakage was tested and first signs of diode degradation were measured.

The diode chains should therefore be a focus for future research as they are currently the limiting component for achieving higher fields. A structured research programme to investigate the failure mechanisms of the diodes and appropriate solutions is planned for the near future. For this purpose currents and power levels in the diodes during realistic operation need to be measured and analysed systematically. Dedicated equipment is currently being developed in order to measure temperature and currents of diodes during operation and especially during breakdown events. As the diodes are at high voltages the measurement concept will be based on LEDs and optical fibres for current measurements and an off-the-shelf optical fibre temperature measurement system.

A detailed characterisation of the ion source beam has been carried out. The development of the wire grid in the Faraday Cup was very challenging, as the wire spacing of 1 mm is rather delicate. The initial design with a macor (ceramic) holder had to be replaced with a PCB. Measurements of the beam width and divergence have proved the excellent beam quality of the ion source. With more than 200 µA the source also fulfills the requirements in terms of beam current.

Beam transport simulations from the ion source through the shells have shown successful beam transport. The simulations are based on the beam data measured with the wire grid. The entrance aperture to the first shells has a very intense focussing

effect. This can either be mitigated by strongly defocussing the ion source beam or by increasing the radius of the first aperture as well as increasing the distance between the shells and the ion source.

The foil stripper system which has been developed and tested in terms of its mechanical robustness, is feasible for installation and pumping. Judging from the experience of other researchers, the stripping with these foils will be straightforward. In fact, at the time of writing, a beam acceleration test with a 7-shell system has been carried out successfully by other members of the research team. This test ran at less than half of the specified field of $10\,\mathrm{MV\,m^{-1}}$. The stripped beam was detected by a fluorescent screen and its mass and polarity was confirmed by deflection with a magnet.

For the realisation of the 7-shell prototype at the full specified field of $10\,\mathrm{MV\,m^{-1}}$ the main challenge is the development of the diode system and its protection. The other components are already suitable for the required voltage. A dedicated diode research programme has already been started. The completion of this programme and the realisation of the 7-shell prototype at full voltage should not take long. Time frames for future research are subject to Siemens non-disclosure policies and will not be discussed in this thesis.

The realisation of a full scale prototype, i.e with about 40 shells, entails some additional challenges. One of these challenges is the manufacturing of the larger shells with reasonable shell weight. This includes the search for a good material as well as for a manufacturing method. Connected to this is the task of improving the insulator design as to make it capable of sustaining more weight. The increased size of shells leads to larger stored energy. This will introduce more stress on the diode chains in the event

of breakdown. Investigations of shell manufacturing have already begun and will be carried out in parallel to research on diode protection. It should therefore be possible to complete the full scale prototype before very long. Again exact time frames are subject to non-disclosure policy.

The step from a functioning full scale prototype to a commercially sold system will involve an immense amount of engineering work. The whole control system needs to be redeveloped from scratch in order to meet regulatory safety requirements. All system components will have to be scrutinised from a safety viewpoint. The whole system will have to be fitted into one unit suitable for transportation from a factory into the client hospital. However Siemens has extensive experience with large medical machinery, including the area of isotope production. This experience, together with the considerable financial and human resources which Siemens commands, will make the commercial development a very doable task. I am therefore confident that the concept will speedily turn into a commercial product as soon as the diode protection challenge has been solved.

BIBLIOGRAPHY

[1] D. Faircloth, "Ion sources for high-power hadron accelerators," *arXiv preprint arXiv:1302.3745*, 2013.

[2] S. R. Cherry, J. A. Sorenson, and M. E. Phelps, *Physics in nuclear medicine*. Elsevier Health Sciences, 2012.

[3] H. Tawara, Y. Itikawa, H. Nishimura, and M. Yoshino, "Cross sections and related data for electron collisions with hydrogen molecules and molecular ions," *Journal of Physical and Chemical Reference Data*, vol. 19, no. 3, pp. 617–636, 1990.

[4] J. Hiskes, "Cross sections for the vibrational excitation of the h2 (x1+ g) state via electron collisional excitation of the higher singlet states," *Journal of Applied Physics*, vol. 51, no. 9, pp. 4592–4594, 1980.

[5] T. Ruth, "Accelerating production of medical isotopes," *Nature*, vol. 457, no. 7229, pp. 536–537, 2009.

[6] P. Beasley, O. Heid, and T. Hughes, "A new life for high voltage electrostatic accelerators," in *Proceedings of IPAC'10*, 2010.

[7] G. De Hevesy, "Radioelements as tracers in physics and chemistry," *Chem News*, vol. 108, p. 166, 1913.

[8] G. De Hevesy, "The absorption and translocation of lead by plants: A contribution to the application of the method of radioactive indicators in the investigation of the change of substance in plants," *Biochem J.*, vol. 17, pp. 439–445, 1923.

[9] H. L. Blumgart and S. Weiss, "Studies on the velocity of blood flow: Vii. the pulmonary circulation time in normal resting individuals 1," *The Journal of Clinical Investigation*, vol. 4, pp. 399–425, 8 1927.

[10] H. O. Anger, "Scintillation camera," *Review of Scientific Instruments*, vol. 29, no. 1, pp. 27–33, 1958.

[11] P. Richards, "A survey of the production at brookhaven national laboratory of radioisotopes for medical research," *VII Rassegna Internazionale Elettronica e Nucleare, Roma*, pp. 223–244, 1960.

[12] J. T. Bushberg and J. M. Boone, *The essential physics of medical imaging*. Lippincott Williams & Wilkins, 2011.

[13] J. Mettler and M. J. Guiberteau, "Essentials of nuclear medicine imaging," *Saunders Elsevier*, 2007.

[14] B. Martin and G. Shaw, *Particle physics*, vol. 45. Wiley. com, 2008.

[15] H. Peng, W. B. Handler, T. J. Scholl, P. Simpson, and B. A. Chronik, "Proof-of-principle study of a small animal pet/field-cycled {MRI} combined system using conventional {PMT} technology," *Nuclear Instruments and Methods in Physics Research Section A: Accelerators, Spectrometers, Detectors and Associated Equipment*, vol. 612, no. 2, pp. 412 – 420, 2010.

[16] C. Catana, Y. Wu, M. S. Judenhofer, J. Qi, B. J. Pichler, and S. R. Cherry, "Simultaneous acquisition of multislice pet and mr images: Initial results with

a mr-compatible pet scanner," *Journal of Nuclear Medicine*, vol. 47, no. 12, pp. 1968–1976, 2006.

[17] L. Yang, D. Rieves, and C. Ganley, "Brain amyloid imagingfda approval of florbetapir f18 injection," *New England Journal of Medicine*, vol. 367, no. 10, pp. 885–887, 2012.

[18] D. M. Goldenberg, J. Horowitz, R. Sharkey, T. Hall, S. Murthy, H. Goldenberg, R. Lee, R. Stein, J. Siegel, and D. Izon, "Targeting, dosimetry, and radioimmunotherapy of b-cell lymphomas with iodine-131-labeled ll2 monoclonal antibody.," *Journal of clinical oncology*, vol. 9, no. 4, pp. 548–564, 1991.

[19] IAEA, "manual for reactor produced isotopes," *IAEA-TECDOC-1340*, 2010.

[20] R. e. a. Bennett, "A system of sup 99mtc production based on distributed electron accelerators and thermal separation," *Journal Name: Nuclear Technology*, Apr 1999.

[21] O. von Guericke, "Experimenta nova (ut vocantur) magdegurgica de vacuo spatio," *Amsterdam*, 1672.

[22] N. Rouland, "Description des machines electrostatiques a taffetas," *Amsterdam*, pp. 45–56, 1785.

[23] J. Wimshurst, "A new form of influence-machine," *Proc. Phys. Soc. London*, vol. 12, p. 403, 1892.

[24] J. Gray, "Electrical influence machines," *Whittaker*, 1903.

[25] G. A. Norton, J. A. Ferry, R. Daniel, and G. M. Klody, "A retrospective of the career of ray herb," *A.I.P. Conference Proceedings*, vol. 473, p. 3, 1999.

[26] E. Rutherford, "The scattering of alpha and beta particles by matter and the structure of the atom," *Philosophical Magazine*, vol. 21, pp. 669–688, 1911.

[27] E. Rutherford, "Collisions of alpha particles with light atoms," *Philos. Mag. J. Sci.*, vol. 37, p. 581, 1919.

[28] J. Cockcroft and E. Walton, "Disintegration of lithium by swift protons," *Nature*, vol. 129, p. 242, 1932.

[29] R. Hellborg, *Electrostatic accelerators [: fundamentals and applications*. Springer, 2005.

[30] H. Greinacher, "Über eine methode, wechselstrom mittels elektrischer ventile und kondensatoren in hochgespannten gleichstrom umzuwandeln," *Zeitschrift für Physik*, vol. 4, no. 2, pp. 195–205, 1921.

[31] M. M. Weiner, "Analysis of cockcroft-walton voltage multipliers with an arbitrary number of stages," *Review of Scientific Instruments*, vol. 40, no. 2, pp. 330–333, 1969.

[32] E. Everhart and P. Lorrain, "The cockcroft-walton voltage multiplying circuit," *Review of Scientific Instruments*, vol. 24, no. 3, pp. 221–226, 1953.

[33] G. Reinhold, K. Truempy, and J. Bill, "The symmetrical cascade rectifier an accelerator power supply in the megavolt and milliampere range," *Nuclear Science, IEEE Transactions on*, vol. 12, no. 3, pp. 288–292, 1965.

[34] A. Kudryavtsev, Y. Belchenko, A. Burdakov, V. Davydenko, A. Ivanov, A. Khilchenko, S. Konstantinov, A. Krivenko, A. Kuznetsov, K. Mekler, *et al.*, "First experimental results from 2mev proton tandem accelerator for neutron productiona)," *Review of Scientific Instruments*, vol. 79, no. 2, p. 02C709, 2008.

[35] R. J. Adler, "Nested high voltage generator/particle accelerator," June 23 1992. US Patent 5,124,658.

[36] R. Adler and R. Richter-Sand, "High voltage, high power nested high voltage accelerator," in *Proc. 1991 Part. Accel. Conf., IEEE Conf. Record*, vol. 91, pp. 3038–7, 1991.

[37] U. Applied Energetics Inc., Tucson Arizona, "Company webpage www.appliedenergetics.com," April 2014.

[38] C. Germain and F. Rohrbach, "High voltage breakdown in vacuum," *Vacuum*, vol. 18, no. 7, pp. 371–377, 1968.

[39] H. C. Miller, "Flashover of insulators in vacuum: review of the phenomena and techniques to improved holdoff voltage," *Electrical Insulation, IEEE Transactions on*, vol. 28, no. 4, pp. 512–527, 1993.

[40] O. Heid and P. Beasley, "Behaviour of non-ideal cockcroft walton systems," *Private Communications*, 2012.

[41] A. Vladimirescu, *The SPICE book*. John Wiley & Sons, Inc., 1994.

[42] M. Engelhardt and I. LTspice, "Linear technology corporation," 2009.

[43] A. S. Pillai and R. Hackam, "Surface flashover of conical insulators in vacuum," *Journal of Applied Physics*, vol. 56, no. 5, pp. 1374–1381, 1984.

[44] N. Khamidov, A. Agzamov, S. Kasimov, and S. Ishanova, "Charge and electric strength of insulator surface in vacuum," *Zes. Nauk. Poli. Poznan. Elektryka*, vol. 38, pp. 221–229, 1989.

[45] N. Jaitly and T. Sudarshan, "Novel insulator designs for superior dc hold-off in bridged vacuum gaps," *Electrical Insulation, IEEE Transactions on*, no. 6, pp. 801–810, 1987.

[46] A. S. Pillai and R. Hackam, "Surface flashover of solid insulators in atmospheric air and in vacuum," *Journal of Applied Physics*, vol. 58, no. 1, pp. 146–153, 1985.

[47] O. Yamamoto, T. Hara, T. Nakae, M. Hayashi, and I. Ueon, "Effects of spark conditioning, insulator angle and length on surface flashover in vacuum," *Electrical Insulation, IEEE Transactions on*, vol. 24, no. 6, pp. 991–994, 1989.

[48] J. Cross and T. Sudarshan, "The effect of cuprous oxide coatings on surface flashover of dielectric spacers in vacuum," *Electrical Insulation, IEEE Transactions on*, no. 4, pp. 146–150, 1974.

[49] A. Holmes, "Design concept of siemens ion source," *Private Communications*, 2011.

[50] Y. I. Belchenko, G. Dimov, and V. Dudnikov, "A powerful injector of neutrals with a surface-plasma source of negative ions," *Nuclear Fusion*, vol. 14, no. 1, p. 113, 1974.

[51] M. Bacal, "Physics basis and future trends for negative ion sources (invited) a)," *Review of Scientific Instruments*, vol. 79, no. 2, p. 02A516, 2008.

[52] A. Holmes, "A one-dimensional model of a negative ion source," *Plasma Sources Science and Technology*, vol. 5, no. 3, p. 453, 1996.

[53] T. Mosbach, "Population dynamics of molecular hydrogen and formation of negative hydrogen ions in a magnetically confined low temperature plasma," *Plasma Sources Science and Technology*, vol. 14, no. 3, p. 610, 2005.

[54] T. Mosbach, "Effects of foreign gases on h- formation in a magnetic multipole hydrogen plasma source," *Plasma Sources Science and Technology*, vol. 14, no. 2, p. 351, 2005.

[55] M. Bacal, "Physics aspects of negative ion sources," *Nuclear Fusion*, vol. 46, no. 6, p. S250, 2006.

[56] J. Peters, "New developments in rf-driven multicusp h- ion sources," *Review of scientific instruments*, vol. 77, no. 3, p. 03A528, 2006.

[57] D. Fussen and C. Kubach, "Theoretical study of mutual neutralisation in h+-h- collisions at low energy (0.02-20 ev)," *Journal of Physics B: Atomic and Molecular Physics*, vol. 19, no. 1, p. L31, 1986.

[58] S. Geltman, "Electron detachment from the negative hydrogen ion by electron impact," *Proceedings of the Physical Society*, vol. 75, no. 1, p. 67, 1960.

[59] J. Whealton, P. Meszaros, R. Raridon, K. Rothe, M. Bacal, J. Bruneteau, and P. Devynck, "Validation and comparison of nonlinear negative ion extraction theory for two experimental configurations," *Revue de Physique Appliquée*, vol. 24, no. 9, pp. 945–949, 1989.

[60] M. Bacal, A. Hatayama, and J. Peters, "Volume production negative hydrogen ion sources," *Plasma Science, IEEE Transactions on*, vol. 33, no. 6, pp. 1845–1871, 2005.

[61] A. Holmes, "Negative hydrogen ion beams," *Plasma physics and controlled fusion*, vol. 34, no. 5, p. 653, 1992.

[62] M. Bacal, "Volume production of hydrogen negative ions," *Nuclear Instruments*

and Methods in Physics Research Section B: Beam Interactions with Materials and Atoms, vol. 37, pp. 28–32, 1989.

[63] A. Ivanov Jr, "Two negative ion groups in volume h- sources," *Review of scientific instruments*, vol. 75, no. 5, pp. 1754–1756, 2004.

[64] F. R. Schwirzke, "Vacuum breakdown on metal surfaces," *Plasma Science, IEEE Transactions on*, vol. 19, no. 5, pp. 690–696, 1991.

[65] P. Chatterton, "Recent developments in vacuum breakdown and discharge physics relevant to accelerator tube design," *Nuclear Instruments and Methods in Physics Research*, vol. 220, no. 1, pp. 73–81, 1984.

[66] B. Jüttner, "Vacuum breakdown," *Nuclear Instruments and Methods in Physics Research Section A: Accelerators, Spectrometers, Detectors and Associated Equipment*, vol. 268, no. 2, pp. 390–396, 1988.

[67] R. Hawley, "Solid insulators in vacuum: a review," *Vacuum*, vol. 18, no. 7, pp. 383–390, 1968.

[68] A. Descoeudres, Y. Levinsen, S. Calatroni, M. Taborelli, and W. Wuensch, "Investigation of the dc vacuum breakdown mechanism," *Phys. Rev. ST Accel. Beams*, vol. 12, p. 092001, Sep 2009.

[69] A. Baschnagel and U. Schlapbach, "Surge current capability of fast recovery diodes," *Power Electronics Europe*, vol. 8, no. 8, pp. 32–37, 2007.

[70] E. W. Thomas, "Atomic data for fusion. volume 3: Particle interactions with surfaces," *ORNL Redbook Atomic Data for Fusion*, vol. 3, no. 3, pp. C22;C23;C34–C37, 1985.

[71] C. Courteille, A. M. Bruneteau, and M. Bacal, "Investigation of a large volume negative hydrogen ion source," *Review of Scientific Instruments*, vol. 66, no. 3, pp. 2533–2540, 1995.

[72] A. J. T. Holmes, R. McAdams, G. Proudfoot, S. Cox, E. Surrey, and R. King, "Intense negative ion sources at culham laboratory (invited)," *Review of Scientific Instruments*, vol. 65, no. 4, pp. 1153–1158, 1994.

[73] R. Gobin, P. Auvray, M. Bacal, J. Breton, O. Delferrire, F. Harrault, A. A. I. Jr., P. Svarnas, and O. Tuske, "Two approaches for h - ion production with 2.45?ghz ion sources," *Nuclear Fusion*, vol. 46, no. 6, p. S281, 2006.

[74] D. . P. A. Components and I. Engineering, "Company website," January 2013.

[75] A. Holmes, "Extraction of heavier ions from h- ion sources," *Private Communications*, 2014.

[76] C. Nieter and J. R. Cary, "Vorpal: a versatile plasma simulation code," *Journal of Computational Physics*, vol. 196, no. 2, pp. 448–473, 2004.

[77] V. Fields, "Opera-2d user guide," *Vector Fields Limited, England*, 1999.

[78] T. Kalvas, O. Tarvainen, T. Ropponen, O. Steczkiewicz, J. Ärje, and H. Clark, "Ibsimu: A three-dimensional simulation software for charged particle opticsa)," *Review of Scientific Instruments*, vol. 81, no. 2, p. 02B703, 2010.

[79] V. D. et al., "Laser stripping of h- beams: theory and experiments," in *Proceedings of PAC07*, 2007.

[80] I. S. et al., "Development of long-lived carbon stripper foils for the ribf project," in *Proceedings of the 17th International conference on cyclotrons and their applications*, 2004.

[81] L. Hao-Lin, W. F. Sommer, and M. J. Borden, "Review of carbon stripper foil lifetime," *Nuclear Instruments and Methods in Physics Research Section A: Accelerators, Spectrometers, Detectors and Associated Equipment*, vol. 362, no. 23, pp. 239 – 244, 1995.

[82] S. K. Zeisler and V. Jaggi, "Carbonsilicon stripper foils," *Nuclear Instruments and Methods in Physics Research Section A: Accelerators, Spectrometers, Detectors and Associated Equipment*, vol. 655, no. 1, pp. 64 – 65, 2011. ¡ce:title¿Proceedings of the 25th World Conference of the International Nuclear Target Development Society¡/ce:title¿.

[83] U. ACF-Metals The Arizona Carbon Foil Co. Inc., Tucson Arizona, "Price list," February 2011.

[84] U. ACF-Metals The Arizona Carbon Foil Co. Inc., Tucson Arizona, "Product information," February 2011.

[85] J. O. S. Jr. and S. A. Miller, "Isotopic 13c target foils 0.4 to 2 2g/cm by pyrolysis of methane, with alternative methods of production," *Nuclear Instruments and Methods in Physics Research Section A: Accelerators, Spectrometers, Detectors and Associated Equipment*, vol. 561, no. 1, pp. 24 – 37, 2006. ¡ce:title¿Proceedings of the 22nd World Conference of the International Nuclear Target Development Society¡/ce:title¿ ¡ce:subtitle¿Preparation of Nuclear Targets and Samples for Advanced Measurements¡/ce:subtitle¿ ¡xocs:full-name¿22nd World Conference of the International Nuclear Target Development Society¡/xocs:full-name¿.

[86] V. Liechtenstein, T. Ivkova, E. Olshanski, R. Golser, W. Kutschera, P. Steier, C. Vockenhuber, R. Repnow, R. von Hahn, M. Friedrich, and U. Kreissig, "Recent investigations and applications of thin diamond-like carbon (dlc) foils," *Nuclear*

Instruments and Methods in Physics Research Section A: Accelerators, Spectrometers, Detectors and Associated Equipment, vol. 521, no. 1, pp. 197 – 202, 2004. ¡ce:title¿Accelerator Target Technology for the 21st Century. Proceedings of the 21st World Conference of the International Nuclear Target Society¡/ce:title¿.

[87] J. O. S. Jr., December 2011.

[88] T. Spickermann, I. Sugai, V. Jaggi, S. K. Zeisler, and et al., "Comparison of carbon stripper foils under operational conditions at the los alamos proton storage ring," in *Proceedings of Hadron Beam 08*, 2008.

[89] MICROMATTER, "Company website," June 2012.

[90] S. K. Z. (micromatter), "private communication and micromatter quotation on thin dlc foils," December 2011.

[91] R. W. S. et al., "Diamond stripper foil experience at sns and psr," in *Proceedings of EPAC08*, 2008.

[92] G. C. Ltd., "Company website," June 2012.

[93] T. Evans and P. F. James, "A study of the transformation of diamond to graphite," *Proceedings of the Royal Society of London. Series A. Mathematical and Physical Sciences*, vol. 277, no. 1369, pp. 260–269, 1964.

[94] I. Sugai, Y. Takeda, M. Oyaizu, H. Kawakami, Y. Irie, Y. Arakida, K. Hara, H. Hattori, K. Kawasaki, J. Kamiya, M. Kinsho, and K. Kuramochi, "Development of thick hybrid-type carbon stripper foils with high durability at 1800K for rcs of j-parc," *Nuclear Instruments and Methods in Physics Research Section A: Accelerators, Spectrometers, Detectors and Associated Equipment*, vol. 561, no. 1, pp. 16 – 23, 2006. ¡ce:title¿Proceedings of the 22nd World

Conference of the International Nuclear Target Development Society¡/ce:title¿ ¡ce:subtitle¿Preparation of Nuclear Targets and Samples for Advanced Measurements¡/ce:subtitle¿ ¡xocs:full-name¿22nd World Conference of the International Nuclear Target Development Society¡/xocs:full-name¿.

[95] S. K. Zeisler and V. Jaggi, "Production of stripper foils by laser ablation of carbonboron sputter targets," *Nuclear Instruments and Methods in Physics Research Section A: Accelerators, Spectrometers, Detectors and Associated Equipment*, vol. 613, no. 3, pp. 434 – 435, 2010. ¡ce:title¿Target and Stripper Foil Technologies for High Intensity Beams¡/ce:title¿ ¡ce:subtitle¿Proceedings of the 24th World Conference of the International Nuclear Target Development Society¡/ce:subtitle¿.

[96] I. Sugai, M. Oyaizu, T. Hattori, K. Kawasaki, T. Yano, H. Muto, Y. Takahashi, and K. Yamazaki, "Nitrided carbon foils as long-lived charge strippers," *Nuclear Instruments and Methods in Physics Research Section A: Accelerators, Spectrometers, Detectors and Associated Equipment*, vol. 303, no. 1, pp. 59 – 62, 1991.

[97] K. von Reden, M. Zhang, M. Meigs, E. Sichel, S. Fang, and R. H. Baughman, "Carbon nanotube foils for electron stripping in tandem accelerators," *Nuclear Instruments and Methods in Physics Research Section B: Beam Interactions with Materials and Atoms*, vol. 261, no. 12, pp. 44 – 48, 2007. ¡ce:title¿The Application of Accelerators in Research and Industry¡/ce:title¿ ¡ce:subtitle¿Proceedings of the Nineteenth International Conference on The Application of Accelerators in Research and Industry¡/ce:subtitle¿ ¡xocs:full-name¿Nineteenth International Conference on The Application of Accelerators in Research and Industry¡/xocs:full-name¿.

[98] J. F. Ziegler, "The stopping and range of ions in matter," June 2012. available via www at the URL http://www.srim.org.

[99] K. Shima, S. Ishii, T. Takahashi, and I. Sugai, "Optimum thickness of carbon stripper foils in tandem accelerator in view of transmission and lifetime," *Nuclear Instruments and Methods in Physics Research Section A: Accelerators, Spectrometers, Detectors and Associated Equipment*, vol. 460, no. 23, pp. 233 – 238, 2001.

[100] H. Tawara and A. Russek, "Charge changing processes in hydrogen beams," *Reviews of modern physics*, vol. 45, no. 2, p. 178, 1973.

[101] G. H. Gillespie, "Double closure calculation of the electron-loss cross section for h- in high-energy collisions with h and he," *Physical Review*, vol. A15, no. 2, p. 563, 1977.

[102] G. H. Gillespie, "High-energy cross sections for h- ions incident on intermediate and high-z atoms," *Physical Review*, vol. A16, no. 3, p. 943, 1977.

[103] G. H. Gillespie, "Systematics of electron-stripping cross sections for fast hydrogenic ions penetrating solids," *Nuclear Instruments and Methods in Physics Research*, vol. B2, pp. 231–234, 1984.

[104] C. S. Jolivet and J. O. S. Jr., "Mounting stripper foils on forks for maximum lifetime," *Nuclear Instruments and Methods in Physics Research Section A: Accelerators, Spectrometers, Detectors and Associated Equipment*, vol. 590, no. 13, pp. 51 – 56, 2008. ¡ce:title¿Toward the Realization of Target and Stripper Foil Technologies for High-Power Proton and Radioactive Ion Accelerators¡/ce:title¿ ¡xocs:full-name¿Proceedings of the 23rd World Conference of the International Nuclear Target Development Society¡/xocs:full-name¿.